4-30-2015

Design, Synthesis, and Characterization of Transition Metal Oxide Based Functional Materials for Multi-Phase Catalytic Applications

Chung-Hao Kuo
University of Connecticut - Storrs, kchunghao@gmail.com

Design, Synthesis, and Characterization of Transition Metal Oxide Based Functional Materials for Multi-Phase Catalytic Applications

Chung-Hao Kuo, PhD

University of Connecticut, 2015

In this thesis, the main focus lies on the nanotechnological synthetic approaches available to heterogeneous catalysis. The seven chapters provided discuss the usefulness of such approaches in multi-phase systems. We discuss several important topics, including the use of carbon nanotubes as support, ligand-free synthesis of metal nanoparticles, and surface chemistry in the production of active metal oxide nanoparticles with well-defined sizes and compositions as a way to control the surface hydrophobicity for use in moisture-saturated gas-phase CO oxidation. Additionally, we introduce the use of solid acids as catalysts for the production of biomass derived platform molecules. High conversion and selectivity can be achieved by controlling the surface area and Brønsted/Lewis acid sites of TiO_2 nanoparticles. Next, we focus on the design and modification of manganese based nanomaterials for photo- and electrochemical water splitting reaction. We first demonstrate that using manganese oxide as support with gold nanoparticles can result in a strong enhancement of catalytic activity for the water oxidation reaction. The enhanced activity of manganese oxide strongly correlates with initial valence of Mn. In Chapter 5, we consider the production and modification of high surface area mesoporous materials and active phases. Reference is then made to the more complex active sites that can be created or carved on such supports by using organic structure-directing agents. Finally, we follow with discussing the ability to achieve multiple functionality in catalysis via the design of specific facet exposed manganese oxide nanoparticles. The active MnO facets with higher adsorption energy of oxygen species can

largely promote electrocatalytic activity. We conclude with a personal and critical perspective on the importance of fully exploiting the synergies between nanotechnology and surface science to optimize the search for new catalysts and catalytic processes.

Design, Synthesis, and Characterization of Transition Metal Oxide Based Functional Materials for Multi-Phase Catalytic Applications

Chung-Hao Kuo

B.S., Tamkang University, Taiwan, 2004

M.S., Tamkang University, Taiwan, 2006

A Dissertation

Submitted in Partial Fulfillment of the

Requirements for the Degree of

Doctor of Philosophy

at the

University of Connecticut

2015

APPROVAL PAGE

Doctor of Philosophy Dissertation

Design, Synthesis, and Characterization of Transition Metal Oxide Based Functional Materials for Multi-Phase Catalytic Applications

Presented by

Chung-Hao Kuo, B.A., M.A.

Major Advisor _____
Steven L. Suib

Associate Advisor _____
Jie He

Associate Advisor _____
Alfredo Angeles-Boza

Associate Advisor _____
S. Pamir Alpay

Associate Advisor _____
Fatma Selampinar

University of Connecticut
2015

Acknowledgements

I would like to acknowledge my major advisor Dr. Steven L. Suib for giving me this opportunity to work in his group. Before I came to U. S., I would not imagine myself can accomplish such tasks to fulfill my dream of doing research. The most important things that I learned from Dr. Suib are not all about chemistry, the problem solving ability, the way of communicating with people, and the dedication to work with enthusiasm will stay with me for my future challenges. I also need to thank Dr. Jie He for his guidance. I really enjoy the time we spent in the lab and at the time we were brainstorming the ideas. I will always cherish the way he treats with me more like a friend than an advisor. I greatly appreciate Dr. Frank Galasso for his help during my Ph.D. life. In addition, a thank you to my previous advisor Dr. Hsiu-Fu Hsu, who introduced me to embrace the beauty of chemistry and his patience to listen to my complaints and give me guidance even when I was in the U. S.

I appreciate Dr. Roger Ristau, Lichun Zhang, Heng Zhang, Daniel Daleb, You-Jun Fu, and Charlene Fuller for their assistances in my research life. I would also like to show my gratitude to my committee members Dr. Alfredo Angeles-Boza, Dr. S. Pamir Alpay, and Dr. Fatma Selampinar. Many people, especially my colleges and team members, Dr. Lei Jin, Dr. Cecil King'ondu, Dr. Yashan Zhang, Dr. Saminda Dharmarathna, Sheng-Yu Chen, Sourav Biswas, Abdelhamid El-Sawy, Biswanath Dutta, Curtis Guild, Saiful Islam, Tehereh Jafari, Jing Jin, Dave Kriz, Zhu Luo, Yong-Tao Meng, Andrew Meguerdichian, Mahbubur Shakil, Madhavi Pahalagedara, Lakshitha Pahalagedara, Junkai He, Ran Miao, Wenqiao Song, Niluka Wasalathanthri, Wei Zhong, Ehsan Moharreri, Weikun Li, Srinivas Thanneeru, Ben Liu, Istvan Kanyo, Anton Gudz and especially Dr. Altug Poyraz have made valuable research life with me in the lab.

Finally, I want to thank my family for their sacrifices. My parents and my parents in law always support me when I need help. Without them, I cannot finish my Ph.D. and have such a life here. I need to thank my life partner, my wife, for her understanding, unconditional love, and most importantly completing my life with a beautiful son.

Table of Contents

List of Figures, Schemes, and Tables

Chapter 1. Introduction.

1.1 Overview of Heterogeneous Catalysis

The use of heterogeneous catalysis is widespread in the chemical industry and there are estimates that over 90% of chemical manufacturing is based on or relies on catalytic processes.[1] In more recent applications, the focus is not only on promoting reaction conversion, but also on suppressing side reactions. This has been developed to improve reaction yield, to simplify chemical manufacturing processes by eliminating the use of catalysts, and to reduce the production of hazardous side products. A better control of the nature of the solids used as catalysts leads to a better control of their catalytic activity, selectivity, and stability. The emphasis on reaction selectivity has opened up new challenges on the requirements for the control of the characteristics of heterogeneous catalysts. The traditional preparation of catalysts via precipitation and solid state synthesis methods lacks control over morphology and nature of the solids and relies on averaging the effects of many different particles. Therefore, it is difficult to modify activity and selectivity of such materials.

With the development of nanotechnologies in recent years, the synthesis of more complex and distinct materials has become possible, and with many of those having been implemented in catalysis.[2,3] New synthetic approaches enable us to not only produce materials with specific size, but also to grow complex composites with different substrates as well as to control the surface behavior of the materials. The fulfillment of afore-mentioned specific requirements in catalysis is greatly improving the design and preparation of well-defined heterogeneous catalysts with highly desirable properties.

1.2 Background and Significance

1.2.1 Heterogeneous Catalyst in CO Oxidation

The understanding of the oxidation of CO as a prototypical reaction for heterogeneous processes has motivated enormous progress and fundamental insight. CO oxidation is one of the well-known heterogeneous reactions and can be regarded as a probe system for examining the activity of a prepared catalyst. From a chemist's point of view, the simple reaction: $2CO + O_2 \rightarrow 2CO_2$ can be described as the oxidation of CO to form CO_2. However, considering that this reaction consist of a three stage process (diffusion, adsorption, and surface reaction) when heterogeneous catalysts are incorporated, the inherent mechanisms are more complicated than the reaction formula shown above. The reaction may be able to occur with the use of a catalyst through activation of oxygen molecules closest to the location of chemisorbed CO molecules, thus allowing a spatially decoupled combination to give the product molecule CO_2. This presents the challenge of investigating the underlying processes at the atomic level and understanding the entire course of the reaction, including its complexity under reaction conditions.

Current heterogeneous catalysts used for CO oxidation can be separated into three main categories: metals, metal oxides, and supported composites. CO oxidation over metals has been studied in detail elsewhere, and the development of commercially available catalytic converters in the 1970s already pointed out the exceptional activity of noble metals (Pt, Pd, Rh) for CO oxidation.[4] However, due to the relatively limited resources of noble metals and the remarkable progress in oxide preparations, catalytic oxidation of carbon monoxide over oxide catalysts has recently gained much interest. In general, noble metals are more active than base metals. However, some oxides, especially those of Co and Cu exhibit an interesting activity for CO oxidation. Undesirable behavior in cycled transient conditions and high susceptibility to deactivation by

sulfur and water are the main reasons that prohibit the practical applications of base metal oxide catalysts.[5]

1.2.1.1 Cobalt Oxide in CO Oxidation

The nature of cobalt oxides and especially the proportion of Co^{2+}, Co^{3+}, and even Co^{4+} was investigated extensively for CO oxidation. Among all accessible types of cobalt oxide, the most active form would be Co_3O_4 in which cobalt is present in two valence states (2^+ and 3^+). The crystal structure of Co_3O_4 is an ideal spinel structure in which Co^{2+} cations occupy one-eighth of the tetrahedral sites while Co^{3+} cations occupy half of the octahedral sites. The spinel Co_3O_4 is also the most stable oxide between 350 ^oC and 900 ^oC. Cobalt oxides have been widely used as precursors to cobalt metal catalysts for Fischer-Tropsch synthesis.[6] The first comprehensive studies on hydrocarbon oxidation of various unsupported Co_3O_4 catalysts were performed by Yu Yao et al. in 1974.[7] The important conclusion made was the fact that cobalt oxides containing Co^{2+}/Co^{3+} ion pairs are very active in CO oxidation. Specific sites for O adsorption (Co^{2+}-O- Co^{3+}) and for CO adsorption (Co^{2+}-CO) require a good balance between Co^{2+} and Co^{3+} species for an optimum activity in oxidation. Further evidence showed that Co_3O_4 has the lowest activation energy (18 $kJmol^{-1}$), much lower than that of CoO (38 $kJmol^{-1}$). The cluster size of Co_3O_4 was also shown to be a factor that affects the activity.[8]

1.2.2 Heterogeneous Biomass Conversion Reaction

Fossil fuels are still the primary carbon feedstocks for fine chemical synthesis and energy sources.[9] However, the increasing demand for fossil resources has raised many problems such as

environmental degradation and global fossil carbon emission. The development of alternative resources is important in decreasing the demand for fossil fuels. Many reported works on biosource chemicals either deal with a large variety of biomass feedstock and reaction types or focus on specific feedstocks such as carbohydrates, triglycerides, glycerol, 5-hydroxymethylfurfural, cellulose, hemicelluloses and pentoses, lignin, and lignocellulose. Some works were dedicated to specific reaction types such as hydrogenolysis/dehydroxylation, telomerization, metathesis, and oxidation. Heterogeneous catalysts have only been recently utilized as a central element in biomass conversion.[10] Several solid acids such as zeolites,[11-13] metal oxides,[14] polymer based acids,[15] and heteropoly acids[16,17] have been widely used to convert carbohydrates. Although solid acids are more easily separated, recycled, and environmentally benign, there are still considerable opportunities for improving the selectivity and mass transfer process of the insoluble polymers and heterogeneous catalysts. The key aspect is the use of a molecule that is derived from sugars and can be flexibly converted to either chemicals or biofuels, but without the loss of carbon atoms (i.e. preserving intrinsic energy). This requires new catalytic (multifunctional) chemistry that offers the advantage of utilizing the established knowledge on tailored synthesis in terms of pore and crystal engineering, presence of different active acids, and redox sites.

1.2.2.1 Zeolite as Catalyst in Biomass Reaction

Zeolites and related materials have been one of the areas in the field of materials and catalysis with the largest impact on science, technology, and industrial processes. The use of zeolites in the field of biomass conversion has been studied extensively. Taarning et al.[11] have discussed the conversion of lignocellulosic material or monosaccharides using Ti and Sn beta zeolites as the catalysts. Due to the high Lewis acidity of such catalysts, the formation of alkoxyl lactates can be

achieved in alcohol media. Huber and coworkers[18] have instead discussed the role of Lewis and Brønsted acid sites in the design of catalysts for aqueous-phase dehydration of carbohydrates. Davis and coworkers[19] further demonstrated the possible mechanism using ^{13}C labeling NMR characterization for the isomerization of trioses to lactic acid and for the isomerization-esterification to form lactate esters. Interestingly, in another example, Corma and coworkers[20] presented the enhancement of biomass conversion using the combination of Lewis and Brønsted acids zeolite type catalysts.

1.2.2.2 Sulfated Metal Oxide as Catalyst in Biomass Reaction

Sulfated metal oxides are also a useful group of strong acid catalysts in biomass conversion. Modification of the metal oxide surface with a suitable sulfated process can develop the ability to catalyze reactions characteristic of very strong acid catalysts at low temperatures, although with limited lifetimes. The nature-active catalytic site has been proposed in many different studies. In general, different models of the active site can be based on the symmetry of the coordinated sulfate ion on the surface of metal oxides.[21] In the case of SO_4^{2-}/ZrO_2 materials, Brønsted-Lowry acidity can be generated by an inductive effect when sulfate adopts a bridging C_{2v} symmetry. For heterogeneously catalyzed biomass reactions with sulfated metal oxides, Brønsted acidity driven reactions tend to produce platform molecules such as 5-hydroxymethylfurfural or levulinate esters. Several examples of the sulfated acidic catalysts for transformation of fructose into levulinate esters have been reported. These include nanoparticles of TiO_2,[22] carbon nanotubes functionalized with sulfonic acids,[23] mesoporous sulfonated materials such as SBA-SO_3H,[24] SO_4^{2-}/TiO_2,[25] SO_4^{2-}/ZrO_2.[26] With fructose as the starting resource, levulinate esters can be produced in 57~78% yield with a corresponding alcohol at 130~200 ^oC. With glucose, the given levulinate esters produce

lower yields (13~50 %) than fructose and require harsher reaction conditions, i.e. higher temperatures, stronger acidity of the catalyst, and a longer reaction time.

1.2.2.3 Heteropoly acid as Catalyst in Biomass Reaction

Among the many acid catalysts discussed above, heteropoly acids (HPAs) are another preferred choices. The high crystalline nature of HPAs often presents intrinsic low specific surface areas. To overcome such a problem, HPAs are usually used with metal oxide supports that have high specific surface areas. Dharne et al.[27] demonstrated the importance of HPA loading for supported $H_3PW_{12}O_{40}$ or $(NH_4)_3PMo_{12}O_{40}$ on montmorillonite. Similarly, Nandiwale et al.[28] deposited $H_3PW_{12}O_{40}$ on partially desilicated ZSM-5 zeolite. The catalysts exhibited enhanced textural and acidic properties and allowed for high conversion and higher selectivity to levulinate esters. However, the loss of activity due to HPAs leaching on the substrate surface often occurred. The use of HPAs inserted within oxide matrixes as catalysts can stabilize the active phase over leaching. Pasquale et al.[29] incorporated $H_3PMo_{12}O_{40}$ or $H_4SiW_{12}O_{40}$ in silica frameworks to form mesoporous solids. The confinement of the HPA into mesopores facilitates the mass transport of reactant and products. Su et al.[30] reported the introduction of $H_3PW_{12}O_{40}$ in a zirconia-modified mesoporous organic silica matrix.

1.2.3 Transition Metal Based Catalyst for Water Oxidation Reaction

Artificial photosynthesis is a process in which solar energy is used to reduce a substrate into an energy-rich chemicals while generating fuel either for direct combustion or for fuel power cells. The key task to yield a breakthrough for constructing an artificial photosynthetic device requires detailed understanding of the catalytic aspects of photo- or photoelectro-driven water oxidation. In the majority of related studies in the past two decades, many homogeneous catalysts were made of noble metals such as, ruthenium, iridium, and rhodium.[31] The studies dealing with molecular aspects of the catalysts provide hints for development of novel efficient catalysts and help gain clues to reveal the mechanism of O_2 evolution catalyzed at the photosynthetic oxygen evolving complex (OEC) whose active site is known to consist of a tetramanganese-oxo cluster.[32] However, these noble metal catalysts significantly increase the cost for real applications.

With respect to the heterogeneous catalysts in water splitting, first-row transition metal oxides have been investigated extensively since the 1980s[33-35], forming a large part of commercially available electrolyzers. Ni and Co oxide based OER catalysts have shown superior catalytic activity. Various Mn oxides have also been reported to catalyze the OER; with the extent of catalysis being based on the modification of synthetic method as well as on the nature of the dopant (such as Mo or W). However, there are two main drawbacks to using first-row transition metal oxides for the water splitting reaction: difficult characterization and benchmarking as well as limited working conditions. The activity of metal oxide catalysts depends on many parameters, including preparation method, material structure, morphology, etc. The lack of exact structural and electronic information about the active sites makes it difficult to optimize these activities.[36,37] Moreover, most metal oxide catalysts are efficient only in alkali conditions, and are inactive in neutral or acidic environments. Based on current progress, the design of highly active materials as

bifunctional catalysts for simultaneously generating H_2 and O_2 is still a challenging issue, which is crucial for improving the overall efficiency of water electrolysis.[38,39]

1.2.3.1 Catalytic Methods Used for Water Oxidation Reaction

Catalytic methods used to evaluate catalyst activity can be categorized into photochemical, chemical, and electrochemical when considering the water oxidation reaction. In photochemical methods, the well-established $Ru(bpy)_3^{2+}$-$S_2O_8^{2-}$ (bpy = 2,2'-bipyridine) system with visible light irradiation is often used. This system can provide a modest overpotential (η) of 370 mV. The overall photo-electrochemical reaction of this system is: $2Ru(bpy)_3{}^{2+} + S_2O_8{}^{2-} + hv \rightarrow 2Ru(bpy)_3{}^{3+} + SO_4{}^{2-}$, where $Ru(bpy)_3^{2+}$ is a photosensitizer and $S_2O_8^{2-}$ is a sacrificial electron acceptor. The $Ru(bpy)_3^{3+}$ species can be reduced back to $Ru(bpy)_3^{2+}$ by pulling one electron from the catalyst, whereas water molecules lose electrons and get oxidized to form O_2. The generated O_2 in solution is often measured by the Clark-type electrode system. In chemical oxidation system, one-electron primary oxidants such as cerium (IV) ammonium nitrate (CAN) are typically used. Higher overpotential (η) of 530 mV is achieved by using such oxidant. These one-electron oxidants may better mimic the multiple, sequential, single-electron transfer events which take place in natural photosynthesis, and studies on water oxidation catalysts driven by these one-electron oxidants show promise for adaptation to light-driven systems (i.e., artificial photosynthesis). Headspace-released O_2 is often measured and quantified by gas chromatography due to relatively higher oxidative activity of such oxidants.

In electrochemical oxidation methods, the term oxygen evolution reaction (OER) is often used. The overall electrolysis of water is presented below. The OER reaction takes place at the anode and hydrogen evolution reaction (HER) at the cathode.

Anode: $2H_2O^+ \rightarrow 4H^+ + O_2 + 4e^-$ ……. (1)

Cathode: $4H^+ + 4e^- \rightarrow 2H_2$ …… (2)

Cell: $2H_2O \rightarrow 2H_2 + O_2$ ……. (3)

Due to the large energy barrier in electrochemical oxidation of water, OER is regarded as one of the most difficult electrolytic reactions in an electrochemical cell, in which the cell voltage (i.e. the energy consumption of the process) is governed by the anodic reaction. The catalyst used here is thought to participate in the reaction mechanism in such a way that charge transfer is facilitated. OER results from reactions in series show that hydroxyl radicals are the important intermediates produced during OER.

For the discussion of the mechanism in the OER reaction using heterogeneous electrocatalysts, the first common step is the discharge of water molecules to hydroxyl radicals at the anode surface.[40] The subsequent steps depend on the strength of the interaction between the hydroxyl radicals and the electrode surface which, in turn, depends on the nature of the electrode material. Atomic oxygen is later formed and adsorbed at the surface followed by fast recombination into molecular oxygen. At the active electrodes, a strong interaction with hydroxyl radicals exists and the oxygen evolution reaction occurs via the formation of higher oxides. In contrast, at the non-active electrodes, the substrate does not participate in the process and the oxidation is assisted by hydroxyl radicals that are weakly adsorbed at the electrode surface.

1.2.3.2 Manganese Oxide Based Catalysts for Water Oxidation reaction

Manganese is one of the most studied metals in water oxidation catalysis,[41] exhibiting remarkable efficiency within a tetramanganese and calcium cluster in the photosystem II (PS II). Therefore, manganese oxide surfaces and molecular mimics are potentially interesting materials in water oxidation catalysis. Dismukes et al. reported the use of nanocrystalline λ-MnO_2 as a water oxidation catalyst, and this is believed to be the first example of a heterogeneous system.[42] The delithiation of Spinel $LiMn_2O_4$ to form cubical Mn_4O_4 substructure in λ-MnO_2 successfully mimics the $CaMn_4O_4$ core of the PSII-WOC structure. A number of Mn-based catalysts such as MnOOH, α-MnO_2, β-MnO_2, amorphous MnO_x, and Mn_3O_4 have already demonstrated activity for the WOR, particularly the α-Mn_2O_3 phase. The hypothesis has been made by Dismukes et al., stating that Mn^{3+}−O edge sharing octahedra at the surface are more reactive due to the weaker, more flexible bonds.[43] However, the Mn^{3+} species are unstable under acidic and even neutral conditions due to their disproportionation into Mn^{2+} and Mn^{4+} for the formation of less active MnO_2 on the catalyst surface. Therefore, several examples using Li^+ or mixed-metal oxide systems are reported for the purpose of stabilizing Mn^{3+} in the catalyst structure. Other efforts dealing with adjusting catalyst morphology,[44] enhancing surface area by loading MnO_x on supports,[45] and increasing activity with noble metal loaded[46] are also reported. Many efforts are still needed in order to overcome the limitation of working conditions and to improve the long-term catalytic activity.

1.2.4 References

(1) Armor, J. N. *Catal. Today* **2011**, *163*, 3-9.

(2) Lee, I.; Zhang, Q.; Ge, J.; Yin, Y.; Zaera, F. *Nano Res.* **2011**, *4*, 115-123.

(3) Lee, I.; Albiter, M. A.; Zhang, Q.; Ge, J.; Yin, Y.; Zaera, F. *Phys. Chem. Chem. Phys.* **2011**, *13*, 2449-2456.

(4) Yao, Y.-F. Y. *J. Catal.* **1984**, *87*, 152-162.

(5) Hammes, M.; Soerijanto, H.; Schomäcker, R.; Valtchev, M.; Stöwe, K.; Maier, W. F. *ChemCatChem* **2014**, *6*, 245-254.

(6) Poizot, P.; Laruelle, S.; Grugeon, S.; Dupont, L.; Tarascon, J. *Nature* **2000**, *407*, 496-499.

(7) Yu Yao, Y. *J. Catal.* **1974**, *33*, 108-122.

(8) Lin, H.-K.; Chiu, H.-C.; Tsai, H.-C.; Chien, S.-H.; Wang, C.-B. *Catal. lett.* **2003**, *88*, 169-174.

(9) Somerville, C.; Youngs, H.; Taylor, C.; Davis, S. C.; Long, S. P. *Science* **2010**, *329*, 790-792.

(10) Démolis, A.; Essayem, N.; Rataboul, F. *ACS Sustainable Chem. Eng.* **2014**, *2*, 1338-1352.

(11) Holm, M. S.; Saravanamurugan, S.; Taarning, E. *Science* **2010**, *328*, 602-605.

(12) Jow, J.; Rorrer, G. L.; Hawley, M. C.; Lamport, D. T. A. *Biomass* **1987**, *14*, 185-194.

(13) Lourvanij, K.; Rorrer, G. L. *Appl. Catal. A* **1994**, *109*, 147-165.

(14) Wang, P.; Zhan, S. H.; Yu, H. B. *Adv. Mater. Res.* **2010**, *96*, 183-187.

(15) Takagaki, A.; Ohara, M.; Nishimura, S.; Ebitani, K. *Chem. Commun.* **2009**, 6276-6278.

(16) Sun, Z.; Cheng, M.; Li, H.; Shi, T.; Yuan, M.; Wang, X.; Jiang, Z. *RSC Adv.* **2012**, *2*, 9058-9065.

(17) Palkovits, R.; Tajvidi, K.; Ruppert, A. M.; Procelewska, J. *Chem. Commun.* **2011**, *47*, 576-578.

(18) Weingarten, R.; Tompsett, G. A.; Conner Jr, W. C.; Huber, G. W. *J. Catal.* **2011**, *279*, 174-182.

(19) Nikolla, E.; Román-Leshkov, Y.; Moliner, M.; Davis, M. E. *ACS Catal.* **2011**, *1*, 408-410.

(20) Casanova, O.; Iborra, S.; Corma, A. *J. Catal.* **2010**, *275*, 236-242.

(21) Song, X.; Sayari, A. *Catal. Rev. Sci. Eng.* **1996**, *38*, 329.

(22) Kuo, C.-H.; Poyraz, A. S.; Jin, L.; Meng, Y.; Pahalagedara, L.; Chen, S.-Y.; Kriz, D. A.; Guild, C.; Gudz, A.; Suib, S. L. *Green Chem.* **2014**, *16*, 785-791.

(23) Liu, R.; Chen, J.; Huang, X.; Chen, L.; Ma, L.; Li, X. *Green Chem.* **2013**, *15*, 2895-2903.

(24) Saravanamurugan, S.; Nguyen Van Buu, O.; Riisager, A. *ChemSusChem* **2011**, *4*, 723-726.

(25) Saravanamurugan, S.; Paniagua, M.; Melero, J. A.; Riisager, A. *J. Am. Chem. Soc.* **2013**, *135*, 5246-5249.

(26) Peng, L.; Lin, L.; Li, H.; Yang, Q. *Appl. Energy* **2011**, *88*, 4590-4596.

(27) Dharne, S.; Bokade, V. *J. Nat. Gas Chem.* **2011**, *20*, 18-24.

(28) Nandiwale, K. Y.; Sonar, S. K.; Niphadkar, P. S.; Joshi, P. N.; Deshpande, S. S.; Patil, V. S.; Bokade, V. V. *Appl. Catal., A* **2013**, *460*, 90-98.

(29) Pasquale, G.; Vázquez, P.; Romanelli, G.; Baronetti, G. *Catal. Commun.* **2012**, *18*, 115-120.

(30) Su, F.; Wu, Q.; Song, D.; Zhang, X.; Wang, M.; Guo, Y. *J. Mater. Chem. A* **2013**, *1*, 13209-13221.

(31) Yamazaki, H.; Shouji, A.; Kajita, M.; Yagi, M. *Coord. Chem. Rev.* **2010**, *254*, 2483-2491.

(32) Yachandra, V. K.; Sauer, K.; Klein, M. P. *Chem. Rev.* **1996**, *96*, 2927-2950.

(33) Matsumoto, Y.; Sato, E. *Mater. Chem. Phys.* **1986**, *14*, 397-426.

(34) Hall, D. E. *J. Electrochem. Soc.* **1985**, *132*, 41C-48C.

(35) Trasatti, S. *Electrochim. Acta* **1991**, *36*, 225-241.

(36) Chen, J.; Selloni, A. *J. Phys. Chem. C* **2013**, *117*, 20002-20006.

(37) Bajdich, M.; García-Mota, M.; Vojvodic, A.; Nørskov, J. K.; Bell, A. T. *J. Am. Chem. Soc.* **2013**, *135*, 13521-13530.

(38) Cobo, S.; Heidkamp, J.; Jacques, P.-A.; Fize, J.; Fourmond, V.; Guetaz, L.; Jousselme, B.; Ivanova, V.; Dau, H.; Palacin, S.; Fontecave, M.; Artero, V. *Nat. Mater.* **2012**, *11*, 802-807.

(39) Zhang, C.; Antonietti, M.; Fellinger, T.-P. *Adv. Fun. Mater.* **2014**, *24*, 7655-7665.

(40) Deabate, S.; Fourgeot, F.; Henn, F. *Electrochim. Acta* **2006**, *51*, 5430-5437.

(41) Galán-Mascarós, J. R. *ChemElectroChem* **2015**, *2*, 37-50.

(42) Robinson, D. M.; Go, Y. B.; Greenblatt, M.; Dismukes, G. C. *J. Am. Chem. Soc.* **2010**, *132*, 11467-11469.

(43) Robinson, D. M.; Go, Y. B.; Mui, M.; Gardner, G.; Zhang, Z.; Mastrogiovanni, D.; Garfunkel, E.; Li, J.; Greenblatt, M.; Dismukes, G. C. *J. Am. Chem. Soc.* **2013**, *135*, 3494-3501.

(44) Kuo, C.-H.; Mosa, I. M.; Poyraz, A. S.; Biswas, S.; El-Sawy, A. M.; Song, W.; Luo, Z.; Chen, S.-Y.; Rusling, J. F.; He, J. *ACS Catal.* **2015**, *5*, 1693-1699.

(45) Jiao, F.; Frei, H. *Energy Environ. Sci.* **2010**, *3*, 1018-1027.

(46) Kuo, C. H.; Li, W.; Pahalagedara, L.; El-Sawy, A. M.; Kriz, D.; Genz, N.; Guild, C.; Ressler, T.; Suib, S. L.; He, J. *Angew. Chem. Int. Ed.* **2014**.

Chapter 2. Facile Synthesis of Co_3O_4@CNT with High Catalytic Activity for CO Oxidation under Moisture-Rich Conditions.

2.1 Overview and Abstract

The catalytic oxidation reaction of CO has recently attracted much attention due to potential applications in the treatment of air pollutants. The development of inexpensive transition metal oxides catalysts that exhibit high catalytic activities for CO oxidation is in high demand. However, these metal oxide catalysts are susceptible to moisture, as they can quickly be deactivated in the presence of trace amounts of moisture. Our work here concentrates a facile synthesis of highly active Co_3O_4@CNT catalysts for CO oxidation under moisture-rich conditions. Our synthetic routes are based on the *in situ* growth of ultrafine Co_3O_4 nanoparticles (NPs) (~2.5 nm) on pristine multi-walled CNTs in the presence of polymer surfactant. Using a 1% CO, 2% O_2 balanced in N_2 (normal) feed gas (3-10 ppm moisture), a 100% CO conversion with Co_3O_4@CNT catalysts was achieved at various temperatures ranging from 25 to 200^{o}C at a low O_2 concentration. The modulation of surface hydrophobicity of CNT substrates other than direct surface modification on the Co_3O_4 catalytic centers is an efficient method to enhance the moisture resistance of metal oxide catalysts for CO oxidation. After introducing fluorinated alkyl chains on CNT surfaces, the superhydrophobic Co_3O_4@CNT exhibited outstanding activity and durability at 150^{o}C in the presence of moisture-saturated feed gas. These materials may ultimately present new opportunities to improve the moisture resistance of metal oxide catalysts for CO oxidation.

2.2 Introduction

Carbon monoxide (CO) from the incomplete combustion of hydrocarbon fuels is one of the major air pollutants.[1] The catalytic oxidation reaction of CO has become increasingly important in diminishing the emission of CO through the pretreatment of effluent gas from various industries and automobile exhaust. Although noble metal catalysts or supported noble metal catalysts (*i.e.* Pt, Pd, and Au) have proven to be the most active,[2-8] the high cost of such catalysts largely limits their extensive applications. In this context, inexpensive metal oxide catalysts have recently attracted attention. Particularly, Co_3O_4, CuO and MnO_2 exhibit high catalytic activities for CO oxidation.[9-19] The metal oxide catalysts, like Co_3O_4, however, are susceptible to moisture, as they can quickly be deactivated in the presence of trace amounts of moisture (> 3 ppm). To date, the development of highly active Co_3O_4 catalysts for CO oxidation that operate at high moisture conditions is still very challenging. Recent reports have demonstrated that nanostructures[13-17, 20] and surface properties of Co_3O_4 catalysts[10, 18-19, 21] play important roles in the activity of catalysts under moisture. On one hand, the active species of Co^{3+} cations are distributed on (110) facets of the spinel structure Co_3O_4.[22] The synthesized nanostructures that can selectively expose such facets are particularly beneficial for their catalytic activity. Xie *et al.* reported that Co_3O_4 nanorods were much less sensitive to water and highly active for CO oxidation at low temperature (-77^{o}C) using normal feed gas (3-10 ppm moisture).[14] The predominant exposure of (110) facets, which enriched active species of Co^{3+} on the surfaces along nanorods, resulted in efficient interactions with CO. On the other hand, the hydrophobicity of the catalyst surface disrupts the affinity of water to the Co_3O_4 surface. For example, Co_3O_4 coated with hydrophobic polydimethylsiloxane can prevent deactivation of catalysts in the presence of water.[10] However, the active sites/surface of these catalysts can easily be blocked by hydrophobic coatings, thus decreasing catalytic efficiency.

In the present study we report a facile and robust wet-chemical approach to synthesize Co_3O_4@CNT with high catalytic activity for CO oxidation. Carbon nanotubes (CNTs) with large surface area have been widely used as 1-dimensional substrates to support the growth of various nanostructured Co_3O_4.[23-32] Our synthetic route, herein, is based on the *in situ* growth of ultrafine Co_3O_4 nanoparticles (NPs) on pristine multi-walled CNTs (**Figure 2.2**), without any covalent functionalization or chemical oxidation of the CNT surface. By controlling hydrophobicity of CNT substrates other than direct surface modification of the Co_3O_4 catalytic centers, Co_3O_4@CNT catalysts are markedly active for CO oxidation and 100% CO conversion is achieved using moisture-saturated (~3%) feed gas. Our approach thus stands out as a promising pathway to synthesize highly efficient catalysts on CNTs. These materials may ultimately present new opportunities to improve the moisture resistance of metal oxide catalysts for CO oxidation.

2.3 Experimental Section

2.3.1 Materials

All chemical reagents were purchased from Aldrich and used without further purification unless otherwise noted. 2-(2-Methoxyethoxy)ethyl methacrylate (MEO_2MA, 95%), *tert*-butyl acrylate (98%) and styrene (99.9%) were passed through a basic aluminum oxide column prior to use. Azobisisobutyronitrile (AIBN) was recrystallized from ethanol. Pristine multi-walled CNTs (Southwest Nanotechnologies Inc.) with diameters of ~10 nm and aspect ratio > 350-550 were used as received. Commercial Co_3O_4 (99.5%) was obtained from Strem Chemical Inc. and used as received.

2.3.2 Polymer Synthesis and Characterizations

2.3.2.1 Synthesis of $PMEO_2MA$ macroRAFT chain transfer agent ($PMEO_2MA_{84}$-CTA)

The block copolymers were synthesized through two-step RAFT polymerization procedures as reported (see **Scheme 2.1**). To prepare $PMEO_2MA$-CTA, MEO_2MA (18.8 g, 0.1 mol), CPDB (737 mg, 3.3 mmol) and AIBN (135 mg, 0.825 mmol) were dissolved in 10 mL of anisole (99%, anhydrous) in a 50 mL flask. The mixture was then degassed under vacuum for 10 min and refilled with nitrogen three times. After that, the flask was placed in a pre-heated oil bath at 60^{o}C for 15 hrs. The solution was then cooled down to room temperature and the polymer was precipitated in cold hexane three times and dried under vacuum at 40^{o}C for 24 h. From GPC measurements using polystyrene (PS) standards, the polymer sample has a M_n(GPC) of 12.5 Kg/mol and a polydispersity index (PDI, M_w/M_n) = 1.21. From the ^{1}H NMR spectrum (in $CDCl_3$), the NMR-based M_n(NMR) is 16.7 Kg/mol, by comparing the integrals of the resonance peaks of aromatic ring in CPDB (7.4-7.9 ppm) and the side methylene groups of MEO_2MA (4.1 ppm).

2.3.2.2 Synthesis of $PMEO_2MA_{84}$-b-$P(St_{61}$-co-$tBA_5)$

To synthesize diblock copolymer of $PMEO_2MA$-*b*-P(St-*co*-*t*BA), $PMEO_2MA$-CTA (1.25 g, 0.1 mmol), styrene (2.08 g, 20 mmol), *tert*-Butyl acrylate (1.28 g, 0.01 mol) and AIBN (1.64 mg, 0.01 mmol) were dissolved in 5 mL of anisole in a 10 mL flask. The reaction mixture was degassed under vacuum for 10 min and refilled with nitrogen three times. The flask was then placed in a pre-heated oil bath at 85^{o}C for 10 h. After polymerization, the solution was cooled down to room temperature and the polymer was precipitated in cold hexane three times and dried under vacuum at 40^{o}C for 24 h. From GPC measurements, the polymer sample has a M_n(GPC) of 38.5 Kg/mol and a polydispersity index (M_w/M_n) PDI= 1.22. From the ^{1}H NMR spectrum (in $CDCl_3$), the NMR-

based M_n(NMR) is 23.7 Kg/mol, using the integrals of the resonance peaks of aromatic rings of the PS block (6.4-7.3 ppm).

2.3.2.3 Synthesis of $PMEO_2MA_{84}$-b-$P(St_{61}$-co-$AA_5)$ by the hydrolysis of $PMEO_2MA_{84}$-b-$P(St_{61}$-co-$tBA_5)$

$PMEO_2MA_{84}$-*b*-$P(St_{61}$-*co*-*t*$BA_5)$ (0.5 g) was dissolved in dichloromethane (10 mL) in a 20 mL vial, followed by the addition of trifluoroacetic acid (2 mL). After stirring at room temperature for 72 h, the solvent was removed by vacuum. The polymer was then dissolved in 10 mL of THF and precipitated in cold hexane three times. After drying the polymer in vacuum at 40°C, the polymer was obtained as a pink powder. The removal of *tert*-butyl groups was evidenced by the disappearance of the *tert*-butyl peak located at 1.58 ppm in the ^{1}H NMR spectrum.

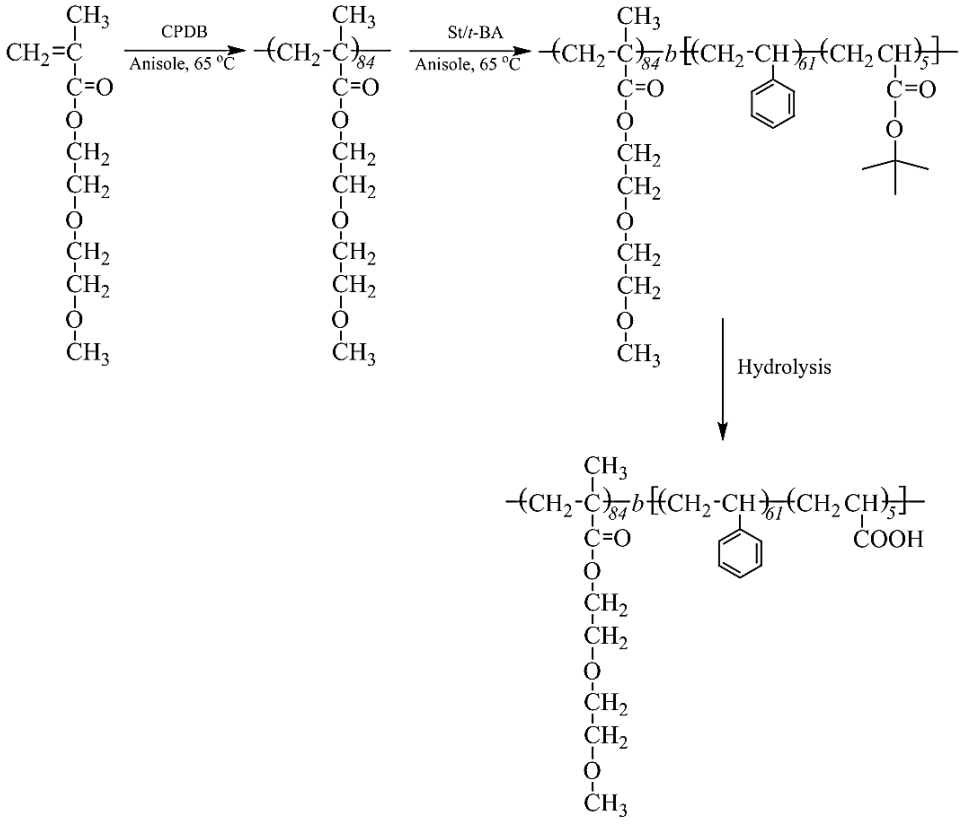

Scheme 2.1 The synthetic routes of polymers.

2.3.3 Synthesis of Co_3O_4 NPs

Co_3O_4 NPs were synthesized using a reported procedure with a slight modification.[38] Briefly, 500 mg of cobalt (II) acetate tetrahydrate (Co(II)Ac_2) as a precursor for Co_3O_4 NP growth was first dissolved in 30 mL of water/ethanol solution (1:1, vol) at 45 ^oC. Three mL of ammonium hydroxide (27-30 vol%) solution was added dropwise to the above solution under strong stirring. The reaction mixture was then heated to reflux for 3 h. After cooling down to room temperature, the reaction suspension was centrifuged at 4500 rpm for 20 min in the presence of 100 mL of acetone. The collected precipitates were redispersed in 100 mL of ethanol and washed twice with acetone by centrifugation. The final product of Co_3O_4 NPs was dried under vacuum at 60^oC.

2.3.4 Synthesis and the Fluorination of Co_3O_4@CNT

The polymer surfactant of $PMEO_2MA_{84}$-*b*-P(St_{61}-*co*-*t*AA_5) has a M_n(GPC) of 38.5 Kg/mol and a polydispersity index (M_w/M_n) PDI= 1.22. For the synthesis of Co_3O_4@CNT, 5 mg of $PMEO_2MA_{84}$-*b*-P(St_{61}-*co*-*t*AA_5) was firstly mixed with 5 mg of CNTs in 15 mL of dimethylformamide. The uniform suspension was obtained after sonication for two minutes at room temperature. About 3 mL of the suspension (~1 mg of CNTs) was then mixed with 3 mL of Co(II)Ac_2 ethanol solution (30 mg of Co(II)Ac_2 in 3 mL of ethanol). After sonication for another two minutes, 0.1 mL of ammonia hydroxide (27-30 vol%) was quickly injected into the above solution under magnetic stirring. The reaction was then heated to 85^oC and refluxed for 3 hours. After cooling down, the reaction suspension was centrifuged at 6000 rpm for 15 minutes. The collected precipitates were washed with ethanol and centrifuged another 3 times to remove the unreacted precursors and unattached Co_3O_4 NPs. The final product was dried under vacuum at 40^oC. The fluorination of Co_3O_4@CNT was performed by using the vapor phase deposition

technique. Co_3O_4@CNT (100 mg) was loaded into a 100 mL sealed jar and pretreated at 80°C for 30 min. Subsequently, 50 μL of 1H,1H,2H,2H-perfluorodecyltriethoxysilane (PFDTES) was added to a 4 mL vial and quickly loaded into a sealed jar. After 1h, 50 μL of PFDTES was added again using the above method. After silanation for another 1 h, the fluorinated Co_3O_4@CNT (F-Co_3O_4@CNT) was obtained.

2.3.5 CO Oxidation of Co_3O_4@CNT and F-Co_3O_4@CNT

The CO oxidation reaction was carried out in a continuous flow fixed bed glass tubular reactor under atmospheric pressure. As-prepared catalyst (100 mg) was used for each test. Before the measurement, the catalyst was pretreated at 200℃ for 1 h under air and another 1 h under helium flow to clean the catalyst surface. After loading the catalysts in the glass tubular reactor, a gas mixture containing 1% CO, 2% O_2 balanced in N_2 (normal feed gas) was passed through the catalyst bed. The outlet gas streams were analyzed with an online gas chromatograph (SRI 8610C Multiple Gas Analyzer #1 GC) equipped with a thermal conductivity detector (TCD), a 6 foot long molecular sieve 13X packed column, and a 6 foot long silica gel packed column. The reaction temperature was measured using a K-type thermocouple inserted directly into the catalyst bed. GC samples were injected after 10 min stabilization at any given temperature. The reaction conversion was calculated based on CO concentration, using nitrogen as an internal standard. Normal gas conditions were obtained by using the as-mixed normal feed gas (~3 ppm of water vapor). Wet conditions were obtained by passing the feed gas through a water bubbler at room temperature (~ 3% of water vapor). To protect the GC column, moisture was trapped by desiccant before the outlet gas streams entered the GC.

2.3.6 Other Characterizations

Size exclusion chromatography (SEC) measurements were performed on a Malvern system equipped with a Viscotek RI detector and D6000M column (300×8.0 mm). Dimethylformamide was used as the carrier solvent at a flow rate of 0.7 mL/min and polystyrene standards (Polymer Laboratories, Inc.) were used for calibration. The data were processed using OmniSEC software. ^{1}H NMR spectra were recorded on a Bruker Avance 300 MHz spectrometer. The crystallinity of Co_3O_4@CNT materials was characterized using a Rigaku UltimaIV powder X-ray diffractometer with Cu K_α radiation and a beam voltage of 40 kV and 44 mA beam current. High resolution transmission electron microscopy (HRTEM) studies were carried out using a JEOL 2010 transmission electron microscope with an accelerating voltage of 200 kV. The TEM samples were prepared by casting the suspension of Co_3O_4@CNT (3-5 μL in ethanol) on a carbon coated copper grid (300 mesh). Thermogravimetric analyses (TGA) were performed on a Hi-Res TA 2950 thermogravimetric analyzer with 60 mL/min of air flow from 25 to 1000℃ at a heating rate of 10℃/min. The evaluation of cobalt content on the surface of CNTs was carried out on a Varian AA-4 updated atomic absorption spectrometer (AAS) with a hollow cathode lamp and a deuterium background corrector, at the respective resonance line using an air-acetylene flame. The as synthesized samples were digested with aqua regia then filtering out insoluble CNTs. The collected filtrates were diluted with deionized water and used for analyzing the concentration of cobalt ions. The X-ray photoelectron spectra (XPS) surface analyses were performed on a PHI model 590 spectrometer with multi-probes (Physical Electronics Industries Inc.), using Al K_α radiation (λ = 1486.6 eV) as the radiation source. The powder samples were pressed on carbon tape mounted on adhesive copper tape stuck to a sample stage placed in the analysis chamber. The water contact angles (CA) were measured on a Dataphysics OCA20 contact-angle system at ambient

temperature. The sample was uniformly mounted on double sided carbon tape with one side sticking on a glass slide. Three μL of distilled water were slowly dropped onto the surface of the carbon tape coated with various samples. Reported CA values are averages of three independent measurements. Attenuated total reflection Fourier transform infrared (ATR-FTIR) spectra were recorded using a Thermo Scientific Nicolet Nicolet iS5 spectrometer by directly placing samples on a germanium crystal. The Brunauer-Emmett-Teller (BET) surface area of catalysts was measured using a Quantachrome Autosorb-1-C automated N_2 gas adsorption system. Fifty mg of samples were degassed at 150 ℃ for 12 h to remove water and other physically adsorbed species.

2.4 Results and Discussion

The *in situ* growth of Co_3O_4 NPs on CNTs was assisted by a polymer surfactant of poly(2-(2-methoxyethoxy)ethyl methacrylate ($PMEO_2MA$) and poly(styrene-*co*-acrylic acid) ($PMEO_2MA$-*b*-P(St-*co*-AA), 8 mol% of AA units in styrene block). The polymer surfactant is composed of an inert block of $PMEO_2MA$ and a functional block of P(St-*co*-AA) where styrene units can interact with CNTs through π-π interactions and carboxylic acid moieties can coordinate with Co ions via electrostatic forces.[33-36] The inert $PMEO_2MA$ block is essential to enable the good solubility of polymer surfactants under high ionic strength. For example, the polymer surfactant of $PMEO_2MA$-*b*-P(St-*co*-AA) can stabilize the suspension of CNTs even at ~30 mM of cobalt salts. In a typical synthesis, $PMEO_2MA$-*b*-P(St-*co*-AA) and CNTs (~10 nm in diameter) (1:1, wt%) were first mixed in dimethylformamide. As a result of strong π-π interactions of CNTs with aromatic rings on P(St-*co*-AA) blocks (see **Figure 2.1**), a uniform suspension could be obtained after sonication for two minutes at room

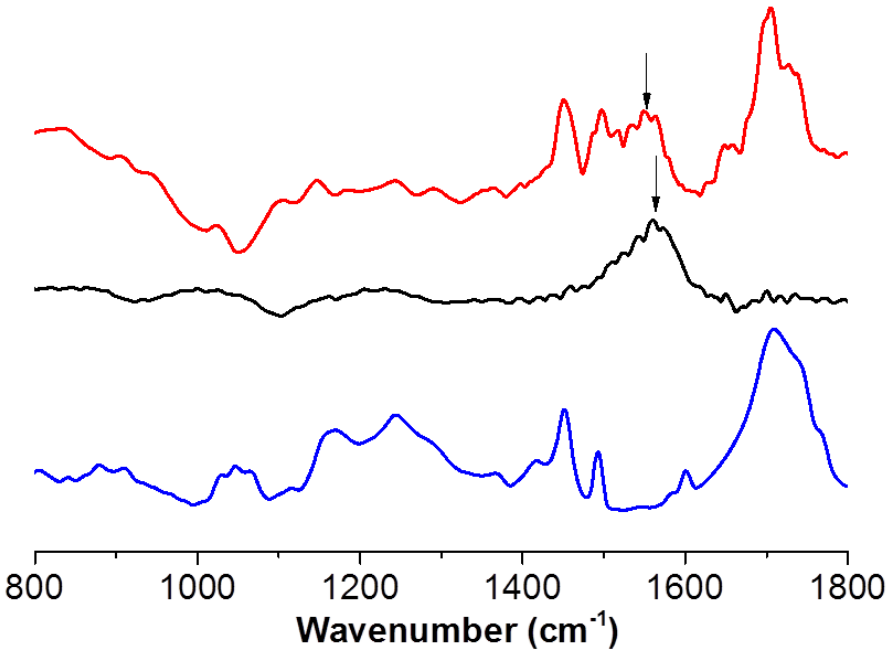

Figure 2.1 ATR-FTIR spectra of CNT/polymer composites (red, top), pristine CNTs (black, middle) and polymer surfactant (blue, bottom). The strong peak at 1710 cm^{-1} is assigned to the stretching of C=O. The peaks at 1560 to 1520 cm^{-1} are assigned C=C stretching on the nanotube body. The blue-shift of these peaks after incorporating with polymer indicates π-π interactions of polymer surfactants and CNTs.

temperature (**Figure 2.2a**).[33-36] Given the small fraction of carboxylic acid groups in P(St-*co*-AA) blocks coordinating with Co ions, the Co_3O_4 NPs can thus easily nucleate and grow on the surface of CNTs following the addition of cobalt(II) acetate and ammonium hydroxide in the mixed solvent of ethanol, dimethylformamide, and water at 80 ^oC.[37-38] Ammonia hydroxide can steadily mediate the hydrolysis and oxidation of Co ions and the loading amount of Co_3O_4 NPs on CNTs can be readily controlled by the amount of cobalt(II) acetate. Compared to the covalent functionalization treatment of CNTs where the aggressive chemical oxidations can alter the orbital hybridization of carbon atoms from sp^2 to sp^3 and disrupt the

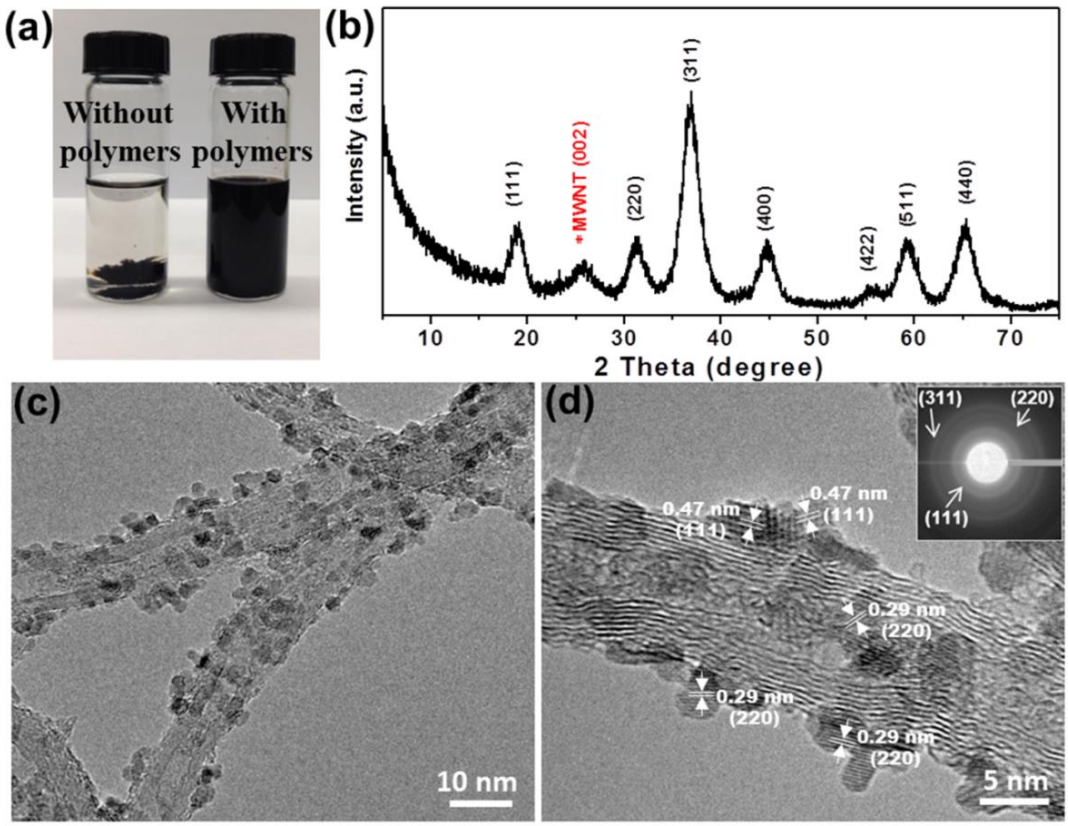

Figure 2.2 (a) The images of pristine CNTs (left) and CNTs with polymer surfactants (right) in dimethylformamide taken after sonication and stayed overnight. The CNTs can form the stable suspension in the presence of polymer surfactants. (b) Powder XRD pattern for synthesized Co_3O_4@CNT catalysts. The peak located at 26° is ascribed to CN (002) reflections. (c,d) High magnification TEM images of Co_3O_4@CNT catalysts. The measured size of Co_3O_4 NPs is 2.5±0.5 nm by averaging more than 100 NPs. The inset in (d) is the selected area electron diffraction pattern of Co_3O_4@CNT.

band-to-band transitions of π electrons of CNTs,[39-41] the non-covalent functionalization of CNTs is based on the weak π-π interactions with polymer surfactants and has the advantages of, i) simple and mild reaction conditions; ii) no strong redox reactions involved on tubular body (see Raman discussion below); and iii) facile yet general approach that can be applied to the *in situ* growth of other metal oxide NPs, *e.g.* TiO_2, Mn_3O_4, and CeO_2 (See **Figure 2.3**).

This may illustrate an alternative and simple approach for the *in situ* growth of NPs on CNT surfaces via the non-covalent bonding of polymer surfactants.

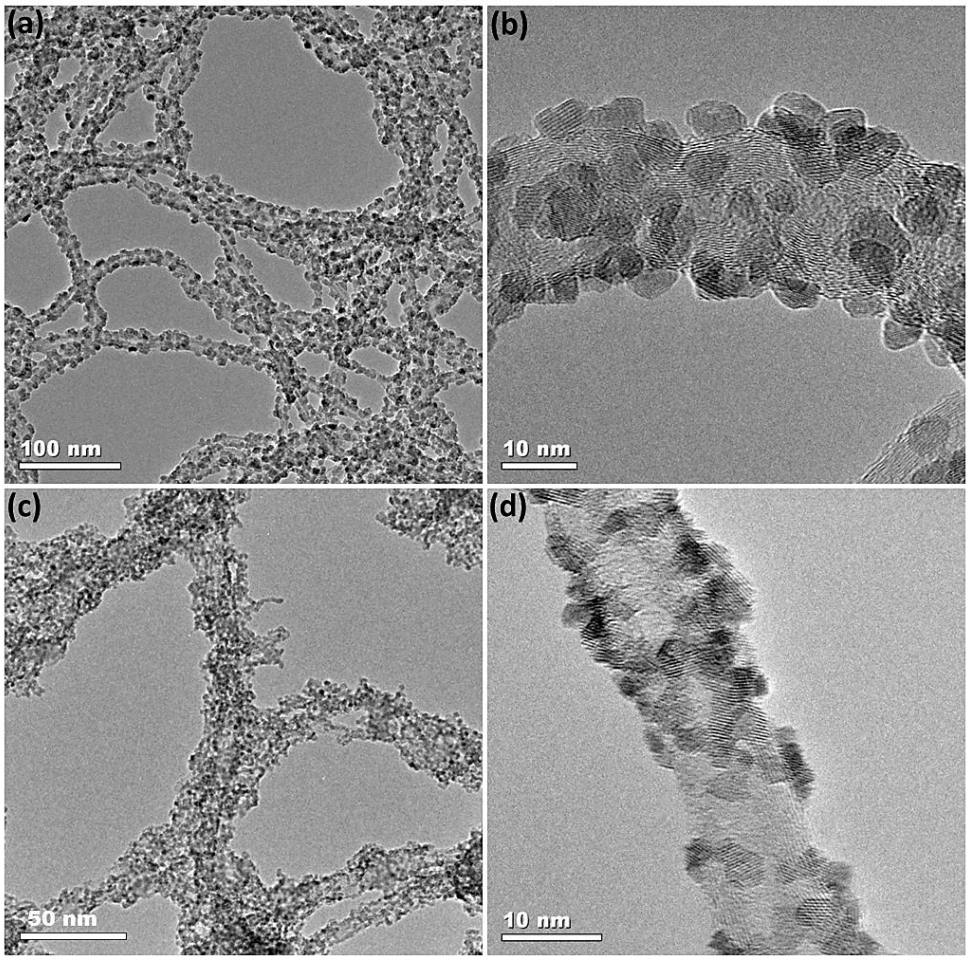

Figure 2.3 The *in situ* growth of other metal oxide NPs under similar reaction conditions. (a,b) Mn_3O_4@CNT; and (c,d) CeO_2@CNT. The average size of Mn_3O_4 particles is 6.5±1 nm and 3.8±1.5 nm for CeO_2 particles.

Figures 2.2c and **d** present representative transmission electron microscopy (TEM) images of Co_3O_4@CNT at high magnifications. Spherical Co_3O_4 NPs are uniformly decorated on CNT surfaces and they are fairly monodispersed with an average diameter of 2.5±0.5 nm. The high resolution TEM image of Co_3O_4 NPs clearly shows the crystalline nature of

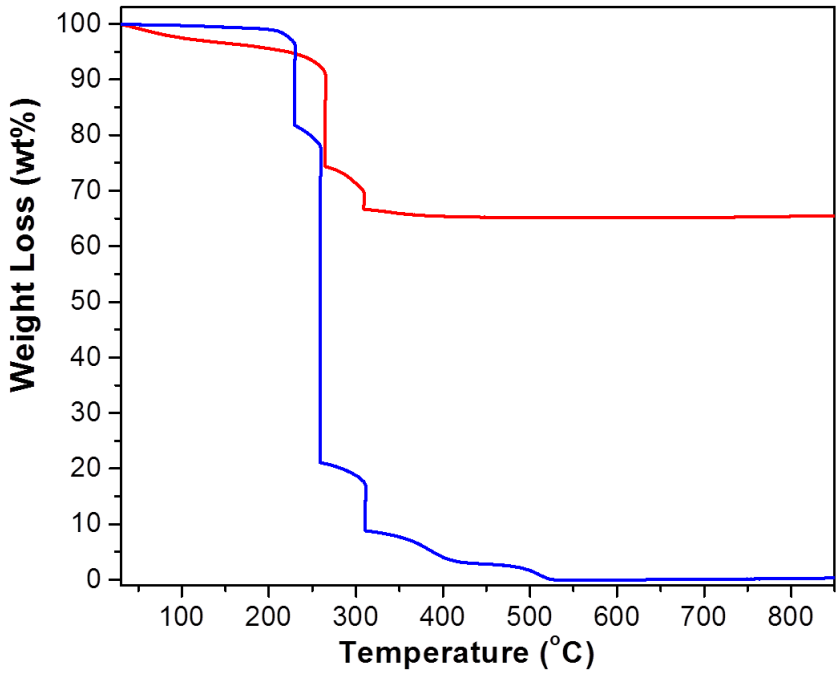

Figure 2.4 Thermogravimetric curves of polymer surfactant of $PMEO_2MA$-*b*-P(St-*co*-AA) (blue) and activated Co_3O_4@CNT catalyst (red) under atmosphere. The block copolymer thermally degrades in three stages, including the decomposition of oligo(ethyloxide) side groups of $PMEO_2MA$ blocks (200°C, the mass loss of 20 wt%), the degradation of polymer backbone (250°C, the mass loss of 60 wt%), and the degradation of residual aromatic carbons (310°C, the mass loss of 15 wt%). The mass loss of Co_3O_4@CNT catalyst (35 wt%) is clearly attributed to the degradation of polymer surfactants. The loading amount of Co_3O_4 in Co_3O_4@CNT catalyst was estimated to be ~30 wt% assuming the weight ratio of polymer and CNTs is close to 1:1. The value is slightly larger than that from atomic absorption measurements, as the mass loss of CNTs is not being taken into account.

individual Co_3O_4 NPs (**Figure 2.2d**). The interplanar distances with the *d*-spacing of 0.47 and 0.29 nm correspond to (111) and (220) facets of spinel Co_3O_4, respectively. The powder X-ray diffraction patterns in **Figure 2.2b** show strong diffraction peaks of (111), (220) and (311) facets indexed to the cubic spinel structure of Co_3O_4 NPs (JCPDS card no: 00-043-1003), in accordance with the TEM observation. The loading amount of Co_3O_4 NPs on CNTs estimated

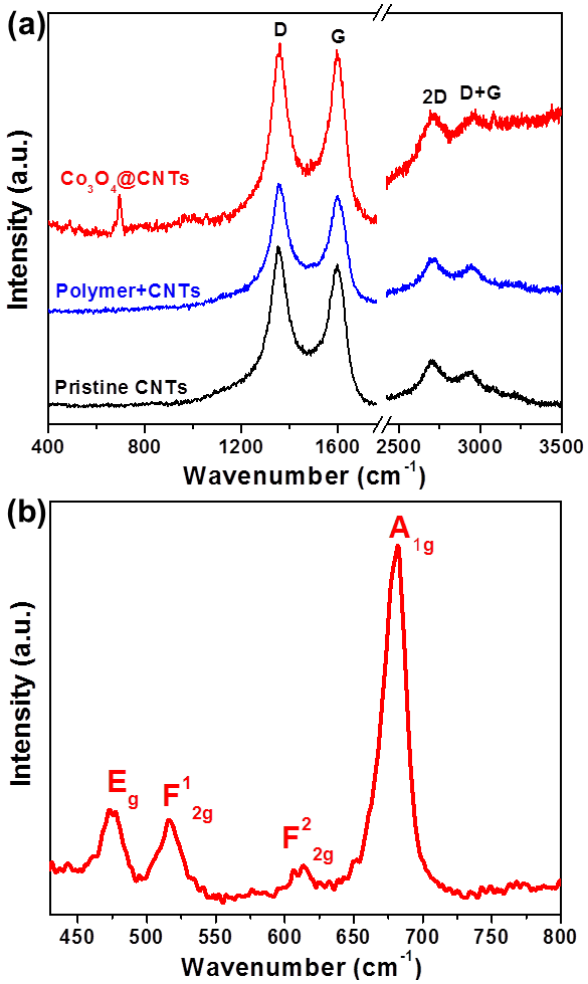

Figure 2.5 (a) Raman spectra of pristine CNTs, CNTs with polymers and Co_3O_4@CNT. The D, G, 2D and D+G bands are defect-related peaks of CNT or amorphous carbon. No shift of these peaks was observed after mixing with polymers and the growth of Co_3O_4, indicating that the surface of CNTs was not chemically modified. (b) The close observation of Raman active lattice vibrations of Co_3O_4.

from atomic absorption measurements (digesting Co_3O_4 NPs from CNTs using aqua regia solution) is approximately 43 wt%, calculated from the Co standard calibration curve. The estimated amount of Co_3O_4 on CNTs collected from atomic absorption measurements is slightly larger than thermogravimetric measurements (see **Figure 2.4**). Due to supporting the catalyst on CNTs with a very large surface-to-volume ratio, the Co_3O_4@CNT catalyst has a

BET surface area of 143 m^2/g and pore volume of 0.67 cm^3/g, notably higher than nanosized Co_3O_4 NPs and commercial Co_3O_4 materials.

The non-covalent bonding of CNTs and polymers does not alter their electronic structures, as evidenced by Raman spectra (**Figure 2.5**). The D- and G-bands of multi-walled CNTs for pristine CNTs, polymer/CNTs, and Co_3O_4@CNT appear at 1354 and 1598 cm^{-1}, respectively, assigned to the defects and disorder-induced mode and in planar E_{2g} zone-center mode.[42-43] No obvious shift of D- and G-bands of CNTs was observed after polymer modification and the growth of Co_3O_4 NPs. In addition, the intensity ratios of D- and G-bands (I_D/I_G) for pristine CNTs, polymer/CNTs, and Co_3O_4@CNT are 1.09, 1.11 and 1.06 respectively. This suggests that such non-covalent functionalization of CNTs preserves their pristine surface and does not introduce further defects on the tubular body. The formation of Co_3O_4 NPs was further confirmed by Raman spectra as well (**Figure 2.5b**). Four Raman active lattice vibrations appear at 477, 516, 612, 682 cm^{-1}, indicating the cubic spinel structure of Co_3O_4 NPs.

To investigate the catalytic activity, the obtained Co_3O_4@CNT was first pretreated by annealing at 200^oC under atmosphere for 1 h. After loading ~100 mg of activated catalyst (~43 mg of Co_3O_4) into a glass tubular reactor, the CO oxidation reaction was carried out under a continuous flow of a normal gas mixture containing 1% of CO and 2% of O_2, balanced in 97% of N_2 (space velocity of 35000 mL g^{-1} h^{-1} and 3-10 ppm moisture). The catalytic performance of Co_3O_4@CNT is given in **Figure 2.6**. A 100% conversion of CO to CO_2 was achieved at various temperatures ranging from 25 to 200 ^oC at a low O_2 concentration. The high catalytic activity is likely attributed to nano-sized Co_3O_4 particles supported on CNTs having a much larger specific surface area of 143 m^2/g and pore volume of 0.67 cm^3/g.[38, 44-46] These results suggest that more active sites on Co_3O_4@CNT catalysts can be exposed. The free Co_3O_4 NPs synthesized without CNT supports

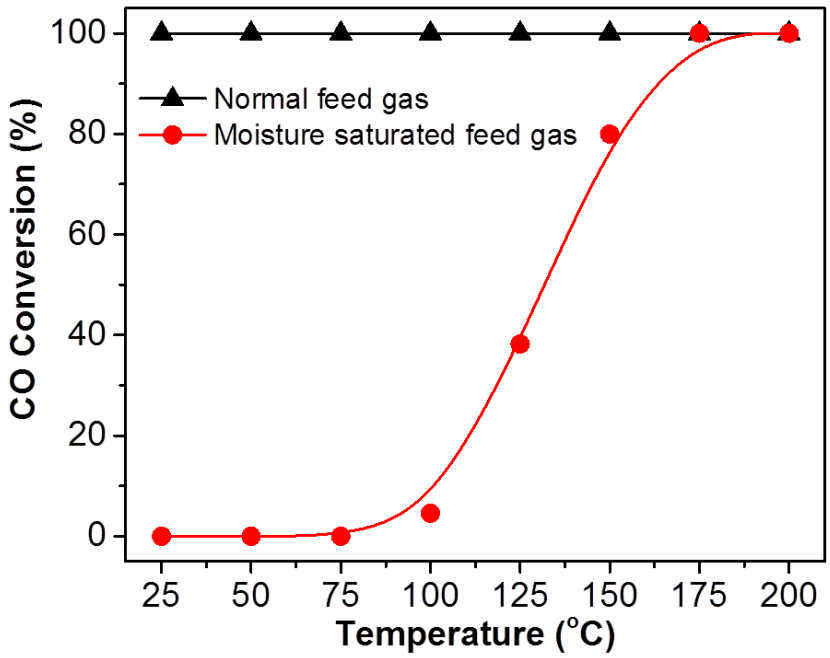

Figure 2.6 Temperature dependence of catalytic activity of Co_3O_4@CNT catalysts for CO oxidation. The CO conversion was measured and quantified by gas chromatography. Each data point was collected after stabilizing the catalysts under feed gas conditions and temperature at least 10 min.

and commercial Co_3O_4 catalysts only show little activity for CO oxidation at room temperature (see **Figures 2.7**). The T_{50} (50% CO conversion at this temperature) of free Co_3O_4 NPs and commercial Co_3O_4 catalysts is ~86°C and ~178°C, respectively. Subsequently, the Co_3O_4@CNT catalysts have been tested using moisture-saturated feed gas (~3% water) close to the water concentration of automobile exhaust (**Figure 2.6**).[47] Under such a critical environment, the light-off temperature of Co_3O_4@CNT catalysts is ~100°C and the T_{50} is ~132°C. The catalytic activity at higher temperatures (T >175°C) is not affected. When the temperature is further decreased, the CO conversion drops rapidly. For example, only 80% of CO was converted into CO_2 at T=150°C. The commercial Co_3O_4 catalysts are completely inactive under such conditions at T=200°C (see **Figures 2.7**).

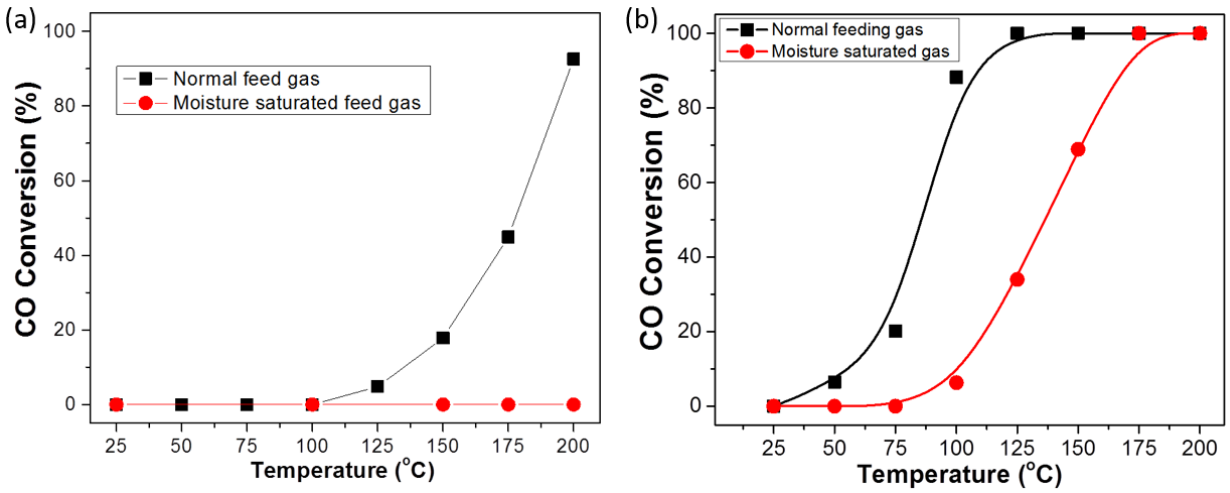

Figure 2.7 (a) Time dependent studies of CO oxidation for commercial Co_3O_4 material under normal gas and moisture saturated gas. (b) Time dependent studies of CO oxidation for synthesized Co_3O_4 NPs under normal gas and moisture saturated gas.

The surface hydrophobicity of Co_3O_4@CNT catalysts is assumed to influence the moisture resistance of catalysts. In order to further optimize moisture resistance, we have further modified the Co_3O_4@CNT surface using the fluorination of 1H,1H,2H,2H-perfluorodecyltriethoxysilane (PFDTES). The residual -COOH groups from polymers can selectively react with PFDTES to introduce fluorinated alkyl chains that alter the hydrophobicity of catalysts. Through the vapor phase deposition technique, the Co_3O_4@CNT catalysts were treated with PFDTES vapor at 80°C for 30 min. The fluorinated coating on the surface of Co_3O_4@CNT is further confirmed by X-ray photoelectron spectra (XPS) (**Figures 2.8**). The F 1s peak at 688 eV is assigned to fluorinated alkyl chains of PFDTES.[48] The Co $2p_{1/2}$ and $2p_{3/2}$ areas did not show any significant differences following the fluorination treatment, indicating that the terminal silane groups of PFDTES are bonded to CNT substrates other than Co_3O_4 NPs.[49] The fact that the active sites on Co_3O_4 were preserved is particularly important.

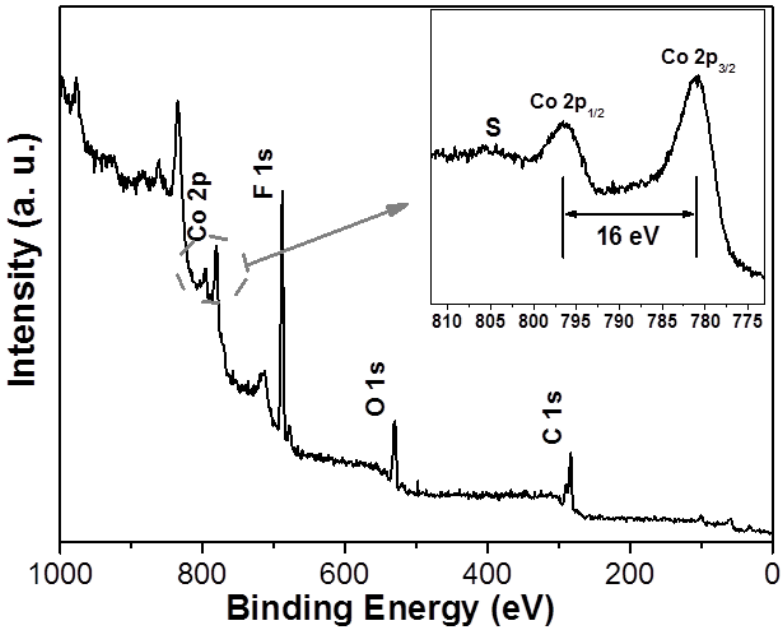

Figure 2.8 X-ray photoelectron spectrum of F-Co_3O_4@CNT catalysts. The appearance of F 1s signals at 688 eV is assigned to the PFDTES coating. The inset is the Co 2p signals, correlated to Co $2p_{3/2}$ (780.8 eV) and Co $2p_{1/2}$ (796.5 eV) peaks.

Figure 2.9 presents the CO conversion curves of F-Co_3O_4@CNT at various temperatures. Again, when using normal feed gas, 100% CO conversion was obtained at various temperatures. This confirms that the fluorination of Co_3O_4@CNT did not shield the surface of Co_3O_4, therefore not preventing adsorption of CO and O_2 on the catalytic center. Under saturated moisture, the shift of CO conversion curve to lower temperature is obvious compared to bare Co_3O_4@CNT catalysts. The light-off temperature of F-Co_3O_4@CNT catalysts is ~40^{o}C and T_{50} is ~110^{o}C, corresponding to a 22^{o}C decrease as compared to that of non-fluorinated Co_3O_4@CNT. At T=150^{o}C, the CO conversion can still reach 100% for F-Co_3O_4@CNT. This is the lowest light-off and T_{100} temperature of Co_3O_4 NPs under saturated moisture so far. The improved moisture-resistance of F-Co_3O_4@CNT is attributed to the increase in surface hydrophobicity of catalysts that prevents water accumulation on the surface of Co_3O_4 active sites.

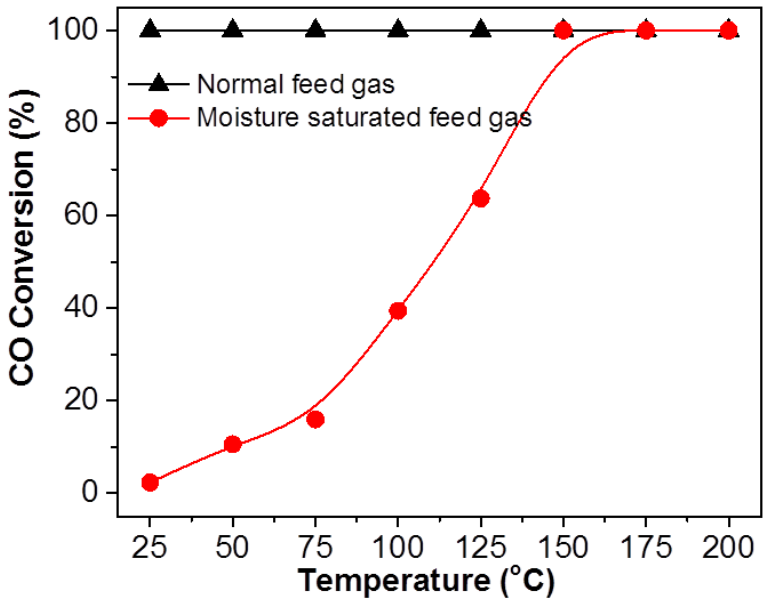

Figure 2.9 Temperature dependence of catalytic activity of F-Co_3O_4@CNT catalysts for CO oxidation. The CO conversion was measured and quantified by gas chromatography. Each data point was collected after stabilizing the catalysts under feed gas conditions and temperature at least 10 min.

The changes of surface hydrophobicity of catalysts were confirmed by water contact angle measurements. The powder samples of catalysts were pressed onto carbon tape mounted on adhesive copper tape stuck to form a condensed film. From water contact angles (**Figure 2.10a-c**), our Co_3O_4@CNT catalysts having a contact angle of 108.8° are more hydrophobic than pure Co_3O_4 particles which have a contact angle of 86.1°. The surface hydrophobicity of CNTs slightly improved the moisture resistance of catalysts, as evidenced by 100% of CO conversion achieved in the presence of 3-10 ppm moisture. However, the hydrophobicity is not high enough to repel the moisture at higher water content (3% of moisture). After surface treatment by PFDTES, the contact angle of fluorinated Co_3O_4@CNT (F-Co_3O_4@CNT) further increased to 142.4° (**Figure 2.10c**), indicating the superhydrophobicity of F-Co_3O_4@CNT. The fluorinated alkyl chains of

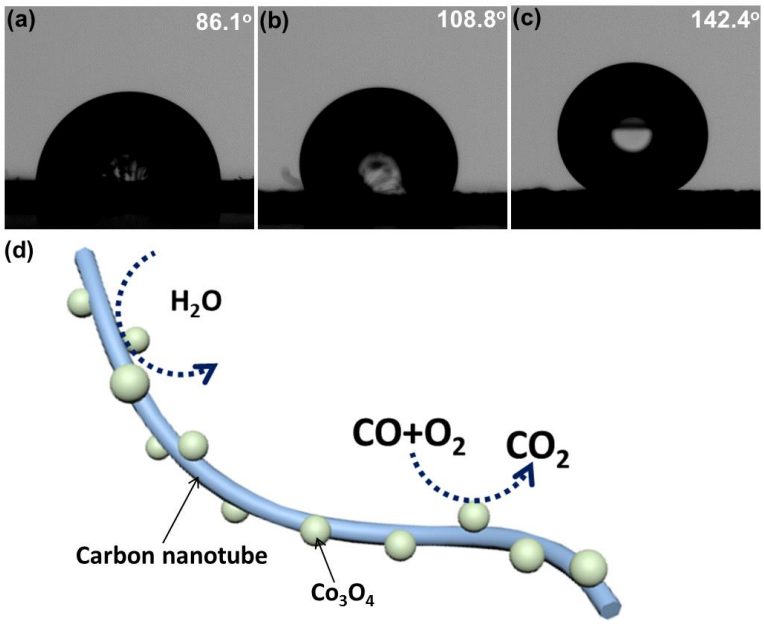

Figure 2.10 (a-c) The contacting angle measurements of commercial Co_3O_4 (a), Co_3O_4@CNT (b) and F-Co_3O_4@CNT (c) catalysts**.** (d) Schematic illustration of surface hydrophobicity of catalysts preventing water accumulation on the surface of catalysts.

PFDTES can form a hydrophobic layer on CNTs that enhances hydrophobicity of F-Co_3O_4@CNT. The hydrophobic layer does not block the active sites on Co_3O_4 as evidenced by catalytic activity of F-Co_3O_4@CNT with normal feed gas. Thus, the improved hydrophobicity of CNT substrate only shields the moisture from the active sites, resulting in the decrease of light-off and T_{50} temperature for F-Co_3O_4@CNT (**Figure 2.10d**).

To gain further insight on the effect of surface properties, we have examined the kinetics of moisture deactivation of two catalysts. **Figure 2.11** presents a time-resolved study of catalytic performance of Co_3O_4@CNT and F-Co_3O_4@CNT at 150 and 100°C as a function of water exposure time. At T=150°C, F-Co_3O_4@CNT showed high catalytic performance and 100% CO conversion was reached regardless of the water exposure time. The bare Co_3O_4@CNT showed a continuous decrease of CO conversion when the water exposure time was increased to 30 min.

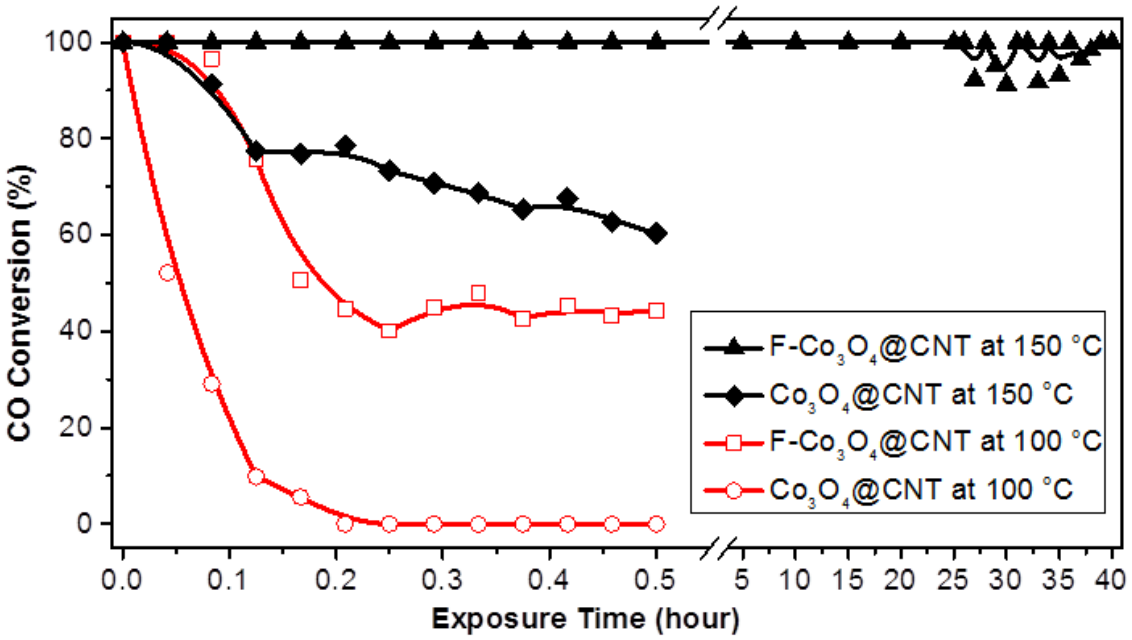

Figure 2.11 Time-resolved study of catalytic performance of Co_3O_4@CNT and F-Co_3O_4@CNT at 150°C and 100°C using the moisture saturated feed gas. For the long term stability test, the moisture saturated gas were keeping pass through catalysts and the moisture was removed before measurement of the CO conversion.

This suggests that water can still accumulate around the catalytic centers and gradually deactivate the catalysts. At this point, the turnover frequency of F-Co_3O_4@CNT is 3.31×10^{-4} s^{-1}, which is nearly twice as high as 1.86×10^{-4} s^{-1} of Co_3O_4@CNT (based on the total mass of Co ions). When the temperature dropped to 100°C, the CO conversion of F-CO_3O_4@CNT decreased in the first 10 min and remained at ~50%. Co_3O_4@CNT, on the other hand, quickly deactivated within 10 min. This observation implies that the water adsorption rate on the CO_3O_4@CNT catalyst surface is higher than the water desorption rate at 100°C; the accumulation of water would gradually passivate the catalytic sites. On the contrary, the adsorption rate on the F-CO_3O_4@CNT is much lower due to the surface hydrophobicity and water does not accumulate.

Finally, the long-term stability of F-Co_3O_4@CNT catalysts was studied at 150°C under moisture-saturated conditions (**Figure 2.11**). The catalytic activity of F-Co_3O_4@CNT is extremely stable. This catalyst gave 100% conversion of CO after 26 h and a small fluctuation of CO conversion appeared after that. The loss of stability is probably due to partial detaching/degradation of fluorinated PFDTES on the catalyst surface, as well as accumulation of carbonate species on the surface. The nanostructure of catalysts did not change after the catalytic tests at 150°C for 40 h (data not shown). Overall, the F-Co_3O_4@CNT catalysts have shown high durability of CO conversion under a harsh environment.

Table 2.1 Turnover frequency of the Co_3O_4@CNT for CO oxidation under different conditions.[a]

Temperature (°C)	TOF (s^{-1}) [b]	
	Co_3O_4@CNT	F-Co_3O_4@CNT
r.t. (normal gas)	3.10×10^{-4}	3.31×10^{-4}
r.t. (~3% water)	0	7.63×10^{-6}
50 °C (~3% water)	0	3.49×10^{-5}
75 °C (~3% water)	0	5.27×10^{-5}
100 °C (~3% water)	1.43×10^{-5}	1.27×10^{-4}
125 °C (~3% water)	1.19×10^{-4}	2.11×10^{-4}
150 °C (~3% water)	2.48×10^{-4}	3.31×10^{-4}
175 °C (~3% water)	3.10×10^{-4}	3.31×10^{-4}
200 °C (~3% water)	3.10×10^{-4}	3.31×10^{-4}

[a] The turnover frequency values were measured with continues flow of 1.0 vol% of CO, 2.0 vol% of O_2, and N_2 was used as carrier gas and internal standard. The total weight hourly space velocity (WHSV) was 3.5×10^4 in mL g^{-1} h^{-1}. Normal gas (~3 ppm of water) and water saturated gas (~3% of water) were used in order to determine the water tolerance ability of the catalysts. [b] Turnover frequencies were calculated based on the total Co ions contained in the Co_3O_4 NPs used in the system.

2.5 Conclusion

In summary, we have developed a polymer-assisted, facile synthesis of highly active Co_3O_4@CNT catalysts for CO oxidation under moisture-rich conditions. The modulation of surface hydrophobicity of CNT substrates was demonstrated to be an efficient method to enhance the moisture resistance of metal oxide catalysts for CO oxidation. Using moisture-saturated feed gas, the fluorinated Co_3O_4@CNT exhibited an outstanding activity and durability at 150ºC. This approach is simple, fast, yet general, and can be potentially applied to other types of metal oxide catalysts. This research may open up a new realm of possibilities in developing inexpensive and moisture-resistant metal oxide catalysts for CO oxidation.

2.6 References

(1) Pommier, M.; McLinden, C. A.; Deeter, M. *Geophys. Res. Lett.* **2013**, *40,* 3766-3771.

(2) Min, B. K.; Friend, C. M. *Chem. Rev.* **2007**, *107,* 2709-2724.

(3) Imanaka, N.; Masui, T.; Imadzu, H.; Yasuda, K. *Chem. Commun.* **2011**, *47,* 11032-11034.

(4) Carrettin, S.; Concepción, P.; Corma, A.; López Nieto, J. M.; Puntes, V. F. *Angew. Chem. Int. Ed.* **2004**, *43,* 2538-2540.

(5) Comotti, M.; Li, W.-C.; Spliethoff, B.; Schüth, F. *J. Am. Chem. Soc.* **2006**, *128*, 917-924.

(6) Liu, L. M.; McAllister, B.; Ye, H. Q.; Hu, P. *J. Am. Chem. Soc.* **2006**, *128*, 4017-4022.

(7) Gong, J.; Mullins, C. B. *J. Am. Chem. Soc,* **2008**, *130,* 16458-16459.

(8) Herzing, A. A.; Kiely, C. J.; Carley, A. F.; Landon, P.; Hutchings, G. J. *Science* **2008**, *321*, 1331-1335.

(9) Royer, S.; Duprez, D. *ChemCatChem* **2011**, *3*, 24-65.

(10) Chen, C.-H.; Njagi, E. C.; Sun, S.-P.; Genuino, H.; Hu, B.; Suib, S. L. *Chem. Mater.* **2010**, *22*, 3313-3315.

(11) Jansson, J.; Palmqvist, A. E. C.; Fridell, E.; Skoglundh, M.; Ö sterlund, L.; Thormählen, P.; Langer, V. *J. Catal.* **2002**, *211*, 387-397.

(12) Dangwal Pandey, A.; Jia, C.; Schmidt, W.; Leoni, M.; Schwickardi, M.; Schüth, F.; Weidenthaler, C. *J. Phys. Chem. C* **2012**, *116*, 19405-19412.

(13) Jiang, D.-e.; Dai, S. *Phys. Chem. Chem. Phys.* **2011**, *13*, 978-984.

(14) Xie, X.; Li, Y.; Liu, Z.-Q.; Haruta, M.; Shen, W. *Nature* **2009**, *458*, 746-749.

(15) Sun, Y.; Lv, P.; Yang, J.-Y.; He, L.; Nie, J.-C.; Liu, X.; Li, Y. *Chem. Commun.* **2011**, *47*, 11279-11281.

(16) Teng, Y.; Kusano, Y.; Azuma, M.; Haruta, M.; Shimakawa, Y. *Catal. Sci. Technol.* **2011**, *1*, 920-922.

(17) Wang, Y.-Z.; Zhao, Y.-X.; Gao, C.-G.; Liu, D.-S. *Catal. Lett.* **2007**, *116*, 136-142.

(18) Yan, N.; Chen, Q.; Wang, F.; Wang, Y.; Zhong, H.; Hu, L. *J. Mater. Chem. A* **2013**, *1*, 637-643.

(19) Yu, Y.; Takei, T.; Ohashi, H.; He, H.; Zhang, X.; Haruta, M. *J. Catal.* **2009**, *267*, 121-128.

(20) Poyraz, A. S.; Kuo, C.-H.; Biswas, S.; King'ondu, C. K.; Suib, S. L. *Nat. Commun.* **2013**, *4*, 29521-295210.

(21) Lin, H. K.; Chiu, H. C.; Tsai, H. C.; Chien, S. H.; Wang, C. B. *Catal. Lett.* **2003**, *88*, 169-174.

(22) Sun, H.; Ang, H. M.; Tade, M. O.; Wang, S. Co_3O_4 *J. Mater. Chem. A* **2013**, *1*, 14427-14442.

(23) Liang, Y.; Wang, H.; Diao, P.; Chang, W.; Hong, G.; Li, Y.; Gong, M.; Xie, L.; Zhou, J.; Wang, J.; Regier, T. Z.; Wei, F.; Dai, H. *J. Am. Chem. Soc.* **2012**, *134*, 15849-15857.

(24) Wu, J.; Xue, Y.; Yan, X.; Yan, W.; Cheng, Q.; Xie, Y. *Nano Res.* **2012**, *5*, 521-530.

(25) Zhuo, L.; Wu, Y.; Ming, J.; Wang, L.; Yu, Y.; Zhang, X.; Zhao, F. *J. Mater. Chem. A* **2013**, *1*, 1141-1147.

(26) He, X.; Wu, Y.; Zhao, F.; Wang, J.; Jiang, K.; Fan, S. *J. Mater. Chem. A* **2013**, *1*, 11121-11125.

(27) Lu, X.; Zhao, C. *J. Mater. Chem. A* **2013**, *1*, 12053-12059.

(28) Xu, M.; Wang, F.; Zhang, Y.; Yang, S.; Zhao, M.; Song, X. *Nanoscale* **2013**, *5*, 8067-8072.

(29) Yoon, T. H.; Park, Y. J. *J. Power Sources* **2013**, *244*, 344-353.

(30) Du, N.; Zhang, H.; Chen, B.; Wu, J. B.; Ma, X. Y.; Liu, Z. H.; Zhang, Y. Q.; Yang, D.; Huang, X. H.; Tu, J. P. *Adv. Mater.* **2007**, *19*, 4505-4509.

(31) Fu, L.; Liu, Z.; Liu, Y.; Han, B.; Hu, P.; Cao, L.; Zhu, D. *Adv. Mater.* **2005**, *17*, 217-221.

(32) Shan, Y.; Gao, L. *Mater. Chem. Phys.* **2007**, *103*, 206-210.

(33) Suzuki, T.; Yan, X.; Kitahama, Y.; Sato, H.; Itoh, T.; Miura, T.; Ozaki, Y. *J. Phys. Chem. C* **2012**, *117*, 1436-1440.

(34) Kang, Y.; Taton, T. A. *J. Am. Chem. Soc.* **2003**, *125*, 5650-5651.

(35) Gonzalez-Dominguez, J. M.; Tesa-Serrate, M. A.; Anson-Casaos, A.; Diez-Pascual, A. M.; Gomez-Fatou, M. A.; Martinez, M. T. *J. Phys. Chem. C* **2012**, *116*, 7399-7408.

(36) Gerstel, P.; Klumpp, S.; Hennrich, F.; Poschlad, A.; Meded, V.; Blasco, E.; Wenzel, W.; Kappes, M. M.; Barner-Kowollik, C. *ACS Macro Lett.* **2014**, *3*, 10-15.

(37) Dong, Y.; He, K.; Yin, L.; Zhang, A. *Nanotechnology* **2007**, *18*, 4356021-4356026.

(38) Grzelczak, M.; Zhang, J.; Pfrommer, J.; Hartmann, J.; Driess, M.; Antonietti, M.; Wang, X. *ACS Catal.* **2013**, *3*, 383-388.

(39) Britz, D. A.; Khlobystov, A. N. *Chem. Soc. Rev.* **2006**, *35*, 637-659.

(40) Karousis, N.; Tagmatarchis, N.; Tasis, D. *Chem. Rev.* **2010**, *110*, 5366-5397.

(41) Banerjee, S.; Hemraj-Benny, T.; Wong, S. S. *Adv. Mater.* **2005**, *17*, 17-29.

(42) Gao, C.; Jin, Y. Z.; Kong, H.; Whitby, R. L. D.; Acquah, S. F. A.; Chen, G. Y.; Qian, H. H.; Hartschuh, A.; Silva, S. R. P.; Henley, S.; Fearon, P.; Kroto, H. W.; Walton, D. R. M. *J. Phys. Chem. B* **2005**, *109*, 11925-11932.

(43) Deng, S.; Zhang, Y.; Brozena, A. H.; Mayes, M. L.; Banerjee, P.; Chiou, W.-A.; Rubloff, G. W.; Schatz, G. C.; Wang, Y. *Nat. Commun.* **2011**, *2*, 3821-3826.

(44) Esswein, A. J.; McMurdo, M. J.; Ross, P. N.; Bell, A. T.; Tilley, T. D. *J. Phys. Chem. C* **2009**, *113*, 15068-15072.

(45) Casas-Cabanas, M.; Binotto, G.; Larcher, D.; Lecup, A.; Giordani, V.; Tarascon, J. M. *Chem. Mater.* **2009**, *21*, 1939-1947.

(46) Hu, L. H.; Peng, Q.; Li, Y. D. *J. Am. Chem. Soc.* **2008**, *130*, 16136-16137.

(47) Heck, R. M.; Farrauto, R. J. *Appl. Catal. A-Gen.* **2001**, *221*, 443-457.

(48) Chun, S.-J.; Lee, S.-Y.; Jeong, G.-Y.; Kim, J. H. *J. Ind. Eng. Chem.* **2012**, *18*, 1122-1127.

(49) Jia, C.-J.; Schwickardi, M.; Weidenthaler, C.; Schmidt, W.; Korhonen, S.; Weckhuysen, B. M.; Schüth, F. *J. Am. Chem. Soc.* **2011**, *133*, 11279-11288.

Chapter 3. Heterogeneous Acidic TiO_2 Nanoparticles for Efficient Conversion of Biomass Derived Carbohydrates.

3.1 Overview and Abstract

Selective conversion of biomass derived carbohydrates into fine chemicals is of great significance for the replacement of petroleum feedstock and the reduction of environmental impacts. Levulinic acid, 5-hydroxymethyl furfural (HMF) and their derivatives are recognized as important precursor candidates in a variety of different areas. In this study, the synthesis, characterization, and catalytic activity of acidic TiO_2 nanoparticles in the conversion of biomass derived carbohydrates were explored. This catalyst was found to be highly effective for selective conversion to value-added products. The nanoparticles exhibited superior activity and selectivity towards methyl levulinate from fructose in comparison to current commercial catalysts. The conversion of fructose to methyl levulinate was achieved with 80 % yield and high selectivity (up to 80 %). Additionally, conversions of disaccharides and polysaccharides were studied. Further, the production of versatile valuable products such as levulinic esters, HMF, and HMF-derived ethers was demonstrated using the TiO_2 nano-sized catalysts in different solvent systems.

3.2 Introduction

Since the use of fossil fuels as feedstock for fine chemical synthesis and energy resources is approaching unsustainable levels, the development of innovative strategies and resources for the sustainable production of fuels and chemicals from renewable materials are stimulating interest.[1-4] Among these resources, biomass has attracted enormous attention due to its considerable

potential as a raw material for the production of green fine chemicals, fuels and fuel additives.[5] Therefore, it is highly desirable to convert carbohydrates to platform molecules selectively under mild conditions, which can subsequently be used for the production of various chemicals. The typical approach for biomass degradation involves acid-catalyzed hydrolysis[6] followed by either chemical or biological conversion to monosaccharides.[7] For example, glucose produced from cellulose through hydrolysis in an aqueous medium can be transformed to useful molecules such as alkyl glucosides, 5-hydroxymethyl furfural (HMF),[8] levulinic acid, and gluconic acid.[9] Among these valuable molecules, levulinic acid and ester derivatives are among the most promising building blocks in a biomass refinery. Levulinic acid and its esters are classified as some of the top 12 valuable chemicals converted from biomass according to the US Department of Energy's National Renewable Energy Laboratory (NREL).[10] Levulinic acid can also be converted into other useful chemicals such as acrylic acid, succinic acid, pyrrolidines, and diphenolic acid.[11, 12]

A traditional approach to the synthesis of levulinic acid from biomass-derived carbohydrates requires the use of homogeneous mineral acids such as sulfuric acid and metal chloride salts.[13-16] The use of homogeneous catalysts for biomass conversion has been extensively studied and is known to be highly effective. However, there are several drawbacks to this approach, including catalyst separation, reactor corrosion, and recyclability. Recently, there have been several studies conducted regarding direct synthesis of platform molecules from biomass-derived feedstock such as cellulose[17], saccharides[18], and furfuryl alcohol[19] using various acids and solvents. Essayem et al. proposed a method for the direct synthesis of methyl levulinate from cellulose using solid acids in supercritical MeOH.[17c] Wang and co-workers developed an acid and metal free method for converting fructose to HMF using an ionic liquid system.[18d] Mascal et al. investigated the process of producing HMF derived ethers and levulinic acid by 5-(chloromethyl)furfural (CMF).[19d]

Furthermore, Tominaga et al. explored the Lewis and Brønsted mixed-acid systems as an efficient way to synthesize methyl levulinate.[17d] Despite all of the afore-mentioned progress, development of novel heterogeneous, cost-effective and efficient catalysts for direct synthesis of platform molecules from biomass resources is imperative for the production of useful chemicals from biomass resources.

The proposed synthetic pathways[20] for the direct conversion of monosaccharides using acid catalysts are shown in **Scheme 3.1**. The reaction starts with the isomerization of glucose to fructose followed by the Brønsted-acid-catalyzed dehydration to produce HMF. Subsequent rehydration of HMF yields levulinic acid. Further reaction of these acids (levulinic or formic acids) with alcohols can produce acid esters. HMF also reacts with alcohols to form HMF derived ethers under specific conditions. The control of the acid type on the catalyst surface is crucial for its selectivity, since different acid types determine the formation of different products. Several solid acids have been widely utilized to convert carbohydrates, such as zeolites,[21] metal oxides,[22] polymer based acids,[20] and heteropoly acids.[23] Although solid acids are more easily separated, recycled, and environmentally benign, there are still considerable opportunities for improving the selectivity and mass transfer limitations between the insoluble polymers and heterogeneous catalysts.

Herein, we report the facile synthesis of acidic TiO_2 nanoparticles that can be used as catalysts in biomass derived carbohydrate conversion. In addition, several other solid acids such as zeolites, polymer based acids, and sulfated metal oxides were chosen for comparison. Detailed process parameters including reaction time, temperature, catalyst loading, and the reusability of the catalyst were investigated in terms of catalytic performance. Moreover, different carbohydrate sources and solvents were studied.

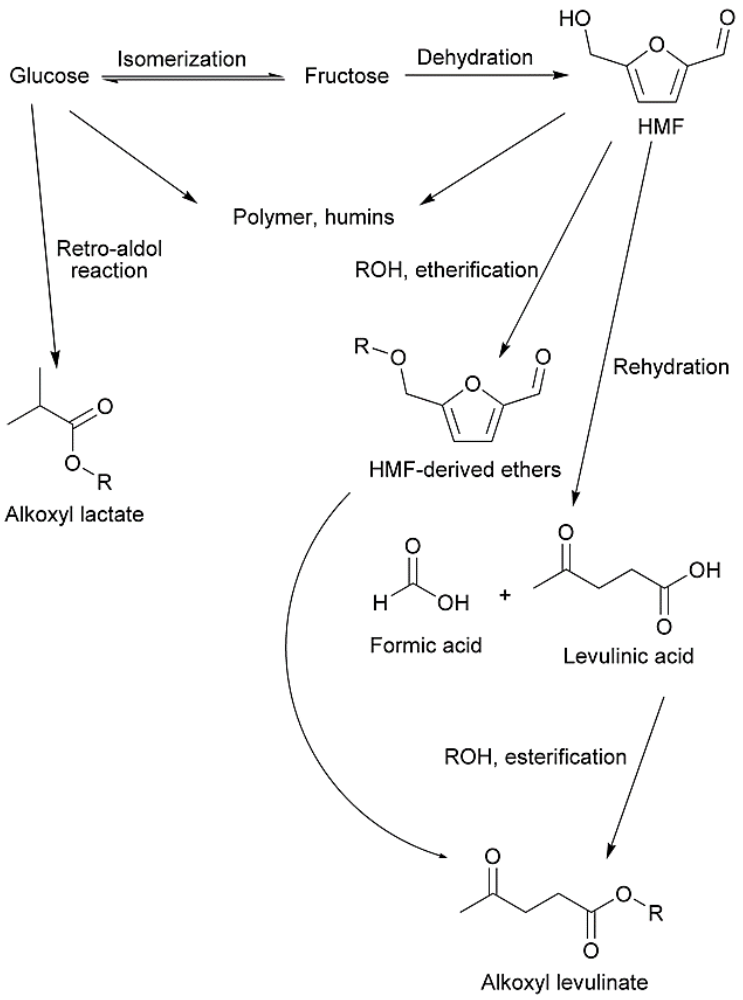

Scheme 3.1 Proposed reaction pathway for the conversion on carbohydrates to platform molecules.

3.3 Experimental Section

3.3.1 Catalyst Preparation

All chemicals were purchased from Sigma-Aldrich and used without further purification. P-25 were purchased from Degussa Inc.. H-ZSM5 (Si/Al = 50) and H-Beta (Si/Al = 30) were purchased from Zeolyst Inc. and calcined at 550 ℃ before use. Sulfated ZrO_2 and TiO_2 were made from the corresponding hydroxides prepared by hydrolysis of a 0.4 M aqueous solution of the metal

precursor with NH_4OH (25 wt% in water) at r.t. under vigorous stirring, at a given final pH of ~ 10. The hydroxides were then impregnated (via an incipient wetness technique) with 0.5 M sulfuric acid and dried at 150 ℃.[24] Finally, all the samples were calcined in the air at temperatures between 450 ~ 650 ℃ with a soak time of 3 h.

The TiO_2 nanoparticles were synthesized via modified precipitation of $TiOSO_4 \cdot xH_2SO_4$ (Alfa Aesar) with ammonia solution at 85 ℃. The pH value of the solution was controlled under acidic conditions during precipitation. The resulting suspension was then refluxed overnight. Impurities and by-products, such as excessive SO_4^{2-} and NH_4^+ ions, were removed by filtration and washing with an adequate amount of distilled deionized water until the filtrate pH was neutral. The obtained white powder was then dried overnight at 120 ℃.

3.3.2 Catalyst Characterization

The catalyst was characterized by powder X-ray diffraction (PXRD), field emission scanning electron microscopy (FESEM), high resolution transmission electron microscopy (HRTEM), thermogravimetric analysis (TGA), temperature programmed desorption (TPD), X-ray photoelectron spectroscopy (XPS) and nitrogen adsorption/desorption [Brunauer-Emmett-Teller (BET) surface area]. The acid types of the catalysts were determined by pyridine-adsorption and FT-IR experiments. The amount of acid sites was determined by thermogravimetric titration using 2,6 lutidine and 3,5 lutidine.[25]

3.3.3 Typical Condition for Biomass Conversion Reaction

Carbohydrate conversion experiments were carried out in a 100 mL cylindrical stainless steel pressurized reactor made by PARR Instrument Company, USA. In a typical reaction, 1 mmol of monosaccharide (0.18 g of fructose/glucose), 0.5 mmol of disaccharide (0.18 g of sucrose/ cellobiose) or biomass sources (molecular weight of cellulose and starch are calculated as a glucose unit) were used as substrates. Catalyst (0.01 to 0.20 g) and solvent (20 mL) were charged into the reactor, followed by purging with nitrogen, and pressurizing to 20 bar. The reactor was then heated to designated temperatures for different reaction times with stirring. After the reaction was completed, the reactor was cooled in an ice bath. The reaction mixture was centrifuged and filtered to remove the catalyst and insoluble solids before analyses. For testing of the reusability of the catalyst, the catalyst was collected by centrifugation after reaction, then washed with methanol (20 mL) twice and dried at 100 ℃ before reuse. The catalyst was regenerated by calcining under air at 400 ℃ for 1 h.

3.3.4 The Synthesis and Characterizations Procedures of Standard Chemicals Levulinic Esters and HMF-Derived Ethers

^{1}H and ^{13}C NMR spectra were recorded on a Bruker AVANCE III- 400 MHz spectrometer. ^{1}H NMR spectra were collected at 400 MHz with chemical shift referenced to the residual peak in $CDCl_3$ (δ: H 7.26 ppm). ^{13}C NMR spectra were collected at 100 MHz and referenced to residual peak in $CDCl_3$ (δ: C 77.0 ppm) or CD_3OD (δ: C 49.1 ppm). Multiplicities are given as s (singlet), d (doublet), t (triplet), and m (multiplet).

3.3.4.1 Preparation and Characterization of Levulinic Esters

***n*-Propyl levulinate** To a mixture of levulinic acid (5.8 g, 0.05 mol), and *n*-propanol (7.5 g, 0.125 mol) in toluene (15 mL) was added H_2SO_4 (0.1 mL) dropwise under reflux. The mixture was refluxed for 4 h. After cooling, the reaction mixture was added to dichloromethane and washed with H_2O. The organic layer was dried over $MgSO_4$. After removal of the solvent, the residue was purified by vacuum distillation to yield *n*-propyl levulinate as a colorless liquid. ^{1}H NMR ($CDCl_3$, 400 MHz): δ: 4.04 ~ 4.00 (m, 2H), 2.74 (t, *J* = 6.6 Hz, 2H), 2.57 (t, *J* = 6.6 Hz, 2H), 2.18 (s, 3H), 1.68 ~ 1.59 (m, 2H), 0.93 (t, *J* = 7.4 Hz, 3H). ^{13}C NMR ($CDCl_3$, 100 MHz): δ: 206.6, 172.8, 66.2, 37.9, 29.8, 28.0, 21.9, 10.3. HRMS *m/z* $(M + H)^+$ for $C_8H_{15}O_3$ 159.1021, found 159.0993.

2-Propyl levulinate 2-Propyl levulinate was obtained from 2-propanol as a colorless liquid following the procedure for the preparation of *n*-propyl levulinate. ^{1}H NMR ($CDCl_3$, 400 MHz): δ: 5.01 ~ 4.95 (m, 1H), 2.72 (t, *J* = 6.6 Hz, 2H), 2.53 (t, *J* = 6.6 Hz, 2H), 2.17 (s, 3H), 1.22 (s, 3H), 1.21 (s, 3H). ^{13}C NMR ($CDCl_3$, 100 MHz): δ: 206.7, 172.2, 67.9, 38.0, 29.8, 28.4, 21.7 (2C). HRMS *m/z* $(M + H)^+$ for $C_8H_{15}O_3$ 159.1021, found 159.0995.

2-Butyl levulinate 2-Butyl levulinate was obtained from 2-butanol as a colorless liquid following the procedure for the preparation of *n*-propyl levulinate. ^{1}H NMR ($CDCl_3$, 400 MHz): δ: 4.86 ~ 4.78 (m, 1H), 2.73 (t, *J* = 6.6 Hz, 2H), 2.53 (t, *J* = 6.6 Hz, 2H), 2.18 (s, 3H), 1.62 ~ 1.48 (m, 2H), 1.18 (d, *J* = 6.3 Hz, 3H), 0.88 (t, *J* = 7.4 Hz, 3H). ^{13}C NMR ($CDCl_3$, 100 MHz): δ: 206.7, 172.4, 72.5, 38.0, 29.8, 28.7, 28.3, 19.4, 9.6 HRMS *m/z* $(M + H)^+$ for $C_9H_{17}O_3$ 173.1178, found 173.1162.

***t*-Butyl levulinate** To a mixture of levulinic acid (5.9 g, 0.05 mol), and *t*-butanol (7.6 g, 0.1 mol) in dichloromethane (80 mL) was added 4-dimethylaminopyridine (DMAP) (1.8 g, 0.015 mol)

under r.t. Then, N,N'-dicyclohexylcarbodiimide (DCC) (12.5 g, 0.06 mol) was added at 0 ℃. After stirring at r.t. for 10 h, the urea was filtered and the organic layer was concentrated in vacuum. After removal of the solvent, the residue was purified by vacuum distillation to yield *t*-butyl levulinate as a colorless liquid. ^{1}H NMR ($CDCl_3$, 400 MHz): δ: 2.68 (t, *J* = 6.6 Hz, 2H), 2.48 (t, *J* = 6.6 Hz, 2H), 2.17 (s, 3H), 1.43 (s, 9H). ^{13}C NMR ($CDCl_3$, 100 MHz): δ: 206.9, 172.0, 80.6, 38.1, 29.9, 29.2, 28.0 (3C). HRMS *m/z* $(M + H)^+$ for $C_9H_{17}O_3$ 173.1178, found 173.1188.

3.3.4.2 Preparation and Characterization of Hydroxymethylfurfural Ethers

5-(Isopropoxymethyl)furan-2-carbaldehyde A mixture of hydroxymethylfurfural (0.3 g, 2.38 mmol) and TiO_2 nanoparticles (100 mg) in 2-propanol (6 mL) was heated to 100 ℃ for 6 h. After cooling, the reaction mixture was added to dichloromethane and washed with H_2O. The organic layer was dried over $MgSO_4$. After removal of the solvent, the residue was purified by column chromatography (dichloromethane/hexane=1/1) to yield 5-(isopropoxymethyl)furan-2-carbaldehyde as a light yellow liquid. ^{1}H NMR ($CDCl_3$, 400 MHz): δ: 9.59 (s, 1H), 7.19 (d, *J* = 3.5 Hz, 2H), 6.50 (d, *J* = 3.5 Hz, 2H), 4.52 (s, 2H), 3.74 ~ 3.64 (m, 1H), 1.20 (s, 3H), 1.19 (s, 3H). ^{13}C NMR ($CDCl_3$, 100 MHz): δ: 177.6, 159.4, 152.4, 122.1, 110.7, 72.1, 62.5, 21.9 (2C). HRMS *m/z* $(M + H)^+$ for $C_9H_{13}O_3$ 169.0865, found 169.0852.

5-(*sec*-Butoxymethyl)furan-2-carbaldehyde 5-(*sec*-Butoxymethyl)furan-2-carbaldehyde was obtained from 2-butanol as a mixture of diastereomers (6:1) a light yellow liquid following the procedure for the preparation of 5-(isopropoxymethyl)furan-2-carbaldehyde. ^{1}H NMR ($CDCl_3$, 400 MHz): δ: δ: 9.60 (s, 1H), 7.20 ~ 7.19 (m, 2H), 6.50 (d, *J* = 3.5 Hz, 2H), 4.59 ~ 4.48 (m, 2H), 3.51 ~ 3.43 (m, 1H), 1.64 ~ 1.52 (m, 2H), 1.17 ~ 1.16 (m, 3H), 0.92 ~ 0.88 (m, 3H). ^{13}C NMR

(CD_3OD, 100 MHz): δ: 179.5, 161.0, 154.0, 124.5, 112.3, 78.5, 63.6, 30.3, 19.5, 10.1. HRMS *m/z* $(M + H)^+$ for $C_{10}H_{15}O_3$ 183.1021, found 183.1002.

The ^1H and ^{13}C NMR of 5-(*sec*-butoxymethyl)furan-2-carbaldehyde contained signals that we ascribed to the diastereomer, which accounted for approximately 15% of product material. Selected ^1H signals of the minor isomer: 9.63 (s, 0.15H), 6.62 (d, J=8.7 Hz, 0.15H), 5.60 (t, J=5.8 Hz, 0.15H), 5.29 (s, 0.15 H), 3.76 ~ 3.70 (m, 0.15H). Selected ^{13}C signals of the minor isomer: 63.48, 19.48, 10.03.

5-(*tert*-Butoxymethyl)furan-2-carbaldehyde 5-(*tert*-Butoxymethyl)furan-2-carbaldehyde was obtained from *t*-butanol as a light yellow liquid following the procedure for the preparation of 5-(isopropoxymethyl)furan-2-carbaldehyde. ^1H NMR ($CDCl_3$, 400 MHz): δ: 9.54 (s, 1H), 7.16 (d, *J* = 3.5 Hz, 2H), 6.45 (d, *J* = 3.5 Hz, 2H), 4.43 (s, 2H), 1.22 (s, 9H). ^{13}C NMR ($CDCl_3$, 100 MHz): δ: 177.4, 160.1, 152.2, 122.3, 110.2, 74.3, 57.1, 27.3 (3C). HRMS *m/z* $(M + H)^+$ for $C_{10}H_{15}O_3$ 183.1021, found 183.1035.

3.3.5 Other Characterizations

The catalysts were characterized using several techniques: Powder X-ray diffraction (PXRD) patterns were obtained using a Rigaku UltimaIV X-ray diffractometer with Cu Kα radiation and a beam voltage of 40 kV and 44 mA beam current. Field emission scanning electron microscopy (FESEM) micrographs were taken on a Zeiss DSM 982 Gemini emission scanning microscope with a Schottky Emitter at an accelerating voltage of 2 kV with a beam current of 1 μA. Samples were ultrasonically dispersed in methanol and deposited onto a silicon wafer. High resolution transmission electron microscopy (HRTEM) studies were carried out using a JEOL 2010

transmission electron microscope with an accelerating voltage of 200 kV. The samples were prepared by dispersing the material in methanol. A drop of the dispersion was placed on a carbon coated copper grid and allowed to dry. Thermogravimetric analyses (TGA) were performed on a Hi-Res TA 2950 thermogravimetric analyzer with 60 mL/min of air flow from 25 to 1000 ℃ at a heating rate of 10 ℃/min. Temperature programmed desorption (TPD) was carried out in a furnace with a quadrupole MS residual gas analyzer. Catalyst powder (200 mg) was placed in a quartz tube and then pre-treated in helium flow (100 mL/min) at 180 ℃ for 1 h to dry the catalyst. After the pre-treatment, 10 % NH_3 in Ar (100 mL/min) was fed at room temperature for 1 h, followed by feeding pure helium flow (100 mL/min) for another 2 h to remove the physically adsorbed NH_3. The acid sites of the catalyst were analyzed by following the m/z = 17 signal over a temperature range from room temperature to 800 ℃ in pure helium flow (100 mL/min). The m/z = 64 signal was also followed to check the decomposition of sulfate ion to SO_2 gas. FT-IR spectra were recorded using a Thermo Scientific Nicolet 8700 spectrometer. The samples were pressed into pellets and self-supporting wafers in a holder in an *in situ* cell and dried at 200 ℃ for 12 hours before analysis. To obtain the spectra of pyridine adsorbed on the surface, the samples were exposed to pyridine vapor for 1 hour at room temperature. Spectra were then recorded after evacuation (10^{-2} Torr) for 30 min at 200 ℃. The Brunauer-Emmett-Teller (BET) surface area of TiO_2 was measured using a Quantachrome Autosorb-1-C automated N_2 gas adsorption system. Samples (150 mg) were pre-degassed at 150 ℃ for about 12 hours to remove water and other physically adsorbed species. The N_2 isothermal adsorption and desorption experiments were performed at relative pressures (P/P_0) from 10^{-3} to 0.992 and from 0.992 to 0.01, respectively. The thermogravimetric titration analysis was done using 2,6- and 3,5- lutidine as probing bases. The

acid amount of the solid acids was calculated by subtracting the weight loss for desorption of base from the materials.

The undiluted reaction mixture was characterized using a gas chromatograph (HP 5890 series II) equipped with a DB-17MS capillary column (20.0 m x 180 μm x 0.18 μm) and mass selective detector (5971 series). The reaction mixture was also analyzed with a Shimadzu series HPLC (Biorad Aminex HPX-87H column) with an RI detector using 0.005 M H_2SO_4 (rate = 0.6 mL/min) as eluents. An HP 5890 series II GC system equipped with a MTX® -biodiesel TG w/Integra-GapTM capillary column (14.0 m x 530 μm x 0.16 μm) and an FID detector was used for quantitative analysis. The yields of organic products were obtained from GC analyses based on a calibration curve from commercial or synthesized samples and an internal standard (1-octanol). The yields were calculated on a carbon-basis. Carbohydrate conversions were determined from HPLC data. The conversion was calculated from the fructose, glucose, sucrose, and cellobiose on a carbon-basis. The polysaccharide conversions of cellulose and starch were further calculated by subtracting the weight of remaining solids (unreacted biomass) at the end of the reaction. The data were obtained using the following equations:

Monosaccharides conversion (%) = 100(A-C)／A

Polysaccharides conversion (%) = 100(B-C-D)／B

Organic products yield (%) = 100E／A or B

A: total amount (mol) of monosaccharides used.

B: total amount (mol) of glucose monomer in cellulose.

C: total amount (mol) of remaining monosaccharides.

D: the unreacted biomass after reaction.

E: total amount (mol) of organic products produced by catalytic reaction.

3.4 Results and Discussion

3.4.1 Discussion of Catalyst Characterization

PXRD, FESEM, HRTEM and N_2 sorption analyses. As-Synthesized TiO_2 nanoparticles were indicated as the anatase phase in PXRD analysis. The broadening of diffraction lines indicates small crystallite sizes. Crystallite sizes were calculated to be an average of ~ 4 nm using Scherrer's equation. The anatase phase was maintained up to 800 ℃ and fully converted to the rutile phase by 1000 ℃. The FESEM images show mostly micron size aggregated powder and with no distinct particle morphology. The HRTEM images confirmed the nano-size nature of synthesized TiO_2 particles. The HRTEM image shows that the powder sample consists of aggregated nanoparticles and estimated particles size were consistent with XRD data (~ 4 nm) (**Figure 3.1**). The BET surface area of the TiO_2 was calculated to be 238 m^2 g^{-1} from N_2 sorption data, which is high compared to other tested catalysts.

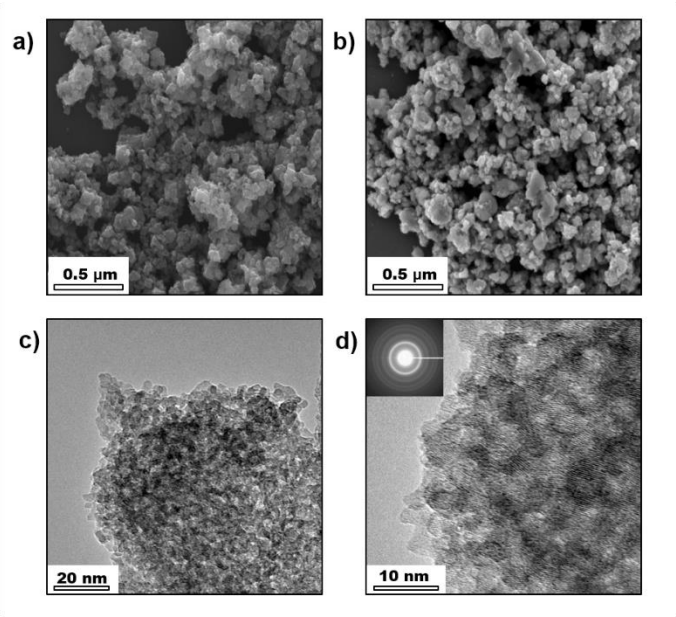

Figure 3.1 The SEM and TEM images of TiO_2 nanoparticles (a) SEM image of freshly prepared TiO_2; (b) SEM image of after the 6^{th} reaction; (c,d) TEM images of freshly prepared TiO_2. Inset: SAED of freshly prepared TiO_2 nanoparticles.

Pyridine-adsorption and FT-IR experiments. The type of acid sites on TiO_2 nanoparticles was determined by pyridine adsorption and FT-IR spectroscopy (**Figure 3.2**). The FT-IR spectrum of TiO_2 nanoparticles without pyridine adsorption treatment showed the typical surface SO_4^{2-} stretch modes in the 1000-1500 cm^{-1} region. The vibrations at 1045 cm^{-1}, 1132 cm^{-1} and 1221 cm^{-1} are attributed to surface SO_3^- stretches. The band at 1400 cm^{-1} is ascribed to O=S=O stretching of SO_4^{2-} groups, which could be chelating in bidentate or bridged bidentate forms on the surface of the TiO_2 nanoparticles.[1] In the pyridine-adsorption FT-IR spectrum, three peaks were observed in the region between 1400 ~ 1600 cm^{-1} due to C–C stretching vibrations of pyridine. The peak at 1445 cm^{-1} was assigned to pyridine adsorbed on Lewis acid sites; the peak at 1548 cm^{-1} is characteristic of pyridine adsorbed on Brønsted acid sites and the peak at 1490 cm^{-1} appears for pyridine adsorbed on both Brønsted and Lewis acid sites.

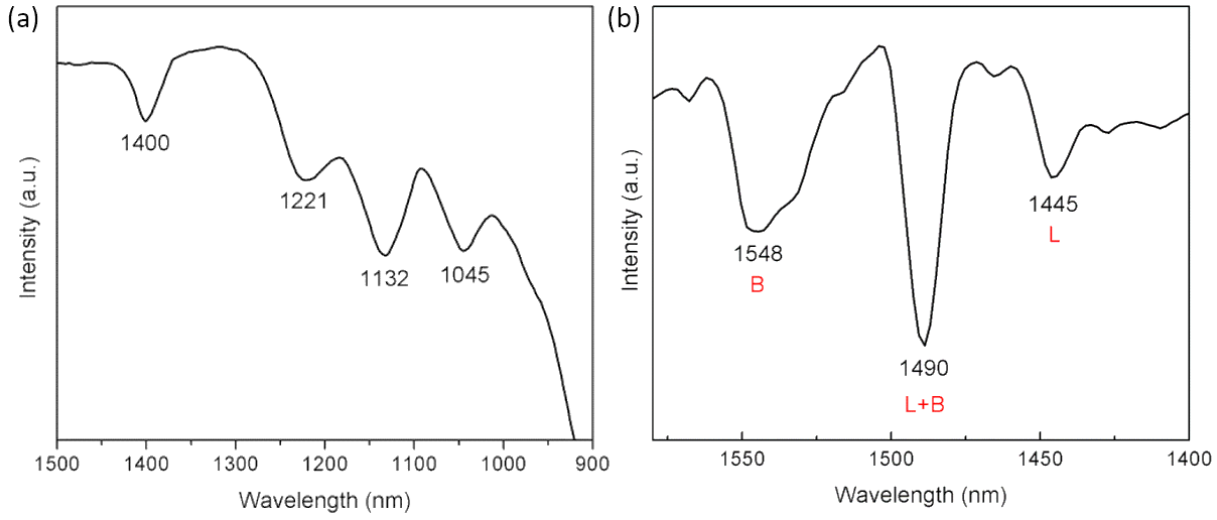

Figure 3.2 (a) The IR spectrum of freshly prepared TiO_2 nanoparticles. (b) The pyridine adsorption IR spectrum of TiO_2 nanoparticles.

NH_3-TPD and TGA analyses. NH_3-TPD experiments were conducted to determine the relative strengths of acid sites (**Figure 3.3**). A major desorption occurred between 150 to 500 ℃,

and another minor desorption peak between 550 to 700 ℃. The desorption peak centered at ~ 325 ℃ is attributed to NH_3 adsorbed on weak acid sites while the one centered at ~ 600 ℃ is due to NH_3 adsorbed on strong acid sites.[2] The amount of SO_4^{2-} ions attached to the surface of the TiO_2 nanoparticles was determined by TGA experiments. A 3 % mass decrease was observed between 450 and 700 ℃, which resulted from decomposition of SO_4^{2-} ions from the TiO_2 surface. This is also shown by the TPD experiments where SO_2 (decomposition of SO_4^{2-} ions, m/z = 64) was detected starting at 450 ℃. These data suggest that the weight loss peak around 600 ℃ can properly be ascribed to SO_4^{2-} ion decomposition.

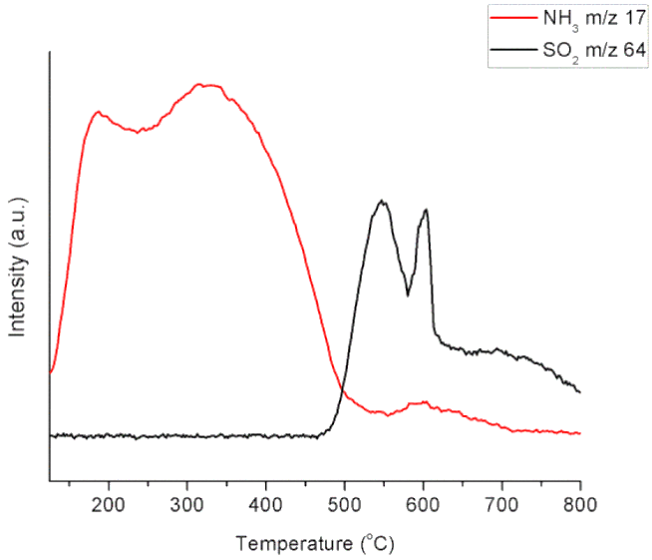

Figure 3.3 The NH_3-TPD desorption analysis of freshly prepared TiO_2 nanoparticles.

3.4.2 Catalytic Conversion of Fructose to Methyl Levulinate

The catalytic performance of the TiO_2 nanoparticles was first tested by fructose conversion in MeOH (**Figure 3.4**). The reaction started with dehydration of fructose to HMF followed by rehydration of HMF to levulinic acid. Finally, levulinic acid was further converted to methyl levulinate (ML) by esterification with MeOH. In primary temperature-dependent studies using fructose as a substrate, TiO_2 nanoparticles exhibited moderate activity (93 % conversion and 4 %

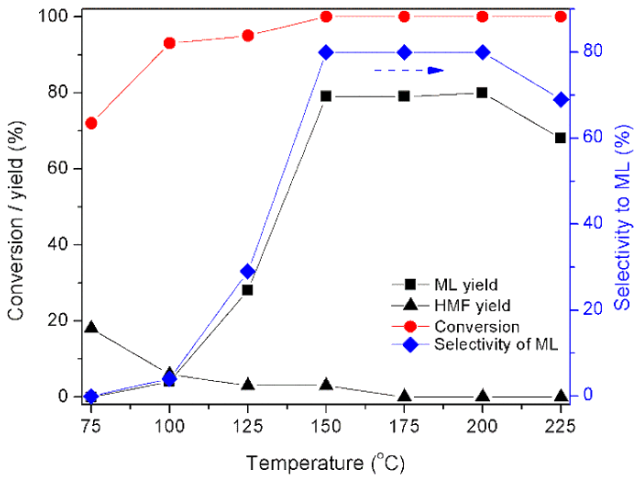

Figure 3.4 Influence of the reaction temperature on fructose conversion and ML yield. (*Reaction conditions:* 20 mL 0.05 M fructose in MeOH, 0.1 g TiO_2 nanoparticles, 1 h.)

ML yield) when the reaction temperature was below 100 ℃; however, when the temperature was increased to 150 ℃, the yield of ML was enhanced to 79 %. It was not until 225 ℃ that the yield of ML dropped to 68 %. This drop is probably due to decomposition of ML at higher temperatures. In addition, HMF and levulinic acid were barely detected in any experiment throughout this study, indicating rapid rehydration of HMF and esterification to produce ML. Typically, the formation of humins either from sugar decomposition or HMF oxidation is believed to be the main factor that lowers the ML yield.[26] Therefore, the origin of humins was further investigated by FT-IR analyses (**Figure 3.5**). For these analyses, formed humins were collected from two separate reactions utilizing fructose and HMF as substrates, respectively. Both FT-IR spectra showed similar features, such as several broad absorbance peaks located in 900 ~ 1800 cm^{-1} region as well as two distinct peaks located at 1596 and 1716 cm^{-1}. The latter two can be assigned to humins formed from aldol addition/condensation polymerization of 2,5-dioxo-6-hydroxyhexanal (DHH), which is a highly active intermediate formed from HMF. In addition, humins collected from the HMF reaction exhibited two additional peaks at 758 and 795 cm^{-1}, which can be attributed

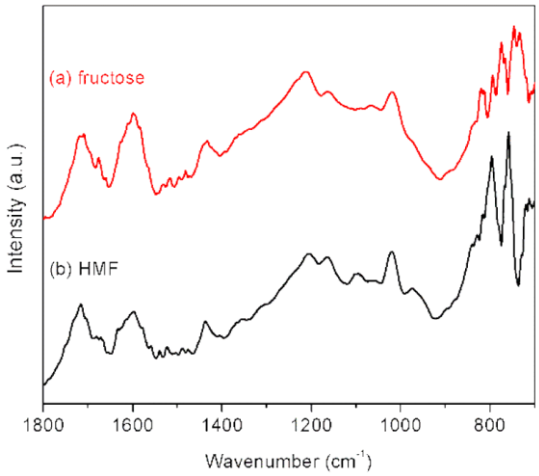

Figure 3.5 IR spectra of (a) humins formed using HMF as substrate, and (b) humins formed using fructose as substrate.

to polymerized HMF.[26b] Thus, fructose and HMF polymerization are not the main sources for the formation of humins. Instead, the intermediate HMF is most likely rapidly converted to ML contributing to the higher yields of ML at short reaction times.

To investigate the effects of catalyst loading on activity, different amounts of catalyst were used. The studies showed that TiO_2 nanoparticles exhibit high activity even with lower catalyst loading. For example, only 5.5 wt% catalyst loading (with respect to fructose) was required for a 67 % yield of ML with 95 % conversion. The product mixture in methanol solution was analyzed by NMR without further purification and was identified as ML with minimal impurities. In contrast to homogeneous acid catalyzed reactions, the purification process in this system only requires filtration and solvent removal, which affords a straightforward and economical approach.

3.4.3 Comparison of Different Catalysts for the Conversion of Fructose to ML

The catalytic performances of TiO_2 nanoparticles were compared to other TiO_2 materials and solid acid catalysts such as Amberlyst-15, sulfated ZrO_2 and TiO_2, niobic acid, and H-type zeolites.

Table 3.1 Summary of catalytic results and characterization for different solid acid catalysts[a]

Catalyst	Conversion (%)[b]	Yield / Selectivity (%) HMF[b]	ML[c]	MLA[c]	BET (m^2/g)	Acid sites by 2,6 Py μmol/g[e]	Acid sites by 3,5 Py μmol/g[e]
TiO_2 nanoparticles	>99	0/(0)	79/(80)	-[d]	238	303	218
Commercial TiO_2	23	3/(13)	0/(0)	-	18[g]	19	20
P-25 TiO_2	87	20/(23)	0/(0)	-	56[g]	48	42
Sulfated ZrO_2	89	25/(28)	62/(70)	-	106	207	154
Sulfated TiO_2	82	33/(40)	41/(50)	-	98	144	127
Amberlyst-15	>99	0/(0)	66/(60)	-	35	457[f]	457[f]
Nb_2O_5	76	5/(7)	0/(0)	-	20	5	125
H-ZSM5 (Si/Al =50)	98	0/(0)	26/(27)	21/(21)	426[g]	272	674
H-Beta (Si/Al =30)	72	0/(0)	11/(15)	23/(32)	680[g]	607	628

[a] *Reaction conditions*: MeOH (20 mL), fructose (1 mmol), catalyst (0.1 g), 175 °C, 1 h under N_2. The average yields are reported. [b] Conversions and yields of HMF were obtained by HPLC analysis. [c] Yields and selectivities of methyl levulinate (ML) and methyl lactate (MLA) were obtained by GC-FID analysis. [d] Not observed product. [e] The number of acid amount measurements were done by thermogravimetric titration method. [f] Due to the thermal instability of Amberlyst-15, the acidity data was acquired from literature.[31] [g] acquired from literature. [31]

Due to the fact that dehydration of fructose is associated with the acidity of the catalyst,[27] the acidities of the solid catalysts were characterized by thermogravimetric titration using 2,6 and 3,5 lutidines.[26b] The catalytic results, surface areas, and acidities are summarized in **Table 3.1**. For the acid-catalyzed dehydration of fructose, commercial TiO_2 was inactive under the same conditions. P-25 did not show any rehydration ability; only HMF (20 %) was detected after reaction. Among the other tested solid acids, Amberlyst-15 showed the highest activity and niobic acid only produced a small amount of HMF (5 %). Sulfated ZrO_2 and TiO_2 showed the formation of the desired product ML in moderate yields (62 % and 41 %, respectively). The catalytic results are strongly correlated with surface acidity. Among the studied materials, TiO_2 nanoparticles exhibited

the most acidic sites as well as the largest surface areas. This might be the reason why TiO_2 nanoparticles were highly active for fructose conversion. Moreover, the notable high activity of prepared acidic TiO_2 nanoparticles is attributed to its nano-sized nature. Ultra-sonicated TiO_2 in MeOH is able to remain in suspension for more than one week. Such behaviour minimizes mass transfer limitations under reaction conditions.

Classic acid-rich H-type zeolites like HZSM-5 and H-beta were also tested under the same reaction conditions. Thermogravimetric titration results showed that the acidities of HZSM-5 and H-beta catalysts were higher than that of TiO_2 nanoparticles. However, HZSM-5 and H-beta exhibited lower selectivities for fructose conversion than the TiO_2 nanoparticles. Both zeolites converted fructose not only to ML and methyl lactate but also unidentified side products. This might be due to the mixture of acid types in zeolites. The H-type zeolites contain both Brønsted and Lewis acid sites on the surface.[28] As shown in Scheme 1, Brønsted acids allow reactions to undergo dehydration then rehydration to produce ML; Lewis acids, on the other hand, catalyze a retro-aldol reaction to generate methyl lactate. Also, the relatively stronger acidities of H-type zeolites were not suitable for fructose conversion under optimized conditions for TiO_2 nanoparticles. Consequently, the selectivity toward ML was significantly lowered to 27~15 % for H-type zeolites. The TiO_2 nanoparticle catalyst provide appropriate acidity to catalyze both the dehydration and further rehydration of fructose.

3.4.4 Investigations on Conversion of Different Biomass Sources

Investigation of the conversion of different biomass sources demonstrated the practical applicability of the synthesized TiO_2 catalyst (**Table 3.2**). In glucose conversion, the reaction pathway involves isomerization of glucose to fructose. Fructose is then converted to ML in MeOH.

Table 3.2 Methyl levulinate yields from different biomass carbohydrates catalyzed by TiO_2 nanoparticles[a]

Substrate	Yield / Selectivity (%)	
	Conversion (%)[b]	ML[c]
Fructose	>99	80/(80)
Glucose	>99	61/(61)[e]
Sucrose	82, >99	51/(62), 65/(65)[d]
Cellobiose	68, >99	17/(25), 58/(58)[e]
Cellulose	72	42/(58)[f]
Starch	67	40/(60)[f]

[a] *Reaction conditions*: MeOH (20 mL), fructose (1 mmol), catalyst (0.1 g), 175 ℃, 1 h under N_2. All reactions were repeated three times. The average yields are reported. [b] Conversions were obtained by HPLC analysis. [c] Yields and selectivities of ML were obtained by GC-FID analysis. [d] Reaction time: 3 hours. [e] Reaction time: 9 hours. [f] Reaction time: 20 hours .

The time-dependent studies (**Figure 3.6**) showed the co-existence of glucose and fructose in the first 5 hours, indicating a slow glucose isomerization. The yield of ML stabilized at a maximum of 61% after 9 hours. The rate of glucose isomerization controls the selectivity to ML. The use of disaccharides such as sucrose (a disaccharide of glucose and fructose) and cellobiose (a disaccharide of glucose) requires initial hydrolysis of disaccharide into the monosaccharides. Sucrose and cellobiose were also selectively converted to ML with high yields (65 % and 58 %, respectively), indicating that sequential reactions (hydrolysis of disaccharides, isomerization of glucose to fructose and finally conversion to ML) were successfully catalyzed. The main differences between the conversions of sucrose and cellobiose are the reaction times; sucrose only requires 3 hours while cellobiose requires 9 hours to complete the reaction. This difference may be due to the hydrolysis of sucrose to glucose and fructose units, which is feasible for conversion of ML. Besides these monosaccharides (fructose, glucose) and disaccharides (sucrose, cellobiose), polysaccharides (cellulose and starch) were also tested under the same conditions as fructose

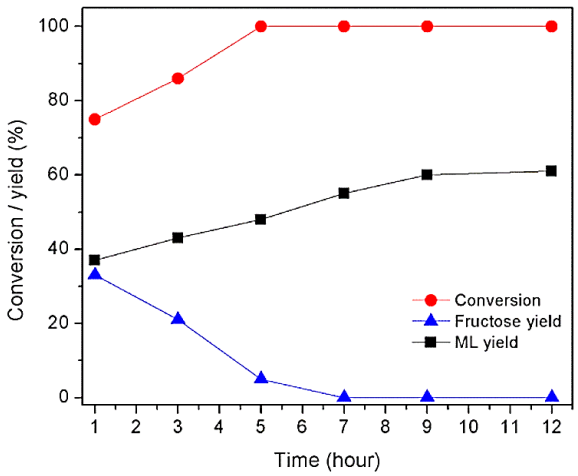

Figure 3.6 Effect of time on conversion of glucose to fructose and ML. (*Reaction conditions*: 0.18 g glucose in 20 mL MeOH, 0.1 g catalyst, 175 ^{o}C.)

conversion. Both cellulose and starch reached ML yields around 40% after 20 hours. Conversion of cellulose to ML involves depolymerization of cellulose to glucose and the subsequent transformation of glucose to ML; therefore, a longer reaction time was needed for this reaction. The depolymerization of cellulose/starch to glucose may be hindered in organic solvents by solubility constraints.

3.4.5 Investigations on Conversion in Different Solvents

Utilization of TiO_2 nanoparticles for converting fructose in various solvents was investigated, and the results are given in **Table 3.3**. Fructose was dehydrated to HMF, but no further rehydrated products such as levulinic acid were detected in aprotic solvents. Among all tested aprotic solvents, tetrahydrofuran (THF) gave the highest HMF yield (54 %). Although fructose solubility is higher in solvents with relatively high boiling points [such as dimethyl sulfoxide (DMSO), dimethylformamide (DMF), and dimethylacetamide (DMA)] the use of these solvents produced more humins during the reaction (as indicated by a deep brown color observed after the reaction). The formation of humins suppressed the HMF yield in these solvents.

Table 3.3 Effect of solvents on fructose conversions and products yields catalyzed by TiO_2 nanoparticles[a]

Solvent	Time (h)	Conversion (%)[b]	Yield (%)			
			HMF[b]	HMF ether[c]	Levulinic ester[c]	LA[b]
THF	1	>99	42	-[d]	-	-
	3	>99	54	-	-	-
CH_3CN	3	66	19	-	-	-
DMF	3	>99	31	-	-	-
DMSO	3	>99	30	-	-	-
DMA	3	>99	35	-	-	-
EtOH	1	97	n.d.	18	58	n.d.
	3	>99	n.d.	n.d.	71	n.d.
n-PrOH	1	98	n.d.	14	66	n.d.
	3	>99	n.d.	n.d.	78	n.d.
2-PrOH	1	96	< 1%	52	8	2
	3	>99	< 1%	68	13	4
n-BuOH	1	>99	n.d.	12	67	n.d.
	3	>99	n.d.	n.d.	75	n.d.
2-BuOH	1	96	< 1%	54	4	2
	3	>99	< 1%	67	10	6
t-BuOH	1	98	9	45	3	8
	3	>99	7	63	7	9

[a] *Reaction conditions:* solvent (20 mL), fructose (1 mmol), catalyst (0.1 g), 150 °C, under N_2. [b] Conversion and yield of HMF and levulinic acid were obtained by HPLC analysis. [C] Yields of levulinic esters and HMF-derived ethers were obtained by GC-FID analysis. [d] Not observed product.

Regarding the utilization of levulinic esters as diesel blend components, lower molecular weight levulinic esters have shown some disadvantages. ML is miscible with water, which is difficult to manage. Another disadvantage is that ML might separate from biodiesel at low temperatures. However, higher molecular weight levulinic esters have higher octane numbers, which are thermally more stable. Mixing diesel with higher boiling point levulinic esters can also reduce volatile organic compound (VOC) emissions, and is more environmentally friendly.[29] Therefore, *n*-ethanol, propanol, and butanol were used as solvents in order to produce levulinic esters with higher molecular weights. The results showed that fructose converted to different *n*-alkyl levulinates can reach 71~ 78% yield in three hours. Zhang et al. tried to produce alkyl levulinates in high yields.[29b] However, the expensive furfuryl alcohol was needed as a precursor while our process uses economical raw precursors such as fructose to produce versatile levulinic esters using a TiO_2 nanoparticle catalyst.

The formation of levulinic esters from fructose is a consecutive reaction which probably proceeds by either rehydration of HMF-ether to form levulinic ester or by rehydration of HMF to levulinic acid, followed by esterification to form levulinic ester. Interestingly, the use of higher steric hindrance alcohols such as 2-propanol, 2-butanol and *t*-butanol led to the HMF-derived ethers as main products as opposed to levulinic esters. The reaction was not favorable for further rehydration to form levulinic esters, so the generation of other products such as levulinic acid or esters was suppressed. The yields of HMF-derived ethers were 63 ~ 68% in 2-propanol, 2-butanol and *t*-butanol. HMF-derived ethers such as 5-ethoxymethylfurfural have already been tested, and exhibited comparable energy density relative to standard gasoline.[30] The advantage of forming HMF-derived ethers is that they are much more stable and easier to work with than HMF.

Therefore, by adjusting *n*-alkyl alcohols to higher sterically hindered alcohols, another selection of valuable platform chemicals (HMF-derived ethers) was obtained.

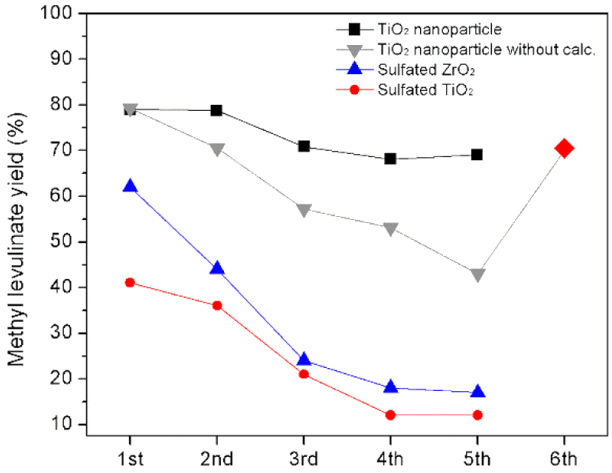

Figure 3.7 Reusability of TiO_2 nanoparticles and sulfated metal oxides. The catalysts were calcined at 400 ºC for 1 h before reuse except the one for TiO_2 nanoparticles without calcination (▼) and calcined at the 6th use (◆). (*Reaction conditions:* 20 mL 0.05 M fructose in MeOH, 0.1 g catalyst, 175 ℃, 1 h.)

3.4.6 Investigations of the Catalysts Reusability

Reusability is also a key factor in heterogeneous catalysis. Results indicate that the yields of ML gradually decreased to 40 % after the 5th use (**Figure 3.7**). The color of the catalyst changed from white to deep brown, indicating an accumulation of humins on the surface of catalyst over time, possibly causing deactivation. Therefore, post treatment of the catalyst was performed by calcination at 400 ℃ for 1 h. The white color of the catalyst was restored, and the yields reverted to 70 % with only around a 10 % loss of yield after the 6th use. The recovered catalysts were further characterized. The XRD patterns and SEM images of recovered TiO_2 nanoparticles showed no significant changes after calcination. These characterization studies showed that the morphology of TiO_2 nanoparticles remained the same after reaction and regeneration.

Sulfated metal oxides are well known strong solid acid catalysts and are widely tested for catalytic reactions.[31] The main drawback of sulfated metal oxides is the unstable activity due to sulfate leaching problems. Therefore, we compared the stability of TiO_2 nanoparticles to other sulfated ZrO_2 and TiO_2 prepared by impregnation methods. To reduce interferences, humins adsorbed on the catalysts were removed by calcination after each use. The results are shown in (**Figure 3.7**). The yield of ML from 80 % dropped to 70 % after the 3rd use but stabilized at around 70 % in further uses for TiO_2 nanoparticles. On the other hand, the activity of sulfated ZrO_2 and TiO_2 catalysts drastically dropped; both of the sulfated catalysts were almost completely deactivated after the 5th use. Strong acidity for the sulfated catalysts is primarily due to the chelation of sulfate ions on the surface of metal oxides.[31] Therefore, the thermal stability of TiO_2 nanoparticles was also tested. The results indicated the sulfur concentration of the TiO_2 nanoparticles for different treatments. Almost no sulfur was detected for the catalyst calcined at 800 ℃ which showed no activity toward ML production. The deactivation might occur due to sulfate ion decomposition. Deactivation of the sulfated metal oxide catalysts due to sulfate ion leaching or the thermal instability of the catalysts has been discussed in several other studies.[31] The post-treatment of catalysts to remove humins might also be responsible for sulfate ion removal on the metal oxide surface due to thermal decomposition. Ultimately, synthesized acidic TiO_2 nanoparticles showed superior behaviour in preserving activity and thermal stability.

3.5 Conclusions

In summary, we report a one-step synthesis of acidic TiO_2 (anatase) nanoparticles that can produce high yields of ML in MeOH from different biomass derived carbohydrates under moderate conditions. The ML yields obtained from fructose were as high as 80 % with 80 % selectivity.

Moreover, HMF, HMF-derived ethers and higher molecular weight levulinic esters can also be obtained by changing solvent feeds. Remarkable catalytic activity of the nanoparticles is attributed to *in-situ* sulfation on the surface and their superior dispersion in reaction media. These novel catalytic nanoparticles allow for the conversion of biomass derived carbohydrates efficiently at low temperatures ranging from 150 to 200 ℃. The catalysts also show high recyclability with a minor loss of performance. These newly discovered acidic TiO_2 nanoparticles for biomass conversion open up a new avenue of cost effective biomass refinery processes toward the production of affordable bio-chemicals and biofuels.

3.6 References

1. C. H. Zhou, X. Xia, C. X. Lin, D. S. Tong and J. Beltramini *Chem. Soc. Rev.* **2011**, *40*, 5588-5617.
2. D. M. Alonso, J. Q. Bond and J. A. Dumesic *Green Chem.* **2010**, *12*, 1493.
3. P. N. R. Vennestrom, C. M. Osmundsen, C. H. Christensen and E. Taarning *Angew. Chem. Int. Ed. Engl.* **2011**, *50*, 10502-10509.
4. D. J. Hayes *Catalysis Today* **2009**, *145*, 138-151.
5. A. J. Ragauskas, C. K. Williams, B. H. Davison, G. Britovsek, J. Cairney, C. A. Eckert, W. J. Frederick, Jr., J. P. Hallett, D. J. Leak, C. L. Liotta, J. R. Mielenz, R. Murphy, R. Templer and T. Tschaplinski *Science* **2006**, *311*, 484-489.
6. R. Rinaldi and F. Schuth *ChemSusChem* **2009**, *2*, 1096-1107.
7. R. Kumar, S. Singh and O. V. Singh *J. Ind. Microbiol. Biotechnol.* **2008**, *35*, 377-391.
8. R. J. van Putten, J. C. van der Waal, E. de Jong, C. B. Rasrendra, H. J. Heeres and J. G. de Vries *Chem. Rev.* **2013**, *113*, 1499-1597.
9. C. Baatz and U. Pruse *J. Catal.* **2007**, *249*, 34-40.
10. T. Werpy and G. Petersen *Top Value Added Chemicals from Biomass: Volume 1 - Results of Screening for PotentialCandidates from Sugars and Synthesis Gas*, National Renewable Energy Laboratory, Golden, CO, **2004**.
11. M. Kitano and F. Tanimoto *Chem. Econ. Eng. Rev.* **1975**, *7*, 25.

12. B. V. Timokhin, V. A. Baransky and G. D. Eliseeva *Russ. Chem. Rev.* **1999**, *68*, 73.
13. S. W. Fitzpatrick, U.S. Pat. 5608105, **1997**.
14. K. Seri, T. Sakaki, M. Shibata, Y. Inoue and H. Ishida *Bioresour. Technol.* **2002**, *81*, 257.
15. L.-P. Peng, L. Lin, J. Zhang, J. Zhuang, B. Zhang and Y. Gong *Molecules*, **2010**, *15*, 5258.
16. J. Hegner, K. C. Pereira, B. DeBoef and B. L. Lucht *Tetrahedron Lett.* **2010**, *51*, 2356.
17. a) X. Y. Wu, J. Fu, X. Y. Lu *Carbohydr. Res.* **2012**, 358, 37-39; b) R. Le Van Mao, Q. Zhao, G. Dima, D. Petraccone *Catal. Lett.* **2011**, *141*, 271-276; c) F. Rataboul, N. Essayem *Ind. Eng. Chem. Res.* **2011**, *50*, 799-805; d) K.-I. Tominaga, A. Mori, Y. Fukushima, S. Shimada, K. Sato *Green Chem.* **2011**, *13*, 810-812; e) Y. Hishikawa, M. Yamaguchi, S. Kubo, T. Yamada *J. Wood Sci.* **2013**, *59*, 179-182.
18. a) S. Saravanamurugan, A. Riisager *Catal. Commun.* **2012**, *17*, 71-75; b) L. C. Peng, L. Lin, H. Li, Q. L. Yang *Appl. Energy,* **2011**, *88*, 4590-4596; c) S. Saravanamurugan, O. N. Van Buu, A. Riisager *ChemSusChem,* **2011**, *4*, 723-726; d) Y. N. Li, J. Q. Wang, L. N. He, Z. Z. Yang, A. H. Liu, B. Yu, C. R. Luan *Green Chem.* **2012**, *14*, 2752-2758.
19. a) G. M. G. Maldonado, R. S. Assary, J. A. Dumesic, L. A. Curtiss *Energy Environ. Sci.* **2012**, *5*, 8990-8997; b) Z. H. Zhang, K. Dong, Z. B. Zhao *ChemSusChem* **2011**, *4*, 112-118; c) J.-P. Lange, W. D. van de Graaf, R. J. Haan *ChemSusChem* **2009**, *2*, 437-441; d) M. Mascal, E. B. Nikitin *ChemSusChem* **2009**, *2*, 859-861.
20. A. Takagaki, M. Ohara, S. Nishimura and K. Ebitani *Chem. Commun.* **2009**, 6276-6278.
21. a) M. S. Holm, S. Saravanamurugan and E. Taarning *Science* **2010**, *328*, 602-605; b) J. Jow, G. L. Rorrer, M. C. Hawley and D. T. A. Lamport *Biomass* **1987**, *14*, 185; c) K. Lourvanij and G. L. Rorrer *Appl. Catal. A* **1994**, *109*, 147.
22. J. L. a. L. Wang *Adv. Mater. Res.* **2010**, *96*, 183.
23. a) Z. Sun, M. Cheng, H. Li, T. Shi, M. Yuan, X. Wang and Z. Jiang *RSC Advances* **2012**, *2*, 9058; b) R. Palkovits, K. Tajvidi, A. M. Ruppert and J. Procelewska *Chem. Commun.* **2011**, *47*, 576-578.
24. A. Corma, A. Martínez and C. Martínez *Appl. Catal. A* **1996**, *144*, 249-268.
25. S. L. Soled, G. B. McVicker, L. L. Murrell, L. G. Sherman, N. C. Dispenziere, S. L. Hsu, D. Waldman *J. of Catal.* **1988**, *111*, 286-295.
26. a) X. Hu and C.-Z. Li *Green Chem.* **2011**, *13*, 1676; b) S. K. R. Patil, J. Heltzel, C. R. F. Lund *Energy Fuels* **2012**, *26*, 5281-5293.

27. M. Watanabe, Y. Aizawa, T. Iida, R. Nishimura, H. Inomata *Appl. Catal. A* **2005**, *295*, 150-156.

28. a) G. L. Woolery, G. H. Kuehl, H. C. Timken, A. W. Chester and J. C. Vartuli *Zeolites* **1997**, *19*, 288; b) Y. Meng, H. C. Genuino, C.-H. Kuo, H. Huang, S.-Y. Chen, L. Zhang, A. Rossi, S. L. Suib *J. Am. Chem. Soc.* **2013**, *135*, 8594-8605.

29. a) L. Lomba, B. Giner, I. Bandrés, C. Lafuente and M. R. Pino *Green Chem.* **2011**, *13*, 2062; b) Z. Zhang, K. Dong and Z. K. Zhao *ChemSusChem* **2011**, *4*, 112-118; c) H. Joshi, B. R. Moser, J. Toler, W. F. Smith and T. Walker *Biomass and Bioenergy* **2011**, *35*, 3262-3266; d) E. Christensen, A. Williams, S. Paul, S. Burton and R. L. McCormick *Energy Fuels* **2011**, *25*, 5422-5428.

30. a) G. A. Kraus, T. Guney *Green Chem.* **2012**, *14*, 1593-1596; b) L. E. Manzer *Top Catal.* **2010**, *53*, 1193-1196.

31. a) S. C. Brown and J. S. J. Hargreaves *Green Chem.* **1999**, *1*, 17; b) J. A. Melero, J. Iglesias and G. Morales *Green Chem.* **2009**, *11*, 1285; c) K. Suwannakarn, E. Lotero, J. Goodwinjr and C. Lu *J. of Catal.* **2008**, *255*, 279-286; d) G. D. Yadav and A. D. Murkute *J. of Catal.* **2004**, *224*, 218-223; d) Y.-H. Chin, W. E. Alvarez and D. E. Resasco *Catalysis Today* **2000**, *62*, 159; e) A. Corma, A. Martinez and C. Martinez *Appl. Catal. A* **1996**, *144*, 249; f) S. Talwalkar, P. Kumbhar, S. Mahajani *Catal. Commun.* **2006**, *7*, 717-720.

32. a) J. R. Sohn and D. C. Shin *Appl. Catal. B* **2008**, *77*, 386-394; b) H. Nakabayashi *Bull. Chem. Soc. Jpn.* **1992**, *65*, 914.

33. K. Okumura, T. Tomiyama, S. Shirakawa, S. Ishida, T. Sanada, M. Arao and M. Niwa *J. Mater. Chem.* **2011**, *21*, 229.

Chapter 4. Understanding the Role of Gold Nanoparticles in Enhancing the Catalytic Activity of Manganese Oxides in Water Oxidation Reactions.

4.1 Overview and Abstract

The Earth-abundant and inexpensive manganese oxides (MnO_x) have emerged as an intriguing type of catalysts for the water oxidation reaction. However, the overall turnover frequencies of MnO_x catalysts are still much lower than that of nanostructured IrO_2 and RuO_2 catalysts. Herein, we demonstrate that doping MnO_x polymorphs with gold nanoparticles (AuNPs) can result in a strong enhancement of catalytic activity for the water oxidation reaction. For the first time, the catalytic activity of MnO_x/AuNPs catalysts correlates strongly with the initial valence of the Mn centers. By promoting the formation of Mn^{3+} species, a small amount of AuNPs (<5 %) in α-MnO_2/AuNP catalysts significantly improved the catalytic activity up to 8.2 times in the photochemical and 6 times in the electrochemical system, compared with the activity of pure α-MnO_2.

4.2 Introduction

Photochemical and electrochemical water splitting into H_2 and O_2 has received continuous attention over a half century for its potential applications in the renewable energy technologies. The half-photolysis of photochemical water oxidation reaction (WOR) or electrochemical oxygen evolution reaction (OER) [$2H_2O\ (l) - 4e^- \rightarrow 4H^+\ (aq) + O_2(g)$] is known as a complex process involving a four-electron transfer process. The oxygen generation is kinetically slow and has been recognized as a bottleneck that largely limits the overall efficiency of water splitting. The rational

design of numerous novel photochemical or electrochemical catalysts is crucial for the more efficient water oxidation.[1] Inspired by highly active cubane-like $CaMn_4O_x$ photocatalysts, the earth-abundant and inexpensive manganese oxides (MnO_x) have emerged as an intriguing type of catalysts for light-driven and electricity-driven water splitting.[2] MnO_x materials have versatile crystalline/amorphous structures due to the multi-valent nature of Mn element. Given that the complex/variable valence,[2a, 3] multiple polymorphs[1i, 4] and versatile morphologies of MnO_x materials[5] can influence their catalytic activity, considerable efforts have been devoted to developing highly efficient MnO_x catalysts for water splitting in the past few years. The catalytic activity of MnO_x polymorphs for WORs/OERs is dependent upon the presence of Mn^{3+} species[6] which have an antibonding electronic configuration and a longer Mn-O bond than that of Mn^{4+}/Mn^{2+} species.[6d]

A number of recent studies have also shown that the underlying substrate (*e.g.* metal electrode) of the catalysts can largely improve O_2 evolution performance for both WORs and OERs.[7] The incorporation of catalyst and substrate may result in the synergetic coupling effect at their interface, thus leading to the enhancement of catalytic activity.[7g] For instance, Bell's group has demonstrated that cobalt oxide (CoO_x) films deposited on noble metal substrates (*e.g.* Au, Pt and Pd) have exhibited a much higher activity for OERs.[7b] The turnover frequency (TOF) of CoO_x deposited on Au for OERs is nearly 40 times higher than that of bulk CoO_x. Jaramillo *et al.* lately reported that the catalytic activity of Au nanoparticle (AuNP) doped MnO_x films was significantly enhanced and the TOF of AuNPs/MnO_x films was an order of magnitude higher than that of bulk films.[7d] As such, the use of noble metal NPs doped metal oxide catalysts may stand out as a promising opportunity to develop highly active catalysts for WORs/OERs. However, the underlying role of metal NP dopants in the catalytic activity for O_2 evolution is still under debate

in the current literature. A study from Primo *et al*. proposed that the hot electron injection from photoexcited gold NPs (AuNPs) to the catalytic centers may occur to alter the electron transfer pathways for WORs.[8] One model involves the oxidation of water on the surface of AuNPs. Other reports, conversely, show the enhanced OER activity of metal oxide catalysts [7b, 7d] that have core-shell nanostructures[7h] where metal NPs cannot directly interact with water molecules.

In the present study, we choose to focus on five different MnO_x materials doped with AuNPs, *i.e.*, cryptomelane-type α-MnO_2, birnessite-type δ-MnO_2, amorphous MnO_2, cobalt doped α-MnO_2, and cubic bixbyite Mn_2O_3, to further understand the role of metal NPs on the catalytic activity of MnO_x materials. We observed that, for the first time, the catalytic activity of MnO_x/AuNPs for WORs presented a strong correlation with the valence of Mn centers. For the oxidation state of Mn^{4+}, the MnO_x/AuNPs catalysts (<5% Au) showed nearly an order of magnitude higher catalytic activity for WORs/OERs than bulk MnO_x catalysts. The electron transfer from Mn^{2+} to AuNPs was envisaged to improve the catalytic activity of MnO_x/AuNPs. Our study highlights the importance of noble metals in developing mixed metal/metal oxide systems as efficient water oxidation catalysts.

4.3 Experimental Section

4.3.1 Materials

Potassium permanganate (>99%), manganese(II) sulfate monohydrate (>99%), potassium hydroxide (90%), cobalt(II) nitrate hexahydrate (>98%), gold(III) chloride hydrate ($HAuCl_4$, 99.999%), Mn_2O_3 (99 %, ~325 mesh), urea, sodium persulfate (>98%), sodium sulfate (anhydrous, >99%), sodium hexafluorosilicate, and sodium bicarbonate (>99.5%) were purchased from Sigma-Aldrich and used without further purification unless otherwise noted. Photosensitizer, tris(2,2′-

bipyridyl)ruthenium(II) chloride hexahydrate [$Ru(bpy)_3^{2+}$] (98%) was obtained from Strem Chemical Inc. and used as received. The ultra-pure water was obtained using High-Q, Inc. system (model 103S) with resistivity of >10.0 MΩ.

4.3.2 Synthesis of MnO_x Polymorphs

4.3.2.1 Synthesis of α-MnO_2

α-MnO_2 of potassium containing Cryptomelane-type manganese oxide with 2×2 tunneling structure was synthesized using a well-established reflux method. Briefly, in a 500 mL round-bottom flask, 225 mL of potassium permanganate aqueous solution (1.7 M) was added dropwise to a mixture of 67.5 mL of manganese sulfate hydrate aqueous solution (26 M) and 6.8 mL of concentrated nitric acid under strong stirring. The dark-brown slurry was further stirred and refluxed for 24 h. After cooling down to room temperature, the reaction mixture was then filtered to obtain to α-MnO_2 and the final product was washed with distilled water for several times until the filtrates was neutral. The catalyst was dried at 120℃ before use.

4.3.2.2 Synthesis of K-Birnessite δ-MnO_2

δ-MnO_2 of potassium containing Birnessite-type manganese oxide layered material was prepared as following. In a typical synthesis, 200 mL of potassium hydroxide solution (0.3 M in water/EtOH (1:1, vol) solution) was added dropwise to 150 mL of potassium permanganate aqueous solution (0.4 M) under vigorous stirring. The resulting mixture was stirred for 1 h and aged at 80℃ for 48 h. The product was washed with deionized water for several times until the filtrate was neutral. The collected material was dried at 80℃ before use.

4.3.2.3 Synthesis of Cobalt Doped α-MnO_2

The synthesis of cobalt doped α-MnO_2 was described as following. In a 500 mL round-bottom flask equipped with condenser, 225 mL of potassium permanganate solution (0.4 M) and 50 mL of cobalt nitrate (0.6 M) were added dropwise to a mixture of 67.5 mL of manganese sulfate hydrate solution (1.75 M) and 6.8 mL of concentrated nitric acid. After completing addition, the dark brown slurry was further refluxed for 24 h, then filtered and washed with distilled deionized water several times until the filtrate was neutral. The catalyst was dried at 120℃ before use.

4.3.3 Synthesis of AuNPs/MnO_x Catalysts

The post-treatment of AuNPs deposited on the manganese oxide materials was synthesized according to a reported procedure.[1] In general, 100 mg of manganese oxide materials and 1 g of urea with 10 mL of ultra-pure water were placed in a 25 mL vial with a stir bar. The predetermined amount of $HAuCl_4$ solution (25 mg/mL) was added subsequently. After sonication for five minutes, the reaction mixture was then heated to 85℃ for one hour. After cooling down, the reaction suspension was filtered and washed with deionized water. The collected material was dried at 120℃ then further calcinated at 250℃ for 2 hr.

4.3.4 Water Oxidation Test of Manganese Oxide and Au Containing Manganese Oxide Materials

Photochemical water oxidation tests were conducted in a 20 mL quartz reaction vessel containing 3 mg of the catalyst, 1.5 mM $Ru(bpy)_3^{2+}$, 13 mM $Na_2S_2O_8$, and 68 mM Na_2SO_4 in 15 mL buffered aqueous solutions (0.022-0.028 M Na_2SiF_6 - $NaHCO_3$ solution with pH ~ 5.8). Reactants in the quartz vessel were sonicated for 1 min and purged with argon for 10 min to remove

all dissolved oxygen from the aqueous solution. The quartz vessel was then irradiated with a continuous output xenon lamp set at 250-W power. A cut-off bandpass filter (λ>400 nm ± 10 nm) was placed in between the quartz vessel and the light source. The amount of dissolved oxygen was measured using an automatic temperature-compensated needle-type oxygen microsensor based on a 140 µm optical fiber (Microx TX3-trace, Presens).

4.3.5 OER Evaluation

Cyclic voltammograms (CVs) were obtained with a CHI 660A electrochemical workstation (CH instruments). For electrochemical oxygen evolution measurements, pyrolytic graphite carbon working electrodes were used (surface area ~ 0.18 cm^2) equipped with a rotating disc working electrode (RDE) configuration. A platinum wire was used as a counter electrode and saturated calomel electrode (SCE) as reference electrode. The potentials reported in this work are referenced to the reversible hydrogen electrode (RHE) and denoted as RHE potential. The preparation of the working electrode is as follows: 5 mg of the catalysts was dispersed in 1 mL of water by sonication. Then 45 µL of Nafion solution was added and sonicated for another 1 min. 8 µL of obtained solution were dropped on the working electrode surface and dried overnight before use. CV curves were iR-compensated and performed from 0.05 to 1.95 V with a sweep rate of 10 mV s^{-1} in oxygen saturated 0.1 M KOH solution. The working electrode was rotated at 1600 rpm.

The calculation of mass activity and TOF in this work is based on literature published by Guo et al. [2]. Mass activity (A g^{-1}) values were obtained from deposited material on the working electrode (~ 0.2 mg) with measured current density (j, mA cm^{-2}) at η = 0.35 V. Mass activity = j/m, where j is the current density at 10 mV and m is the mass of material loaded on the electrode surface. Turnover frequency (TOF) values were obtained using the following equation and

assuming all materials on the working electrode are involved in the reaction. TOF = $j\ S\ /\ 4F{\cdot}n$, where j (mA cm^{-2}) is the measured current density at $\eta = 0.35$ V, S represent the surface area of the working electrode, F is Faraday's constant, and n is the moles of the metal atom on the working electrode.

4.3.6 Characterization

The crystallinity of as-synthesized materials was characterized using a Rigaku UltimaIV power X-ray diffractometer (XRD) with Cu K_α radiation and a tube voltage of 40 kV and current of 44 mA. Morphologies of catalysts were studied using high resolution transmission electron microscopy (HR-TEM) and field emission scanning electron microscopy (FE-SEM). HRTEM studies were carried out using a JEOL 2010 transmission electron microscope with an accelerating voltage of 200 kV. TEM samples were prepared by casting the suspension of material on a carbon coated copper grid (300 mesh). FE-SEM studies were carried out using Zeiss DSM 982 Gemini FE-SEM with a beam current of 1 mA and a Schottky emitter operating at 2 kV. For the surface analysis, the X-ray photoelectron spectroscopy (XPS) was performed on a PHI model 590 spectrometer with multi-probes (Physical Electronics Industries Inc.), using Al K_α ($\lambda = 1486.6$ eV) as the radiation source. The powder samples were pressed on carbon tape mounted on adhesive copper tape stuck to a sample stage placed in the analysis chamber. Raman measurements were recorded using a Renishaw 2000 Ramascope attached to a charge-coupled device (CCD) camera, with an Ar^+ ion laser (514.4 nm) as the excitation source. Before each measurement was taken, the spectrometer was calibrated with a silicon wafer. The chemical compositions of the as-synthesized materials were characterized with energy dispersive X-ray spectroscopy (EDX) with an FEI Nova NanoSEM 450 SEM equipped with an Oxford X-max80 EDX analyzer operating at an electron

accelerating voltage of 10 kV. The determination of specific surface area and pore size distribution was done using a Quantachrome autosorb iQ surface area system using N_2 gas as the adsorbate at 77 K. Prior to the experiments all the samples were degassed at 150℃ for 12 h. The XAFS data were collected at the National Synchrotron Light Source at Brookhaven National Laboratory utilizing beam line X18A.

4.3.7 X-ray Absorption Spectroscopy Data Reduction and Data Analysis

Energy $E_{0,exp}$ of the raw data was determined from the first inflection point in the spectra. Afterwards the difference between the obtained energy $E_{0,exp}$ and the tabulated absorption edge energy of the manganese K-edge ($E_{0,ref}$ = 6.539 keV) was used to calibrate the raw data. Background subtraction and normalization were performed by fitting a linear polynomial to the pre-edge region and a cubic polynomial to the post-edge region of the absorption spectrum. A smooth atomic background, $\mu_0(k)$, was obtained using cubic splines. The number of splines was nine and the k weight was three. The fitting range in k space was set from 2.4 to 14 $Å^{-1}$. After XAFS data reduction, the radial distribution function FT($\chi(k)$) was obtained by Fourier transforming the k^3-weighted experimental $\chi(k)$, multiplied by a Bessel window, into the R space. EXAFS data analysis was performed using theoretical backscattering phases and amplitudes obtained from FEFF calculations. The model structure was α-MnO_2.

EXAFS fitting and simulation were performed using the standard EXAFS formula. The fit was carried out in R space in the R range from 1.0858 to 3.4569 Å. The number of single-scattering (SS) paths was 3. For the studied system the number of independent parameters was 19 and the number of free running parameters was 7. Structural parameters that are determined by a least-square EXAFS fit to the experimental spectra are the bond length R, the Debye-Waller factors σ^2

and the E_0 shifts. The coordination numbers were kept invariable in the refinement. The reduction factor S_0^2 was also kept invariable and set to 0.9. E_0 shifts were correlated while the Debye-Waller factors and the bond lengths were allowed to run free. EXAFS refinements were conducted in *R* space to magnitude and imaginary part of a Fourier transformed k^3-weighted experimental $\chi(k)$.

A satisfactory refinement could already be obtained by taking into account only single-scattering paths. In this work it sufficed to consider three scattering shells in the chosen R range. The refinement was also carried out by entering two distances into the Mn-O-shell, but an improvement of the *R*-value could not be achieved. Hence, it was decided to consider the Mn-O distance of 1.89 Å, the Mn-Mn_{edge} distance of 2.86 Å and the Mn-Mn_{corner} distance of 3.47 Å of the structure model α-MnO_2 for the refinement.

4.4 Results and Discussion

Various MnO_x polymorphs were synthesized by following the reported procedures.[9] AuNPs were deposited on the surface of MnO_x materials through chemical reduction of $HAuCl_4$ using urea. The growth of AuNPs on MnO_x catalysts was confirmed by transmission electron microscopy (TEM) as shown in **Figure 4.1a** and **c**. **Figure 4.1a** shows TEM images of as-prepared cryptomelane-type α-MnO_2 nanorods with an average diameter of ~20 nm and a length of 200-500 nm. AuNPs have an average diameter of 4 nm and are well-dispersed on the surface of α-MnO_2 nanorods. The amount of Au deposited on α-MnO_2 was determined by energy dispersive X-ray (EDX) spectroscopy. By adjusting the ratio of $HAuCl_4$ and MnO_x, the doping amount of AuNPs could be readily controlled in the range of 0.9% to 5.8%. Catalysts are denoted as MnO_2/AuNP-*n* hereafter, where *n* is the percentage of Au relative to Mn.

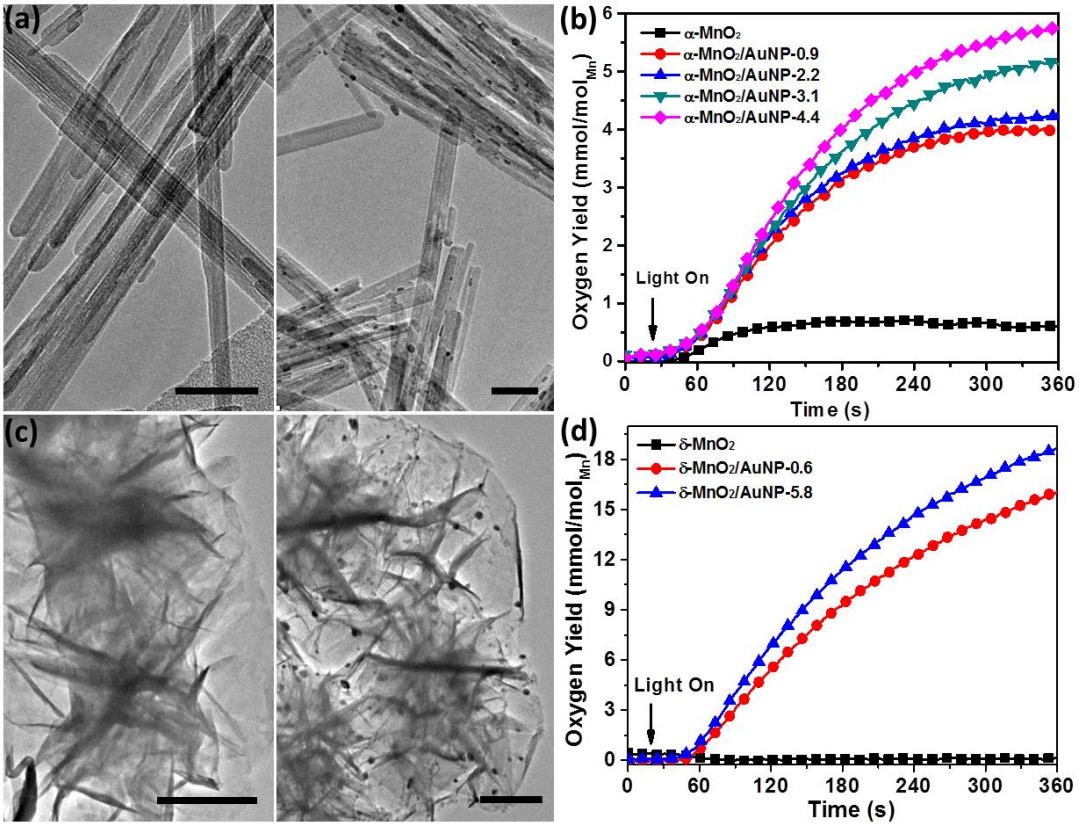

Figure 4.1 (a,c) TEM images of MnO_x (left) and MnO_x/AuNP (right) catalysts: (a) α-MnO_2 and α-MnO_2/AuNP-4.4; and (c) δ-MnO_2 and δ-MnO_2/AuNP-5.8. Scale bars are 50 nm in (a) and 200 nm in (c). (b,d) Dissolved O_2 concentration measured under visible light irradiation (~400 nm) using α-MnO_2/AuNP (b) and δ-MnO_2/AuNP (d) as catalysts. Conditions: 1.5 mM of $Ru(bpy)_3^{2+}$, 13 mM of $Na_2S_2O_8$, 68 mM of Na_2SO_4 and 3 mg of catalysts in a 15 mL of Na_2SiF_6-$NaHCO_3$ buffer solution (pH ~5.8). The WOR results were confirmed by three individual measurements at least.

Other MnO_2 polymorphs, including birnessite-type δ-MnO_2 (**Figure 4.1c**), amorphous MnO_2, cobalt doped α-MnO_2 rods, and bixbyite Mn_2O_3 were deposited with AuNPs using a similar procedure. The crystallinity of MnO_x/AuNP catalysts was further confirmed by X-ray diffraction (XRD) and Raman spectroscopy. No noticeable change in crystalline structures of MnO_x polymorphs was found in all samples after Au deposition. The surface area of MnO_x/AuNPs is close to that of pure MnO_x and no obvious changes were observed.

The catalytic performance of MnO_x polymorphs was first evaluated for WORs as photocatalysts utilizing well-established $Ru(bpy)_3^{2+}$-$S_2O_8^{2-}$ system. The overall photoelectrochemical reaction of this system is $2Ru(bpy)_3^{2+} + S_2O_8^{2-} + hv \rightarrow 2Ru(bpy)_3^{3+} + SO_4^{2-}$, where $Ru(bpy)_3^{2+}$ is a photosensitizer and $S_2O_8^{2-}$ is a sacrificial electron acceptor. Formed $Ru(bpy)_3^{3+}$ species can be reduced back to $Ru(bpy)_3^{2+}$ by pulling one electron from the catalyst where water molecules lose electrons and get oxidized to form O_2. The generated O_2 in solution was measured using a needle-type oxygen microsensor upon exposure to visible light (λ>400 nm). Using α-MnO_2/AuNPs and δ-MnO_2/AuNPs as photocatalysts, WOR results are presented in Figs 1b and d. Pure α-MnO_2 exhibited a moderate oxygen evolution rate and the dissolved oxygen content was ~0.7 mmol/mol Mn after 3 min (**Figure 4.1b**); while pure δ-MnO_2 showed nearly no activity for WORs and no significant oxygen content was detected (below 0.2 mmol/mol Mn) (**Figure 4.1d**). Similar results were reported by Robinson[6d] and Bharat[10]. The deposition of a small amount of AuNPs on both α-MnO_2 and δ-MnO_2 led to a significantly higher rate of oxygen generation. The dissolved oxygen content increased from 4.0 mmol/mol Mn for α-MnO_2/AuNP-0.9 to 5.8 mmol/mol Mn for α-MnO_2/AuNP-4.4 with increased loading of AuNPs on α-MnO_2. The TOF of 1.70×10^{-5} s^{-1} for α-MnO_2/AuNP-4.4 calculated from WOR results is 8.2 times higher than that of pure α-MnO_2 (see **Table 4.1**). For δ-MnO_2/AuNPs, a dramatic enhancement of WOR activity was of particular note and ~18 mmol/mol Mn of O_2 was generated. The TOF of δ-MnO_2/AuNP-5.8 is 5.1×10^{-5} s^{-1}, close to that of Mn_2O_3[2a]. Likewise, the enhancement of WOR activity was found in the other two types of MnO_2 polymorphs, including amorphous MnO_2 and cobalt doped α-MnO_2 rods. Moreover, the increase of doping contents of AuNPs in MnO_x polymorphs seemed to further improve the catalytic activity; but this effect is

Table 4.1 Summarized WOR and OER activities of α-MnO_2 and α-MnO_2/AuNP catalysts[a]

Catalysts	η at J = 10 mA/cm^{-2} (V)	Mass activity at η =0.35 V (A g^{-1})	TOF at η =0.35 V (s^{-1})	TOF of WORs
α-MnO_2	0.63[b]	2.4	0.004	2.08×10^{-6}
α-MnO_2/AuNP-0.9	0.54	4.5	0.009	1.18×10^{-5}
α-MnO_2/AuNP-2.2	0.46	4.7	0.012	1.25×10^{-5}
α-MnO_2/AuNP-3.1	0.41	10.3	0.029	1.51×10^{-5}
α-MnO_2/AuNP-4.4	0.39	14.7	0.039	1.70×10^{-5}

[a]Detailed calculation methods were given in SI. [b]The overpotential of pure α-MnO_2 was obtained at highest current density of 9.6 mA.

minimal[11]. WOR results suggest that the addition of AuNPs to MnO_x polymorphs results in a much higher photochemical catalytic activity.

To further explore the enhanced catalytic activity of MnO_2/AuNP catalysts, the OER performance of α-MnO_2/AuNP was also measured for electrochemical oxidation of water by cyclic voltammetry (CV). The voltammograms of α-MnO_2/AuNPs with various contents of AuNPs under alkaline conditions (0.1 M KOH, pH ~13) are shown in **Figure 4.2**. Larger current density and lower over potential of water oxidation were obtained with a higher loading amount of AuNPs. The over potential (η) at the current density (j) of 10 mA/cm^{-2} is 0.39 V for α-MnO_2/AuNP-4.4, compared to pure α-MnO_2 with η=0.63 V (**Table 4.1**). The mass activity of α-MnO_2/AuNP-4.4 at η=0.35 V is ~6 times higher than that of pure α-MnO_2; while the TOF of α-MnO_2/AuNP-4.4 for OERs is roughly 10 times higher than that of pure α-MnO_2. It is quite challenging to compare the catalytic activity to that of previously published MnO_x catalysts as the sample preparation and measurement conditions vary. However, under similar conditions, Fekete *et al*. reported the electrochemical activity of nanostructured β-MnO_2 catalysts and found that the over potential at J=10 mA/cm^{-2} is 0.55 V in NaOH solution (0.1 M), which is close to that of pure α-MnO_2 in this work.[12] The recent report from Gorlin and Jaramillo showed that the electrodeposited

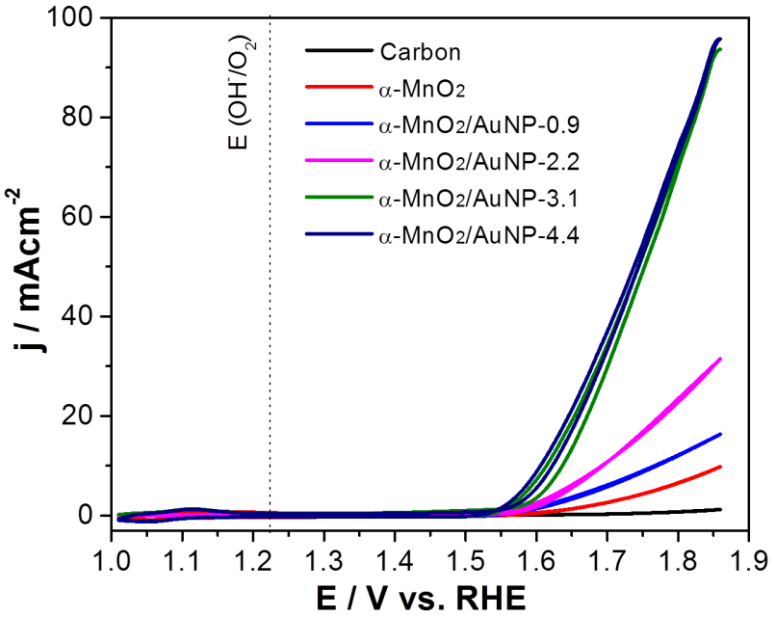

Figure 4.2 Cyclic voltammetry studies of α-MnO_2 and α-MnO_2/AuNP for electrochemical oxidation of water. All measurements were carried out in O_2 purged 0.1 M KOH solution at a scan rate of 10 mVs^{-1} with a RDE rotation rate of 1600 rpm.

MnO_x/AuNP composite catalyst has an over potential of 0.35 V at J=10 mA/cm^{-2}.[7d] Similar effects from AuNP doping are shown in the study we present here.

How does catalytic intriguing synergy of MnO_x/AuNPs for water splitting occur? To investigate synergetic effects, it is useful to address two important factors focusing on the *ex situ* material characterization as well as the reaction mechanism: i) the influence of AuNPs on structural evaluation and surface properties of MnO_x, including the crystalline structures of MnO_x and the valence/oxidation state of Mn; and ii) the influence of AuNPs on the reaction pathways and catalytic centers, *e.g.* whether AuNPs can act as co-catalysts or new active centers instead of Mn. As aforementioned, macroscopic crystalline structures of MnO_x catalysts were not influenced by the presence of AuNPs. The enhancement of WORs may be ascribed to the change in either the surface properties of MnO_2/AuNP catalysts or the *in situ* involvement of AuNPs in the WOR mechanism.

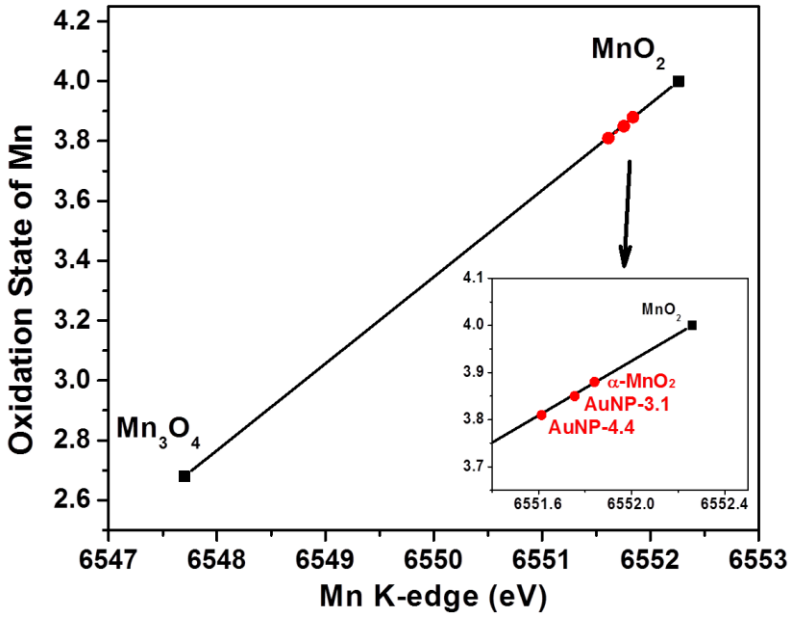

Figure 4.3 The average oxidation state of Mn for α-MnO_2 and α-MnO_2/AuNP catalysts derived from Mn K-edge absorption threshold.

The surface property of MnO_2/AuNPs catalysts was first investigated by X-ray photoelectron spectroscopy (XPS). The high resolution XPS spectra of Mn 2p region present two peaks at 642.2 eV and 653.8 eV assigned to Mn $2p_{3/2}$ and $2p_{1/2}$, respectively. The difference in binding energy of the two peaks frequently used for characterizing Mn^{3+} and Mn^{4+} ratios did not display any significant change as compared to that of pure α-MnO_2. However, the Mn K-edge X-ray absorption near-edge structure (XANES) analysis of MnO_2/AuNPs catalysts suggested a slight change in the average oxidation state of Mn (**Figure 4.3**). The overall features of Mn K-edge XANES spectra are quite similar for all samples of α-MnO_2/AuNP. Extended X-Ray Absorption Fine Structure (EXAFS) also revealed no significant influence of gold loading on the average Mn-O and Mn-Mn distances (**Table 4.2**). However, a decreasing XAFS amplitude indicated an increasing Mn-O and Mn-Mn distance distribution with gold loading. The slight shift from 6551.84 (α-MnO_2) to 6551.61 eV (α-MnO_2/AuNP-4.4) corresponds to the decrease of Mn oxidation state from 3.91 (α-MnO_2)

Table 4.2 EXAFS curve fitting parameters[a]

Sample	Pair	CN_{fixed}	R [Å]	σ^2 [Å ^{2}]	E_0 [eV]	Fit residual R [%]
α-MnO_2	Mn-O	6	1.91	0.0034	-5.0	7.689
	Mn-Mn	4	2.88	0.0037		
	Mn-Mn	4	3.45	0.0039		
α-MnO_2/AuNP-0.9	Mn-O	6	1.91	0.0055	-5.6	12.46
	Mn-Mn	4	2.88	0.0060		
	Mn-Mn	4	3.45	0.0061		
α-MnO_2/AuNP-3.1	Mn-O	6	1.90	0.0056	-4.8	9.252
	Mn-Mn	4	2.88	0.0064		
	Mn-Mn	4	3.45	0.0067		
α-MnO_2/AuNP-4.4	Mn-O	6	1.92	0.0070	-4.6	12.74
	Mn-Mn	4	2.89	0.0079		
	Mn-Mn	4	3.46	0.0088		

[a]Fit range in *R* space 1.0858 Å to 3.4569 Å ; *k* range from 2.4 Å to 14 Å ; N_{idp} =19; N_{free} = 7; Number of SS paths = 3; S_0^2 = 0.9; α-MnO_2 as theoretical model.

to 3.84 (α-MnO_2/AuNP-4.4).[7d] This small shift in binding energy indicates that, i) the localized electronic interaction of MnO_2 and AuNPs is present to lowwer Mn valence; and ii) the weak, positive charge of AuNPs will compensate the valence change of Mn, resulting in the formation of Mn species with lowered oxidation state.[13] The co-presence of positive Au ions (Au^{3+}) was further confirmed by Au 4f XPS spectra.

To explore the influence of AuNPs on the reaction pathway and catalytic centers, more control experiments were performed. First, the individual AuNPs (citrate stabilized AuNPs with diameter of 3~5 nm) were tested for WORs and no oxygen was detected. Second, by physically mixing AuNPs and α-MnO_2, no enhancement of catalytic activity compared to that of pure α-MnO_2 was observed. Third, the catalytic performance of Mn_2O_3 and Mn_2O_3/AuNPs catalysts for WORs was examined using the identical conditions of $Ru(bpy)_3^{2+}$-$S_2O_8^{2-}$ system (see **Figure 4.4**). There is no significant difference in the catalytic activity of Mn_2O_3, Mn_2O_3/AuNP-0.4 and Mn_2O_3/AuNP-3.9

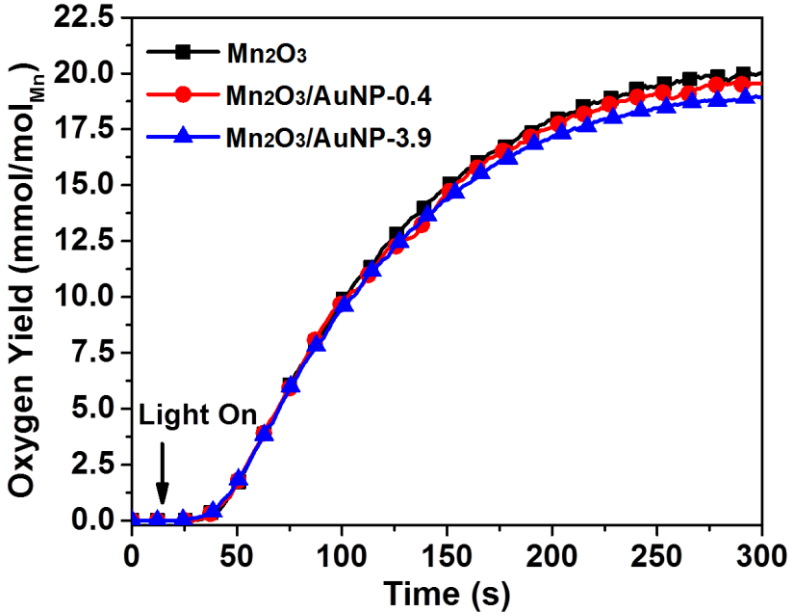

Figure 4.4 Dissolved O_2 concentration measured using Mn_2O_3 and Mn_2O_3/AuNPs catalysts under visible light irradiation (>400 nm).

catalysts for WORs. The TOF value of 4.39×10^{-5} s^{-1} for Mn_2O_3 is close to that of Mn_2O_3/AuNPs, 4.14×10^{-5} s^{-1} (within 5% difference). We can conclude from the above results, i) AuNPs are catalytically "inactive" for WORs without the presence of MnO_2 catalysts in photochemical system; ii) the mixture of AuNPs with MnO_2 did not promote the activity of MnO_2, indicating that the interaction of AuNPs and MnO_2 is localized and diminished at long distance; and iii) the deposition of AuNPs on Mn_2O_3 do not improve its WOR activity, implying that only Mn^{3+} species are the catalytic centers and AuNPs are not directly involved in the WORs. This suggests that AuNPs cannot act as the catalytic centers for WORs or modify the electron transfer pathways from water molecules to catalytic centers.

In general, Mn^{3+} has a very labile Mn-O bond compared to that of Mn^{4+}/Mn^{2+} species and it can act as precursors for O_2 evolution. The active Mn^{3+} species can be generated by the electron injection from H_2O to Mn^{4+} ions in MnO_2. [6b] However, they are rather unstable under natural or acidic conditions; and the disproportionation of Mn^{3+} to Mn^{2+} and Mn^{4+} species occurs quickly to

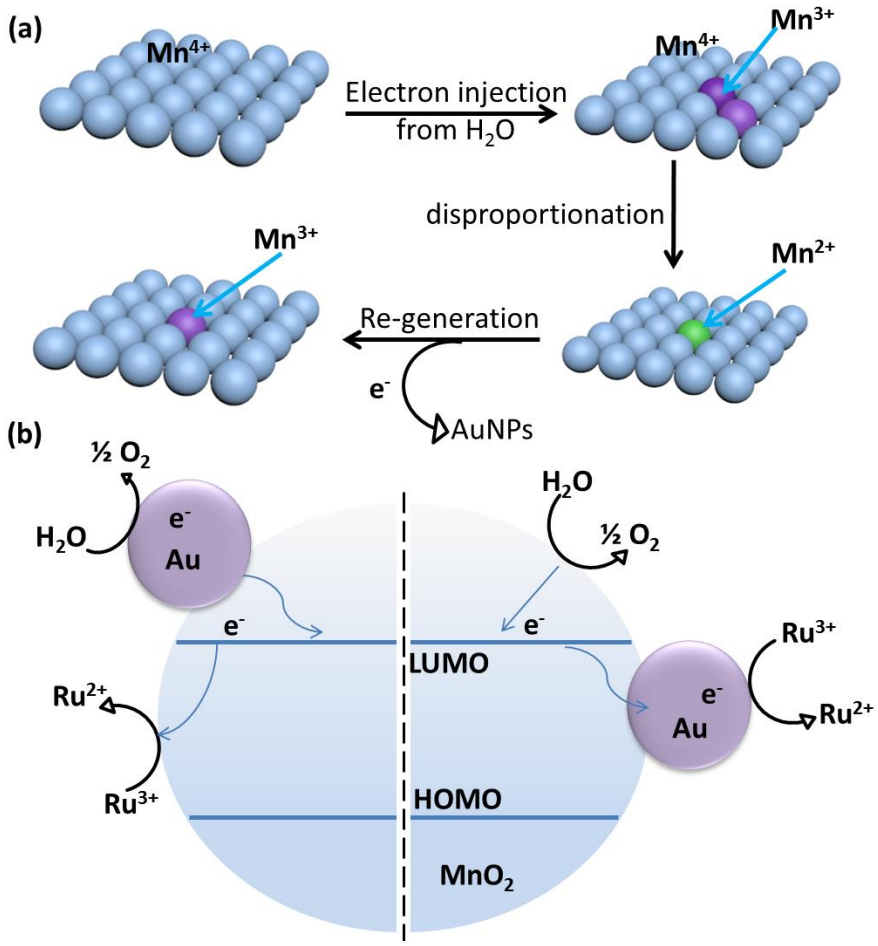

Scheme 4.1 (a) The changes in oxidation state of Mn catalytic centers in photochemical water oxidation. (b) Schematic illustration of mechanism for photochemical water oxidation on MnO_x/AuNPs catalysts. The proposed electron transfer pathways describe two possibilities involving electron loss of water molecules on AuNPs (left) or MnO_2 (right).

diminish the active Mn^{3+}centers for WORs (**Scheme 4.1a**), $2Mn^{3+} \rightarrow Mn^{2+} + Mn^{4+}$. The equilibrium concentration of Mn^{3+} species is less than 10^{-14}% of the initial concentration of Mn^{4+} and Mn^{2+} at pH~6.[6b] Based on our observation of valence-dependent catalytic activity, it is reasonable to deduce that AuNPs in MnO_2/AuNPs catalysts promote the *in situ* formation of active Mn^{3+} species for WORs. One hypothesis is that, the electron loss of Mn^{2+} species to AuNPs through the following reaction, $2Mn^{2+} + 3H_2O \rightarrow Mn_2O_3 + 2e^- + 6H^+$, to re-generate Mn^{3+} catalytic centers (**Scheme 4.1a**). In this redox reaction, the electron transfer from Mn^{2+}/Mn^{3+} (E^o=

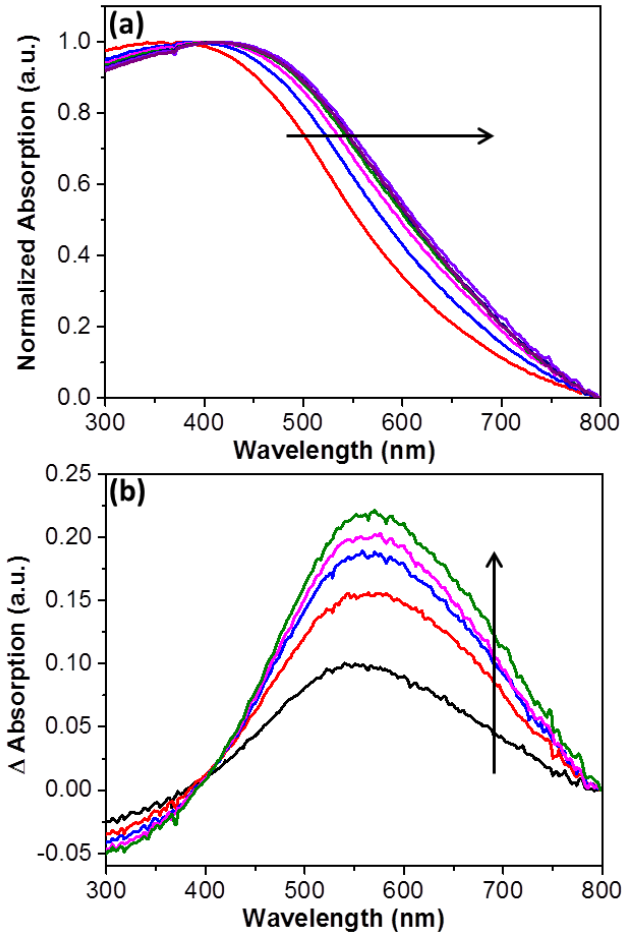

Figure 4.5 (a) Time-resolved UV-vis absorption spectra of α-MnO_2/AuNP-4 (0.1 mg/mL) in the presence of $Na_2S_2O_8$. The absorption spectra of above solution were measured immediately after the addition of $Na_2S_2O_8$ at an interval of 1 min. (b) Spectral changes of UV-vis absorption of α-MnO_2/AuNP-4.4 in 6 minutes by subtracting the reference spectrum recorded at 1 min. The arrows are to indicate the increase of reaction time.

+1.49V) redox pairs to AuNPs (note that, Au^+/Au of E^o= +1.83V and Au^{3+}/Au of E^o= +1.52V) continuously yields Mn^{3+} species. The results presented in **Figure 4.3** clearly demonstrate that the localized electronic interaction of MnO_2 and AuNPs leads to the weakly positive charge. The electron transfer pathway will increase the concentration of surface Mn^{3+} species, but not directly impact the electron loss of water molecules. For Mn_2O_3 catalysts, Mn^{3+} species pre-exist; thus, no change in activity of Mn_2O_3/AuNP catalysts was observed. Moreover, the electronic

communication of AuNPs and other metal oxide semiconductors has been reported previously at a metal-semiconductor interface, *e.g.* AuNPs/TiO_2[14] and AuNPs/WO_3[15]. AuNPs may also increase the electron transfer efficiency at the metal-semiconductor interface,[14b] compared to catalytic materials and Ru^{2+}/Ru^{3+} redox species.

We have examined the *in situ* change of the oxidation state of Mn species using UV-vis spectroscopy. As shown in **Figure 4.5a**, α-MnO_2 displayed a broad peak centered at ~370 nm in aqueous solution, corresponding to the *d-d* transition band gap of MnO_2.[16] The broadness of the absorption peak is due to the coexistence of lower oxidation states of Mn in α-MnO_2.[6a] For instance, Mn^{3+} species in the octahedral center induce a red-shift of the absorption band due to the single spin-allowed *d-d* transition and the change transfer between Mn^{3+}-O.[16b] The spectral change of α-MnO_2/AuNP-4.4 catalysts (0.1 mg/mL) was recorded in the presence of $Na_2S_2O_8$ as an electron acceptor at a time interval of 1 min (**Figure 4.5a**). The gradual red-shift of the absorption peak (~50 nm) of α-MnO_2 to a longer wavelength occurs with increasing reaction time. The change in absorption of α-MnO_2 as a function of reaction time is plotted in **Figure 4.5b**. The new peak appearing at 540-560 nm is ascribed to the generation of surface Mn^{3+} species. The control experiments were performed with pure α-MnO_2 without AuNPs and α-MnO_2 mixed with free AuNPs under identical conditions. No absorption shift was observed in these experiments.

The spectral changes of α-MnO_2/AuNP-4.4 suggest that AuNPs promote the formation of active Mn^{3+} species. The electron transfer between Mn and $S_2O_8^{2-}$ is known to be thermodynamically favorable ($S_2O_8^{2-}/SO_4^{2-}$ of E^o=2.1 V) but proceed at a kinetically slow rate. The redox reaction cannot be measured without the presence of AuNPs. The role of AuNPs is likely to enhance the electronic communication between Mn and redox species *e.g.* $S_2O_8^{2-}/SO_4^{2-}$ and Ru^{2+}/Ru^{3+}, by pulling electrons from the catalysts (**Scheme 4.1b**). Similar results were

reported in OERs using metal oxides (Co and Ni) with noble metals, where noble metals generated and stabilized metal ions at higher oxidation states (*e.g.* Co^{4+} and Ni^{3+}). Such species are recognized as active centers for the water oxidation reaction. Of greater relevance to our present study, Casella *et al.*[17] and Yeo *et al.*[7f] demonstrated that the growth of Ni hydroxide on Au electrode favors the oxide of Ni^{3+} over Ni^{2+}. Yeo *et al.* also noted that the cobalt oxide deposited on Au electrodes exhibits a high occurrence of Co^{4+} species on the surface.[7b] The enhanced activity was correlated to the electronegativity of noble metals.

4.5 Conclusion

In summary, we have systematically studied five different MnO_x/AuNP catalysts for both WORs and OERs. The enhanced catalytic activity of MnO_x by depositing AuNPs has been confirmed in both photochemical and electrochemical systems. By doping a small amount of AuNPs (<5%), the catalytic activity of α-MnO_2/AuNP was significantly enhanced up to 8.2 times in photochemical and 6 times in electrochemical system compared with pure α-MnO_2. The catalytic activity of MnO_x/AuNPs was found to be strongly correlated to the valence of Mn centers. The enhanced electronic communication Mn and redox species that solely promote the *in situ* formation of active Mn^{3+} species for WORs played a key role for the higher catalytic activity of MnO_2/AuNPs. Our results may provide fundamental guidance to prepare highly active transition metal oxide catalysts for both WORs and OERs.

4.6 References

(1) a) M. Bajdich, M. García-Mota, A. Vojvodic, J. K. Nørskov, A. T. Bell, *J. Am. Chem. Soc.* **2013**, *135*, 13521-13530; b) B. S. Yeo, A. T. Bell, *J. Am. Chem. Soc.* **2011**, *133*, 5587-5593; c) T. Takashima, K. Hashimoto, R. Nakamura, *J. Am. Chem. Soc.* **2012**, *134*, 18153-18156; d) R. Subbaraman, D. Tripkovic, K.-C. Chang, D. Strmcnik, A. P. Paulikas, P. Hirunsit, M. Chan, J. Greeley, V. Stamenkovic, N. M. Markovic, *Nat. Mater.* **2012**, *11*, 550-557; e) J. Rosen, G. S. Hutchings, F. Jiao, *J. Am. Chem. Soc.* **2013**, *135*, 4516-4521; f) F. Jiao, H. Frei, *Angew. Chem. Int. Ed.* **2009**, *48*, 1841-1844; g) Q. Yin, J. M. Tan, C. Besson, Y. V. Geletii, D. G. Musaev, A. E. Kuznetsov, Z. Luo, K. I. Hardcastle, C. L. Hill, *Science* **2010**, *328*, 342-345; h) M. W. Kanan, D. G. Nocera, *Science* **2008**, *321*, 1072-1075; i) D. M. Robinson, Y. B. Go, M. Greenblatt, G. C. Dismukes, *J. Am. Chem. Soc.* **2010**, *132*, 11467-11469.

(2) a) M. M. Najafpour, T. Ehrenberg, M. Wiechen, P. Kurz, *Angew. Chem. Int. Ed.* **2010**, *49*, 2233-2237; b) J. Yano, J. Kern, K. Sauer, M. J. Latimer, Y. Pushkar, J. Biesiadka, B. Loll, W. Saenger, J. Messinger, A. Zouni, *Science* **2006**, *314*, 821-825.

(3) a) D. M. Robinson, Y. B. Go, M. Mui, G. Gardner, Z. Zhang, D. Mastrogiovanni, E. Garfunkel, J. Li, M. Greenblatt, G. C. Dismukes, *J. Am. Chem. Soc.* **2013**, *135*, 3494-3501; b) I. Zaharieva, P. Chernev, M. Risch, K. Klingan, M. Kohlhoff, A. Fischer, H. Dau, *Energy Environ. Sci.* **2012**, *5*, 7081-7089; c) A. Yamaguchi, R. Inuzuka, T. Takashima, T. Hayashi, K. Hashimoto, R. Nakamura, *Nat. Commun.* **2014**, *5*, 4256.

(4) a) A. Iyer, J. Del-Pilar, C. K. King'ondu, E. Kissel, H. F. Garces, H. Huang, A. M. El-Sawy, P. K. Dutta, S. L. Suib, *J. Phys. Chem. C* **2012**, *116*, 6474-6483; b) F. Zhou, A. Izgorodin, R. K. Hocking, V. Armel, L. Spiccia, D. R. MacFarlane, *ChemSusChem* **2013**, *6*, 643-651.

(5) a) V. B. R. Boppana, F. Jiao, *Chem. Commun.* **2011**, *47*, 8973-8975; b) F. Zhou, A. Izgorodin, R. K. Hocking, L. Spiccia, D. R. MacFarlane, *Adv. Energy Mater.* **2012**, *2*, 1013-1021.

(6) a) A. Iyer, J. Del-Pilar, C. K. King'ondu, E. Kissel, H. F. Garces, H. Huang, A. M. El-Sawy, P. K. Dutta, S. L. Suib, *J Phys Chem C* **2012**, *116*, 6474-6483; b) T. Takashima, K. Hashimoto, R. Nakamura, *J Am Chem Soc* **2012**, *134*, 1519-1527; c) T. Takashima, K. Hashimoto, R. Nakamura, *J Am Chem Soc* **2012**, *134*, 18153-18156; d) D. M. Robinson, Y. B. Go, M. Mui,

G. Gardner, Z. J. Zhang, D. Mastrogiovanni, E. Garfunkel, J. Li, M. Greenblatt, G. C. Dismukes, *J Am Chem Soc* **2013**, *135*, 3494-3501.

(7) a) M. R. Gao, Y. F. Xu, J. Jiang, Y. R. Zheng, S. H. Yu, *J Am Chem Soc* **2012**, *134*, 2930-2933; b) B. S. Yeo, A. T. Bell, *J Am Chem Soc* **2011**, *133*, 5587-5593; c) S. Yusuf, F. Jiao, *Acs Catal* **2012**, *2*, 2753-2760; d) Y. Gorlin, C. J. Chung, J. D. Benck, D. Nordlund, L. Seitz, T. C. Weng, D. Sokaras, B. M. Clemens, T. F. Jaramillo, *J Am Chem Soc* **2014**, *136*, 4920-4926; e) M. S. El-Deab, M. I. Awad, A. M. Mohammad, T. Ohsaka, *Electrochem. Commun.* **2007**, *9*, 2082-2087; f) B. S. Yeo, A. T. Bell, *J Phys Chem C* **2012**, *116*, 8394-8400; g) Y. Y. Liang, Y. G. Li, H. L. Wang, J. G. Zhou, J. Wang, T. Regier, H. J. Dai, *Nat Mater* **2011**, *10*, 780-786; h) Z. Zhuang, W. Sheng, Y. Yan, *Adv Mater* **2014**, 3950-3955.

(8) A. Primo, T. Marino, A. Corma, R. Molinari, H. Garcia, *J Am Chem Soc* **2011**, *133*, 6930-6933.

(9) a) H. Cao, S. L. Suib, *J. Am. Chem. Soc.* **1994**, *116*, 5334-5342; b) Q. Gao, O. Giraldo, W. Tong, S. L. Suib, *Chem. Mater.* **2001**, *13*, 778-786.

(10) V. B. R. Boppana, F. Jiao, *Chem Commun* **2011**, *47*, 8973-8975.

(11) L. Trotochaud, S. L. Young, J. K. Ranney, S. W. Boettcher, *J. Am. Chem. Soc.* **2014**, *136*, 6744-6753.

(12) M. Fekete, R. K. Hocking, S. L. Y. Chang, C. Italiano, A. F. Patti, F. Arena, L. Spicci, *Energ Environ Sci* **2013**, *6*, 2222-2232.

(13) A. K. Sinha, K. Suzuki, M. Takahara, H. Azuma, T. Nonaka, K. Fukumoto, *Angew Chem Int Edit* **2007**, *46*, 2891-2894.

(14) a) J. J. Zhao, C. R. Bradbury, D. J. Fermin, *J Phys Chem C* **2008**, *112*, 6832-6841; b) J. N. Chazalviel, P. Allongue, *J Am Chem Soc* **2011**, *133*, 762-764; c) A. Furube, L. Du, K. Hara, R. Katoh, M. Tachiya, *J Am Chem Soc* **2007**, *129*, 14852-14853.

(15) A. Tanaka, K. Hashimoto, H. Kominami, *J Am Chem Soc* **2014**, *136*, 586-589.

(16) a) Y. Omomo, T. Sasaki, L. Z. Wang, M. Watanabe, *J Am Chem Soc* **2003**, *125*, 3568-3575; b) F. Milella, J. M. Gallardo-Amores, M. Baldi, G. Busca, *J Mater Chem* **1998**, *8*, 2525-2531.

(17) I. G. Casella, M. R. Guascito, M. G. Sannazzaro, *J Electroanal Chem* **1999**, *462*, 202-210.

Chapter 5. Robust Mesoporous Manganese Oxide Catalysts for Water Oxidation.

5.1 Overview and Abstract

Inspired by the natural oxygen evolution reaction of Photosystem II, the earth-abundant and inexpensive manganese oxides (MnO_x) have been recognized for their great potential as highly efficient and robust materials for water oxidation reaction (WORs). To date, most of the heterogeneous, synthesized MnO_x catalysts still exhibit lower activities for WORs, in comparison to RuO_2 and IrO_2. Herein, we report a single-step and scalable synthesis method for mesoporous MnOx materials that is developed through a soft-templated method. This method allowed precise control of Mn^{3+}-rich Mn_2O_3 structure as well as pore sizes and crystallinity of these mesoporous MnO_x. These catalysts were investigated for both photochemical and electrochemical water oxidation, and they presented a superior activity for water oxidation. The highest turnover frequency of 1.05×10^{-3} s^{-1} was obtained, which is comparable with those for precious metal oxide based catalysts (RuO_2 and IrO_2). Our results illustrate a guideline to the design and synthesis of inexpensive and highly active heterogeneous catalysts for water oxidation.

5.2 Introduction

The design of highly active catalysts for solar-driven water oxidation reactions (WORs) is critical to develop integrated artificial photosynthetic systems. Inspired by the Photosystem II system catalyzed by Mn tetramer clusters of $CaMn_4O_5$,[1-3] earth-abundant and inexpensive manganese oxides (MnO_x) have been recognized for their great potential as highly efficient and robust catalysts of WORs.[4] However, the documented catalytic activity of MnO_x for WORs is still rather

low: at least 1 order of magnitude lower than that of IrO_2 and RuO_2. In order to improve the catalytic activity of MnO_x, much effort has been devoted to the study of structural properties: e.g., the valence of Mn centers and the surface properties of catalysts.[5-11] Mn^{3+} species having longer Mn−O−Mn bonds were found to be much more active for WORs than Mn^{2+}/Mn^{4+} species. Mn^{3+}-rich structures with labile Mn−O bonds allow for the formation of surface Mn−OH_2 species and the cleavage of Mn−O_2 bonds, which facilitates WORs and increases the overall turnover frequency (TOF) of the catalytic centers.[12-16] The controllable synthesis of MnO_x with enriched Mn^{3+} species is therefore highly desired. In addition, the control of surface properties of MnO_x catalysts, e.g. surface area and surface oxygen mobility,[5,17] is known to be very critical for WORs as well. For instance, mesoporous catalysts exhibited better catalytic performance for WORs in comparison to bulk catalysts.[18-20] Jiao et al. reported that nanometer-sized MnO_x catalysts supported on mesoporous silica were highly active for WORs.[19] The high surface area of the silica support played a critical role in the performance of these catalysts. However, the preparation of mesoporous MnO_x catalysts via the hard template approach involves a complicated and time-consuming process that limits the practical applications of those materials. Moreover, the precise control over the crystallinity and valence of MnO_x based transition-metal oxides is still challenging due to the different possible coordination numbers and oxidation states of Mn centers.

Herein, we report a facile and general synthesis of high quality mesoporous MnO_x with the crystal structure of Mn_2O_3 using a one-step inverse micelle templating approach.[21] Our synthesis procedure involves a simple sol-gel process using manganese nitrate as a precursor and nonionic surfactant P123 as a soft template. By varying the calcination temperature, manipulation of the crystal structures and size of the Mn_2O_3 phase of the materials from the amorphous to the bixbyite

Mn_2O_3 structure is possible. In comparison to previous species prepared by a nano-casting (using a hard template) approach, our synthetic approach has the advantages of (i) being a single step wet-chemical synthesis without any post-treatment, (ii) producing large quantities of mesoporous Mn_2O_3 materials on gram scales, (iii) tuning the pore size, surface area, and crystallinity of Mn_2O_3 materials, and (iv) most importantly, precisely controlling the valence transition of MnO_x to enrich the amount of Mn^{3+}. The mesoporous Mn_2O_3 materials exhibit superior activities for photocatalytic WORs. A TOF of 1.05×10^{-3} s^{-1} for WORs, to the best of our knowledge, is the highest TOF using synthetic MnO_x reported so far.[2,4,5,7,8]

5.3 Experimental Section

5.3.1 Materials

Manganese (II) nitrate tetrahydrate ($Mn(NO_3)_2 \cdot 4H_2O$, ≥97%), 1-butanol (anhydrous, 99.8%), nitric acid (HNO_3, 68~70%), Mn_2O_3 (99%, ~325 mesh), poly(ethylene glycol)-block-poly(propylene glycol)-block-poly(ethylene glycol) (PEO_{20}-b-PPO_{70}-b-PEO_{20}, Pluronic P123), Na_2SiF_6, $Na_2S_2O_8$, Na_2SO_4, and $NaHCO_3$ were purchased from Sigma-Aldrich and used without further purification unless otherwise noted. K-Cryptomelane α-MnO_2, K-Birnessite δ-MnO_2 and amorphous manganese oxide (AMO) were synthesized followed published literature.[5] Photosensitizer of tris(2,2′-bipyridyl)ruthenium(II) chloride hexahydrate [$Ru(bpy)_3^{2+}$] (98%) and commercial RuO_2 were obtained from Strem Chemical Inc. and used as received. The ultra-pure water was obtained using High-Q, Inc. system (model 103S) with resistivity of >10.0 MΩ.

5.3.2 Synthesis of Mesoporous Mn_2O_3

Manganese (II) nitrate tetrahydrate (1.2 g, 4.78 mmol) was first dissolved in *n*-butanol (10 g, 0.13 mol), HNO_3 (~3.5 g in 68% solution, 0.38 mol) and P123 surfactant (1.2 g) in a 150 mL beaker at room temperature under strong stirring. The solution was then placed in preheated oven at 120 °C for 3 h. The obtained deep-brown powder was washed several times with ethanol to remove the excess surfactant by centrifugation. The final powder product was dried at 40 °C under vacuum overnight. The dry powder was then subjected to heating cycles to achieve desired crystal structures and mesopore sizes. The sample was firstly heated at 150 °C for 12 hr. The collected material was denoted as Mn-150. The further heating processes were followed by 250 °C for 6 hr, 350 °C for 4 hr, 450 °C for 2 hr and 550 °C for 1 hr, and the obtained samples were denoted as Mn-250, Mn-350, Mn-450, and Mn-550, respectively. All heat treatments were done under air atmosphere. Be cautious that, the annealing treatment of all samples was performed in ovens with proper ventilation due to release of toxic NO_x gas from the gel.

5.3.3 Water Oxidation Reaction of Mesoporous Mn_2O_3

Photochemical water oxidation tests were conducted in a 20 mL quartz reaction vessel containing 3 mg of the catalyst, 1.5 mM $Ru(bpy)_3^{2+}$, 13 mM $Na_2S_2O_8$, and 68 mM Na_2SO_4 in 15 mL of buffered aqueous solutions (0.022-0.028 M Na_2SiF_6-$NaHCO_3$ solution with pH~5.8). Reactants in the quartz vessel were sonicated for 1 min and purged with argon for 5 min to remove all dissolved oxygen from the aqueous solution. The quartz vessel was then irradiated with a continuous output xenon lamp (250 W). A cut-off filter (λ>400±10 nm, SCHOTT North America, Inc.) was placed in between the quartz vessel and the light source to remove UV light. The amount

of dissolved oxygen was measured using an automatic temperature-compensated needle-type oxygen microsensor based on a 140 μm optical fiber (Microx TX3-trace, Presens).

5.3.4 Electrochemical Oxygen Evolution Study

Linear sweep voltammetry (LSV), electrochemical impedance (EIS), and chronopotentiometry experiments were obtained with a CHI 660A electrochemical workstation. For electrochemical oxygen evolution studies, pyrolytic graphite carbon working electrodes were used (surface area ~0.14 cm^2) equipped with a rotating disc working electrode (RDE) configuration. A platinum wire was used as a counter electrode and saturated calomel electrode (SCE) as the reference electrode. The potentials reported in this work are referenced to the reversible hydrogen electrode (RHE) and denoted as RHE potential. The preparation of the working electrode is as follows: 4 mg of catalysts and 0.4 mg of carbon (VulcanXC-72) were dispersed in 2 mL of water/EtOH by sonication. Then, 19 μL of Nafion solution was added and sonicated for another 20 min. 15 μL of mixture solution were dropped on the working electrode surface and dried overnight before use. CV curves were *i*R-compensated and performed from 1.21 to 1.81 V (vs. RHE) with a sweep rate of 5 mV s^{-1} in oxygen saturated 0.1 M of KOH solution. The working electrode was rotated at 1600 rpm. The electrochemical impedance spectra were applying an AC voltage with 5 mV amplitude in a frequency ranged from 0.01 to 100 kHz for 5 cycles. To check fitting results selected experimental data was also fitted using the ZSimDemo software package (version 3.2). In this procedure, RC initial estimates were obtained using a circle fitting function. Similar fitting parameters were obtained using both software packages. For chronopotentiometric test, the current density was fixed at 5 mA/cm^2 for the anodic reaction.

The calculation of mass activity and TOF of electrochemical studies in this work is based on literature published by Guo et al.[22] Mass activity (A g^{-1}) values were obtained from deposited the catalytic materials on the working electrode (~0.03 mg) with measured current density (j, A cm^{-2}) at η = 0.35 V. Turnover frequency (TOF) values were obtained using the following equation and assuming all materials on the working electrode are involved in the reaction, using TOF= jS/4Fn, where j (A cm^{-2}) is the measured current density at η = 0.35 V, S (cm^2) represent the surface area of the working electrode, F (C mol^{-1}) is Faraday's constant, 4 is the number of the electrons involved in the reaction, and n (mol) is the moles of the metal atom on the working electrode.

5.3.5 Detailed Characterization

The crystallinity of as-synthesized materials was characterized using a Rigaku UltimaIV power X-ray diffractometer (PXRD) with Cu K_α radiation and a tube voltage of 40 kV and current of 44 mA. The low-angle PXRD patterns were collected over a 2θ range of 0.5~10° with a continuous scan rate of 0.5° min^{-1}, where the wide-angle PXRD patterns were collected over a 2θ range of 5~75° with a continuous scan rate of 1.0° min^{-1}. Morphologies of catalysts were studied using high resolution transmission electron microscopy (HR-TEM) and field emission scanning electron microscopy (FE-SEM). HRTEM studies were carried out using a JEOL 2010 transmission electron microscope with an accelerating voltage of 200 kV. TEM samples were prepared by casting the suspension of material on a carbon coated copper grid (300 mesh). FE-SEM studies were carried out using Zeiss DSM 982 Gemini FE-SEM with a beam current of 1 mA and a Schottky emitter operating at 2 kV. For the surface analysis, the X-ray photoelectron spectroscopy (XPS) was performed on a PHI model 590 spectrometer with multi-probes (Physical Electronics Industries

Inc.), using Al K_α (λ = 1486.6 eV) as the radiation source. The powder samples were pressed on carbon tape mounted on adhesive copper tape stuck to a sample stage placed in the analysis chamber. The XPS spectra were analyzed and fitted using CasaXPS software (version 2.3.12). The C 1s photoelectron line at 284.6 eV was used as a reference for correction of the surface charging. A mixture of Gaussian (70%) and Lorentzian (30%) functions was used for the least-squares curve fitting procedure. Raman measurements were recorded using a Renishaw 2000 Ramascope attached to a charge-coupled device (CCD) camera, with an Ar^+ ion laser (514.4 nm) as the excitation source. Before each measurement was taken, the spectrometer was calibrated with a silicon wafer. The determination of specific surface area (by BET method) and pore size distribution (by BJH desorption method) were done using a Quantachrome autosorb iQ surface area system using N_2 gas as the adsorbate at 77 K. Prior to the experiments all the samples were degassed at 150ºC for 12 h or 6 h.. The XAFS data were collected at the National Synchrotron Light Source (NSLS) at Brookhaven National Laboratory utilizing beam line X18A. A Silicon (111) double crystal monochromator was used to monochromatize the synchrotron radiation. The incident and transmitted beam intensities were monitored using ionization chambers filled with N_2. The samples were diluted by h-BN with a ratio of (1:8) then pressed into pellets and mounted in front of transmission detector. Before the measurements were taken, a thin Mn foil reference was used for energy calibration. The XANES data were analyzed using Athena software where background and post and pre-edge corrections were made.

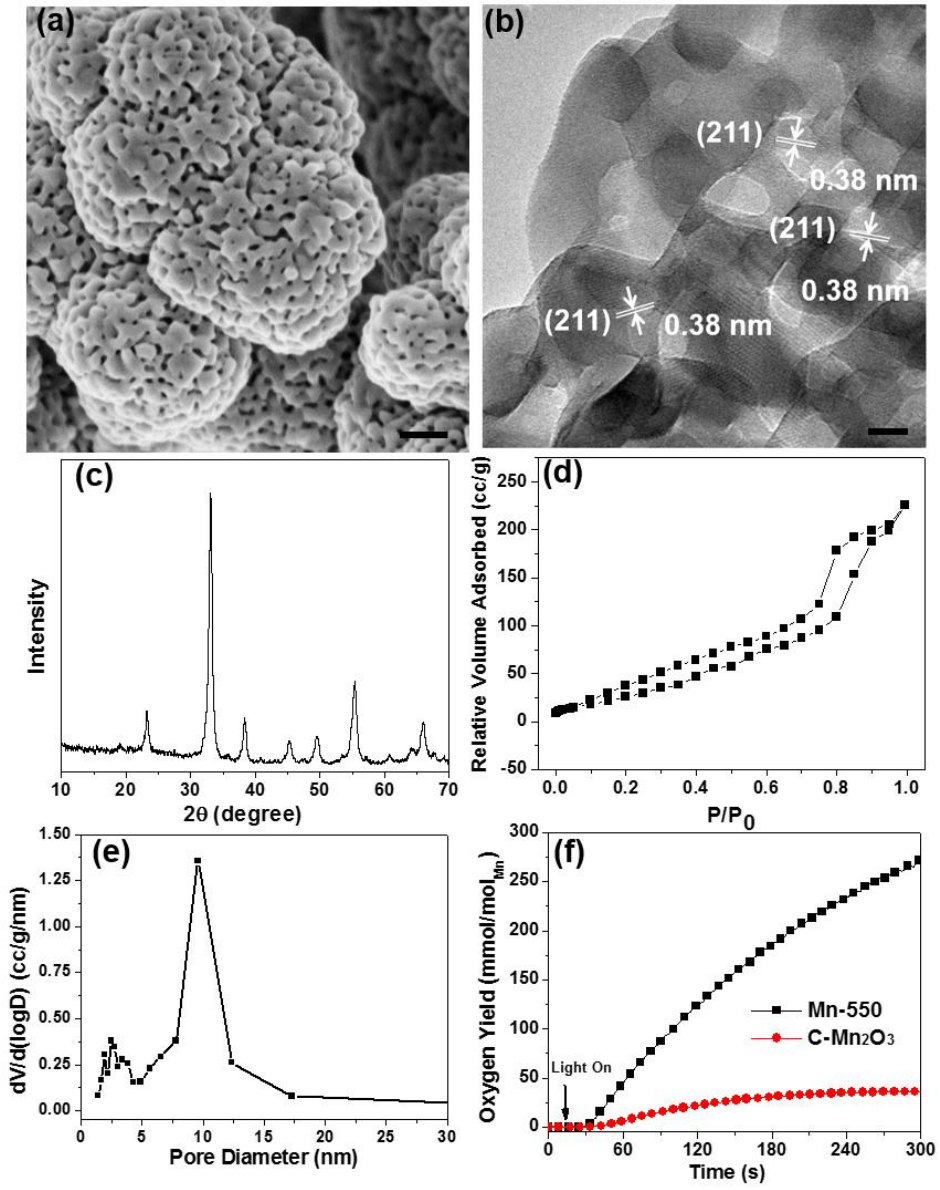

Figure 5.1 (a) SEM and (b) high-resolution TEM images of mesoporous Mn-550 catalyst, respectively. The measured lattice distance of 0.38 nm in (b) is correlated to (211) plane of bixbyite α-Mn_2O_3 structures. Scale bars are 50 nm in (a) and 10 nm in (b). (c) The powder XRD pattern of Mn-550 catalyst. (d,) Nitrogen adsorption isotherm and (e) BJH desorption pore distribution diagram of the Mn-550 catalyst. (f) The dissolved oxygen concentration of photochemical water oxidation for Mn-550 and C-Mn_2O_3 (commercial Mn_2O_3) catalysts. Conditions: 1.5 mM of $Ru(bpy)_3^{2+}$, 13 mM of $Na_2S_2O_8$, 68 mM of Na_2SO_4 and 3 mg of catalysts in a 15 mL of Na_2SiF_6-$NaHCO_3$ buffer solution (pH ~ 5.8). The WOR results were confirmed by at least three individual measurements.

5.4 Results and Discussion

The synthetic procedures of mesoporous Mn_2O_3 catalysts are given in experimental section.[21,23] Briefly, manganese (II) nitrate, P123 and nitric acid were first dissolved in *n*-butanol. After stirring for 30 min to generate a homogeneous clear solution, the reaction mixture was placed in an oven running at 120 ^oC for 3 hours. The collected solids were further washed with excess ethanol to remove the surfactant (solvent extraction). In order to maintain the mesoporosity of the materials, the stepwise annealing process was utilized for the structural transformation of amorphous structure to crystalline mesoporous Mn_2O_3. The materials were subjected to an annealing cycle between 150 to 550 ^oC and denoted as Mn-150~Mn-550 hereafter. The mesoporous Mn-550 catalyst was studied by scanning electron microscopy (SEM) and transmission electron microscopy (TEM) as shown in **Figure 5.1a** and **b**. The SEM image clearly showed the porous structure of the material. The crystal domain size of Mn_2O_3 as well as its pore size are in the range of 10~20 nm. High-resolution TEM analysis showed the crystalline bixbyite structure of Mn_2O_3. The measured *d*-spacing of 0.38 nm is attributed to (211) plane of Mn_2O_3. The powder X-ray diffraction (PXRD) pattern clearly shows the main diffraction peaks of (211), (222), (400), (332), (431), (440), and (622) planes, confirming the bixbyite Mn_2O_3 structures.[24] The size of aggregated Mn_2O_3 nanoparticles estimated from Scherrer's equation is approximately 17.3 nm, which is consistent with our TEM observations. The mesoporosity with uniform pore size distribution of Mn-550 was confirmed by Type-IV nitrogen adsorption isotherm followed by a Type I hysteresis loop. The Brunauer-Emmett-Teller (BET) surface area of Mn-550 was estimated to be 120 m^2/g with a pore size of 9.6 nm and a pore volume of 0.42 cc/g.

Photocatalytic water oxidation was studied using a $Ru(bpy)_3^{2+}$-$Na_2S_2O_8$ system ($E(Ru^{3+}/Ru^{2+})$=1.24 V) and mesoporous Mn-550 as a catalyst.[5] The overall photochemical reaction

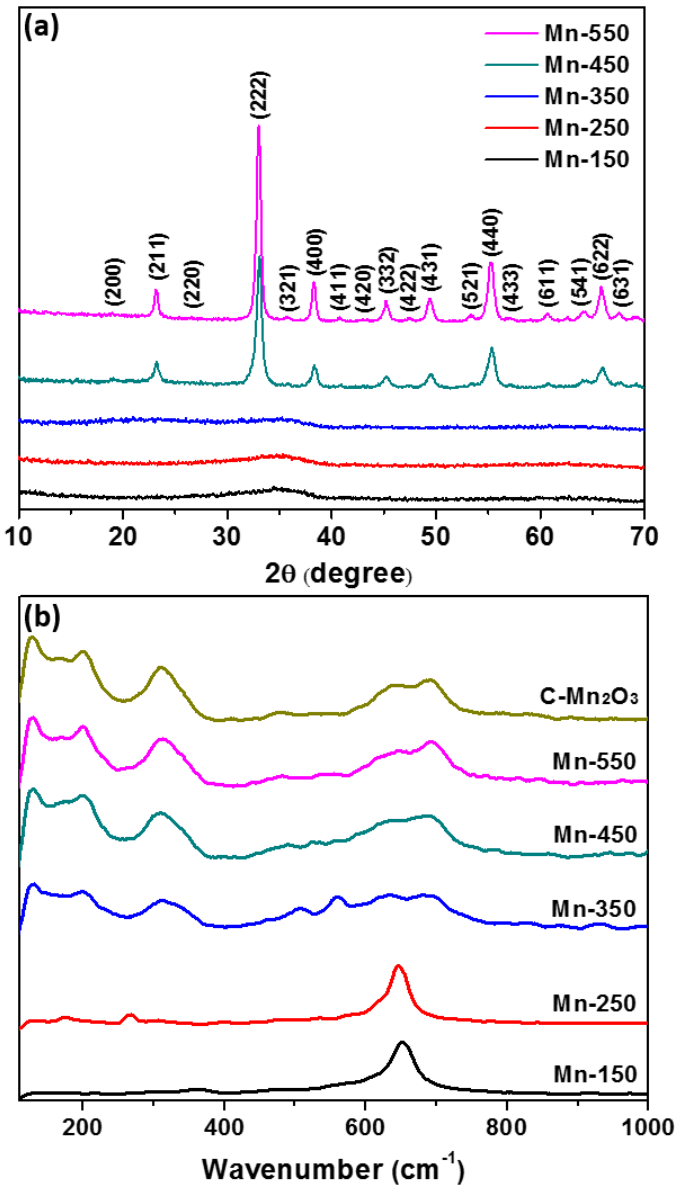

Figure 5.2 (a) The powder XRD patterns and (b) the Raman spectra for synthesized mesoporous MnO_x catalysts with different calcination temperatures. The observed main diffraction peaks of Mn-450 and 550 in (a) are ascribed to bixbyite Mn_2O_3 (211), (222), (400), (332), (431), (440), and (622) planes.

of WORs is, $2Ru(bpy)_3^{2+} + S_2O_8^{2-} + hv \rightarrow 2Ru(bpy)_3^{3+} + SO_4^{2-}$, where $S_2O_8^{2-}$ is the sacrificial electron acceptor. The generated Ru^{3+} species can be reduced back to Ru^{2+} by removing one electron from the Mn catalyst while water molecules are oxidized to form O_2 by losing electrons

to the catalysts. The evolved oxygen concentration was monitored using a needle-like oxygen microsensor (temperature compensated optic oxygen meter). The Mn-550 material showed a superior activity for oxygen evolution under these conditions (**Figure 5.1f**). The dissolved oxygen content quickly increased to 270 mmol/mol Mn after 6 min of irradiation. The TOF number of Mn-550 reached 1.05×10^{-3} s^{-1}, which is nearly one order of magnitude higher than a commercial Mn_2O_3 (C-Mn_2O_3) material which has a TOF of 1.85×10^{-4} s^{-1}. This TOF value is the highest among the synthetic manganese oxides. Mn_2O_3 materials are known to be the most active phase for water oxidation among all manganese oxide phases.[2,12] As a comparison, commercial RuO_2 and Mn_2O_3 were also tested under the same reaction conditions; the RuO_2 has a TOF of 3.87×10^{-3} s^{-1} which is much higher than C-Mn_2O_3; whereas the Mn-550 activity was comparable to that of RuO_2 materials. Such a dramatic enhancement of WOR catalytic activity is presumably because of the high surface area and the uniform mesoporous size distribution of the Mn-550 material.

To understand the correlation between the nanostructures and catalytic performance of mesoporous Mn_2O_3 catalysts, we further investigated the effect of calcination temperatures on the catalytic performances of mesoporous Mn_2O_3 catalysts. The mesoporous MnO_x catalysts calcined at lower temperatures (mesoporous Mn-150, 250 and 350) exhibited poor crystallinity, as shown to be nearly amorphous by XRD (see **Figure 5.2a**). Upon calcination at temperatures of 450 ºC and higher, the bixbyite Mn_2O_3 structure was identified. **Table 5.1** summarizes the physicochemical properties of mesoporous materials obtained at different calcination temperatures. The surface areas of all mesoporous materials are in the range of 129~226 m^2/g, much higher than C-Mn_2O_3 (11 m^2/g). The pore size and pore volume increased solely with calcination temperature due to the increase of nanoparticle size.[21] The crystal domain size of mesoporous Mn_2O_3 was also enhanced with the increase of calcination temperatures as is observed

Table 5.1 Structural parameters of mesoporous manganese oxide materials.

Materials	S_{BET} (m^2/g)[a]	P (nm)[b]	V (cc/g)[c]	L (nm)[d]	D (nm)[e]	Crystal structures (XRD)
Mn-150	129	2.7	0.21	2.6	N/A	amorphous
Mn-250	182	3.4	0.24	7.8	N/A	amorphous
Mn-350	226	3.4	0.24	8.1	N/A	amorphous
Mn-450	150	4.3	0.26	11.5	11.4	Mn_2O_3 (Bixbyite)
Mn-550	120	9.6	0.42	N/A	17.3	Mn_2O_3 (Bixbyite)
C-Mn_2O_3	11	N/A	N/A	N/A	35.4	Mn_2O_3 (Bixbyite)

[a] Surface area obtained from Brunauer-Emmett-Teller (BET) measurements (S_{BET}). [b] BJH desorption pore size distribution (P). [c] BJH desorption pore volume (V). [d] Low-angle XRD peak position (L). [e] Scherrer's crystallite size (D).

from low angle XRD diffraction peaks. For example, the crystal domain size of Mn-150 is ~2.6 nm; while Mn-450 has the crystal domain size of ~11.5 nm. The structural evolution of mesoporous Mn_2O_3 materials obtained at different calcination temperatures was investigated using Raman spectroscopy (see **Figure 5.2b**). For Mn-150 and Mn-250 samples, one strong band at 646 cm^{-1} can be assigned to the Mn-O breathing mode of the divalent Mn ions in tetrahedral coordination and the other small peak at the range of 200 ~ 400 cm^{-1} may correspond to asymmetric stretching of bridging oxygen species (Mn-O-Mn). These spectra are very similar to those of reported amorphous manganese oxide (AMO),[5] suggesting that Mn-150 and Mn-250 possibly consist of layered hydroxides. At higher calcination temperatures, new peaks at 311 cm^{-1} and 570~770 cm^{-1} arise which can be attributed to the out-of-plane bending modes and symmetric stretching of bridge oxygen species (Mn−O−Mn), respectively.[25] These vibrational bands are

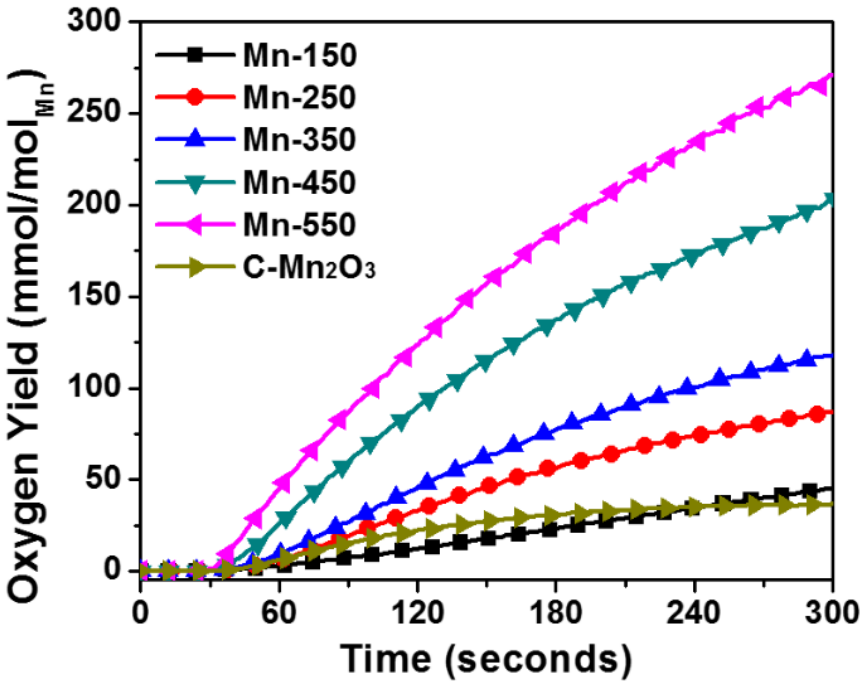

Figure 5.3 The dissolved oxygen concentration of photochemical water oxidation for mesoporous manganese oxide materials calcined at different temperatures. Conditions: 1.5 mM of $Ru(bpy)_3^{2+}$, 13 mM of $Na_2S_2O_8$, 68 mM of Na_2SO_4 and 3 mg of catalysts in a 15 mL of Na_2SiF_6-$NaHCO_3$ buffer solution (pH ~5.8). The WOR results were confirmed by three individual measurements at least.

identical to the Raman spectrum of C-Mn_2O_3, further confirmed the structural transition of MnO_x materials from amorphous layered structures to bixbyite Mn_2O_3. The transition temperature of MnO_x materials in Raman studies is obviously lower than that in XRD results. This is possibly because of the low crystallinity of MnO_x calcined at 350 ^oC that cannot be observed using XRD.

The WOR activities of all samples obtained at different calcination temperatures were studied under identical conditions (**Figure 5.3**). The dissolved oxygen content quickly increased with the increase of calcination temperature, indicating the enhanced catalytic activity for WORs. The turnover number of Mn-150 sample is 1.51×10^{-4} s^{-1}, close to that of non-porous C-Mn_2O_3 sample (see **Table 5.2**). The crystalline mesoporous Mn_2O_3 catalysts calcined at 450 (Mn-450) and 550

Table 5.2 Summarized WOR and OER activities of mesoporous manganese oxide catalysts.

Catalysts	η at J = 10 mA cm^{-2} (mV)	Mass activity at η =0.35 V (A g^{-1})[a]	Resistance R_{ct} (Ω)	TOF at η =0.35 V (s^{-1})	TOF of WORs
MnO-150	N/A[a]	2.75	567	1.57×10^{-4}	1.51×10^{-4}
MnO-250	N/A[a]	21.02	394	1.20×10^{-3}	3.15×10^{-4}
MnO-350	575	25.83	284	1.48×10^{-3}	4.31×10^{-4}
MnO-450	507	35.23	165	2.01×10^{-3}	7.70×10^{-4}
MnO-550	N/A[a]	9.60	539	5.49×10^{-4}	1.05×10^{-3}
C-Mn_2O_3	N/A[a]	2.48	1530	1.42×10^{-4}	1.85×10^{-4}
RuO_2	415	183.62	168	1.15×10^{-2}	3.87×10^{-3}

[a] Failed to reach J = 10 mA/cm^{-2} under our experimental conditions.

^{o}C (Mn-550) obviously exhibited higher activity than the ones calcined at lower temperatures. The TOF number increased from 4.31×10^{-4} s^{-1} to 7.70×10^{-4} s^{-1} when the calcination temperature was increased from 350 to 450 ^{o}C. The formed Mn^{3+}-rich crystalline Mn_2O_3 structures of Mn-450 were believed to be crucial in the improvement of catalytic activity. Upon increasing the calcination temperature to 550 ^{o}C, the TOF of Mn-550 increased to 1.05×10^{-3} s^{-1}, even though the surface area started to decrease.

Electrochemical oxygen evolution reactions (OERs) of mesoporous Mn_2O_3 materials were further explored to confirm WOR results. Using the rotating disc electrode (RDE) system in a three electrode chemical cell, linear sweep voltammetry (LSV) was done in an oxygen saturated 0.1 M KOH solution with a scan rate of 5 mV s^{-1} and a rotation speed of 1600 rpm. The catalytic materials were mounted on the surface of pyrolytic graphite carbon working electrodes before measurements. The OER results are summarized in **Figure 5.4a** and **Table 5.2**. The OER activities of all materials showed similar trends as photochemical systems except Mn-550. Mn-450 exhibited

the highest activity for OERs. The overpotential (η) of Mn-450 at current density of 10 mA cm^{-2} is 507 mV. The calculated TOF of Mn-450 at η = 350 mV is 2.01×10^{-3} which is higher than TOF value (7.70×10^{-4}) from the photochemical system. Again, compared to the non-porous C-Mn_2O_3 with TOF of 1.42×10^{-4}, the Mn-450 is at least one order of magnitude more active than C-Mn_2O_3 materials. Commercial RuO_2 was also tested for OERs under similar conditions. RuO_2 shows a lower overpotential (η = 415 mV) compared to that of Mn-450. However, the current density of Mn-450 surpassed that of RuO_2 after η > 550 mV, suggesting that the electron transfer rate of Mn catalysts may increase faster with the increase of applied potential. Furthermore, the durability of catalysts was examined by chronopotentiometry at a current density of 5 mA/cm^2. The results demonstrate that Mn-450 has a good electrochemical stability along with the activity, as the overpotential remained nearly constant for more than 10 hours. Moreover, the original Mn_2O_3 crystal structure and mesoporosity did not show obvious change after reaction. In case of pure RuO_2 catalyst, unstability is a disadvantage under long charge-discharge cycling test, even though activity is higher.[26] Therefore, combining the above performance factors, mesoporous manganese oxide (Mn-450) is both more durable and feasible than RuO_2.

The electrochemical impedance spectroscopy (EIS) technique was used to elucidate the kinetics and mechanism of oxygen evolution.[27-29] The low frequency area of the Nyquist plot (Zreal vs -Zim) was presented, corresponding to the charge transfer resistance (R_{ct}) of the catalytic materials. The fitted equivalent circuit and model are presented in **Figure 5.4b**. Firstly, the R_{ct} value of commercial Mn_2O_3 is 1530 Ω; while all mesoporous Mn_2O_3 materials have much lower R_{ct} in the range of 165~567 Ω when measured under the same experimental conditions. R_{ct} values increase in the order of Mn-450 > Mn-350 > Mn-250 > Mn-550 > Mn-150. The R_{ct} value is inversely proportional to the electron transfer rate. Therefore, lower R_{ct} value means the material

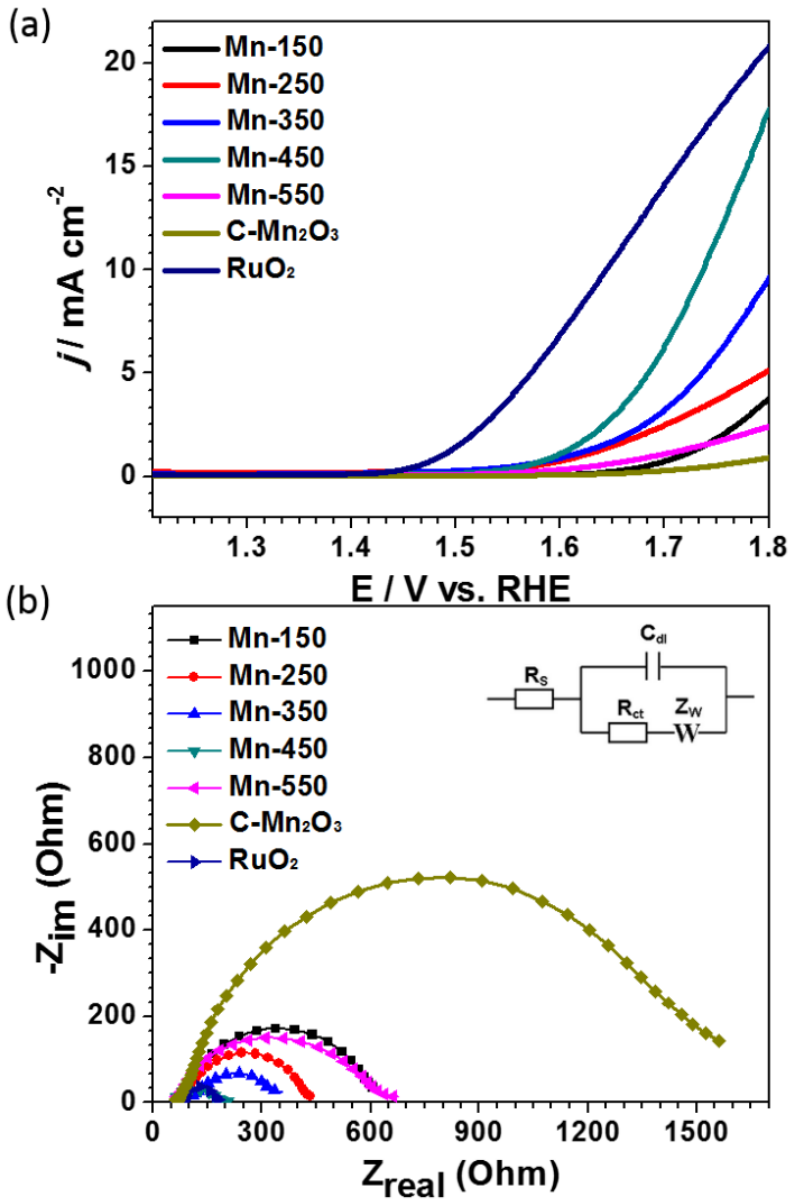

Figure 5.4 (a) Linear sweep voltammetry curves for mesoporous MnO_x materials for electrochemical oxidation of water with comparison to RuO_2. (b) The Nyquist plot at a frequency region of 0.1 to 100000 Hz obtained from electrochemical impedance measurements under applied potential of 1.71 V (vs. RHE). All measurements were carried out in O_2 purged 0.1 M KOH solution at a scan rate of 5 mVs^{-1} with a RDE at a rotation rate of 1600 rpm. The inset graph represents fitted equivalent circuit model used to obtain charge transfer resistance of the OER catalysts. R_s: active electrolyte resistance. C_{dl}: double-layer capacitance. R_{ct}: active charge transfer resistance. Z_w: specific electrochemical element of diffusion W.

has faster electron transfer rate and can be correlated with higher activity in OERs. Overall, the measured R_{ct} values are consistent with the OER activities. Secondly, Mn-450 has similar R_{ct} values to RuO_2 (165 and 168 Ω, respectively). Such enhanced kinetics may be ascribed to the formation of a highly crystalline Mn_2O_3 phase at 450 ^oC that subsequently increases the electronic conductivity of the electrode.

As structural or surface Mn^{3+} species can act as precursors for oxygen production in WORs, a higher Mn^{3+} content might be responsible for the higher WOR activity. To determine the Mn^{3+} content of the catalysts, all mesoporous MnO_x were first studied by X-ray photoelectron spectroscopy (XPS). The Mn $2p_{3/2}$ binding energy slightly decreased from 642.3 eV for Mn-150 to 642.1 eV for Mn-550, indicating an increase of the Mn valence at higher calcination temperatures. The deconvolution of Mn $2p_{3/2}$ peak revealed that the ratio of $Mn^{3+}/Mn^{2+/4+}$ increased with calcination temperature. This further confirmed the phase transition from amorphous hydroxides to Mn^{3+} rich Mn_2O_3 phase with the heat treatment.[30] More detailed valence studies of Mn centers were carried out, using Mn K-edge X-ray absorption near-edge structure (XANES) analysis (**Figure 5.5**). To identify Mn oxidation states, the Mn K-edge absorption threshold was determined from the first derivative of the near-edge region and least squares linear combination fitting was used and accompanied by reference samples.[31,32] Accordingly, the average oxidation state of mesoporous MnO_x materials was found to be gradually increasing from 2.77 to 2.97 (~0.4 eV edge shift) while increasing the calcination temperature from 150 to 550 ^oC. The final valence of Mn was very close to the commercial Mn_2O_3 standard sample. The results clearly showed the oxidization of MnO_x materials during calcination and structure transformation from amorphous hydroxides to bixbyite Mn_2O_3 structures.

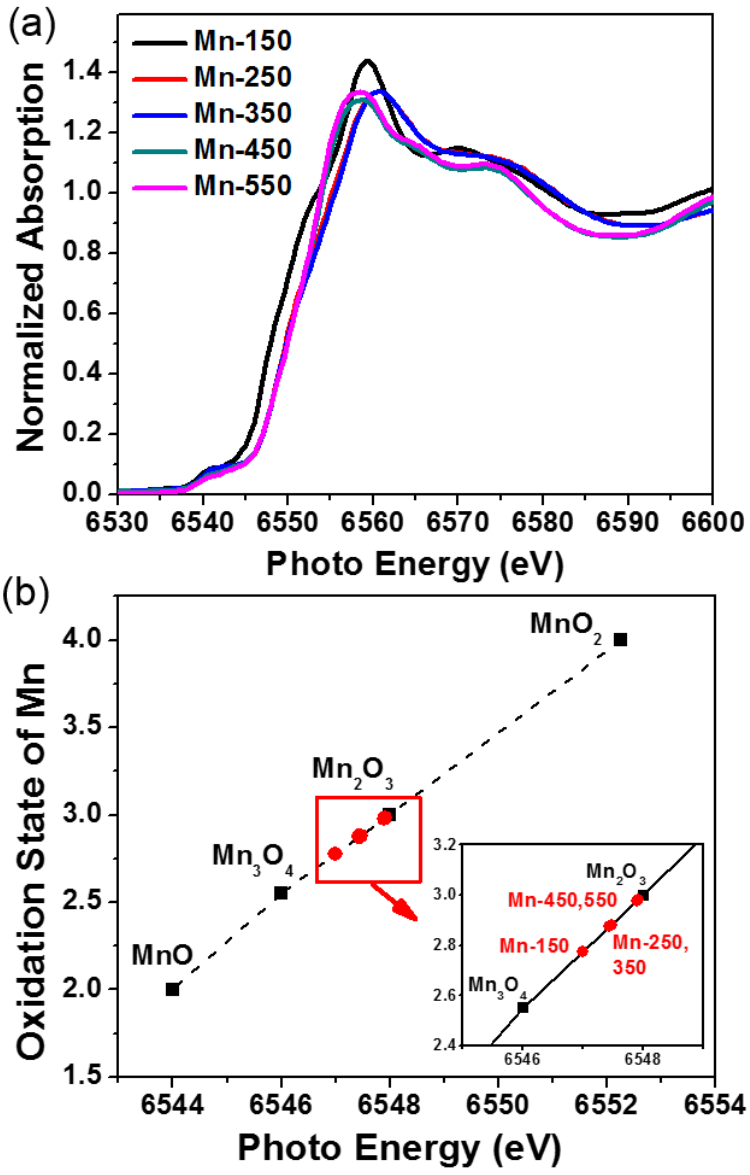

Figure 5.5 (a) X-ray absorption near-edge spectra (XANES) of Mn K-edge spectra of mesoporous Mn_2O_3 materials depicted with normalized Y-axis. (b) The average oxidation state of Mn for mesoporous Mn_2O_3 materials derived from Mn K-edge absorption threshold.

Another structural parameter that might be also important for the enhanced catalytic activity is the high, accessible surface area of these crystalline mesoporous materials. Unlike conventional mesoporous materials, the mesopores in these materials are formed by connected intraparticle voids formed in between the close packed nano-crystals of manganese oxide. The mesopores formed by intraparticle voids show higher thermal stability for applied heat treatments (up to 550^{o}C), resulting in highly crystalline wall structures. Therefore, one can use the combined advantages of the Mn_2O_3 phase and high surface areas for WOR catalysis. The more exposed (accessible) catalyst surface minimizes the mass-transfer limitation and increases the catalytic activity.[33] In order to better evaluate the roles of surface area and crystallinity, we calculated the normalized (w.r.t surface area) TOFs of WORs. The most crystalline C-Mn_2O_3 sample showed the highest surface area normalized activity indicating the crucial role of crystallinity. However, less crystalline Mn-450 sample has higher total activity due to the significantly higher surface area (150 m^2/g vs. 11 m^2/g) despite having lower normalized WOR activity (see **Tables 5.1**). The increase of crystallinity can decrease the trapping of electrons or charge recombination during water oxidation and enhance the electron transfer rate. Similar results have already been reported in TiO_2 related materials.[34,35] However, mesoporous manganese oxides showed better catalytic activity than their commercial analogue (C-Mn_2O_3) because of their both crystalline nature and high surface area.

5.5 Conclusions

In summary, mesoporous MnO_x with tunable mesoporosity and crystallinity along with high surface areas were synthesized via a single step soft-templated (inverse surfactant surfactant

micelles) wet-chemistry approach. The pore sizes as well as the crystallinity of mesoporous MnO_x catalysts can be well-controlled by a simple calcination process without the collapse of mesoporosity. The mesopore sizes can be controlled precisely in the range of ~2.5 to 10 nm while preserving a high surface area (up to 226 m^2/g). The MnO_x materials showed superior activities for WORs and OERs compared to non-porous commercial Mn_2O_3 catalysts. The highest TOF value (1.05×10^{-3} s^{-1}) was achieved by the sample calcined at 550ºC (Mn-550). These TOF numbers are comparable to the most active RuO_2 (3.87×10^{-3} s^{-1}). The enhanced catalytic activity is correlated with the increase of Mn^{3+} concentration (in a highly crystalline Mn_2O_3 phase) with increasing calcination temperature as confirmed by XPS and XANES studies. The high surface area of the mesoporous manganese oxide samples was found to be another crucial parameter dictating the catalytic activity. Our study illustrates a general guideline to the design and synthesis of inexpensive and highly active heterogeneous catalysts for water oxidation.

5.6 References

(1) Yano, J.; Kern, J.; Sauer, K.; Latimer, M. J.; Pushkar, Y.; Biesiadka, J.; Loll, B.; Saenger, W.; Messinger, J.; Zouni, A. *Science* **2006**, *314*, 821-825.

(2) Najafpour, M. M.; Ehrenberg, T.; Wiechen, M.; Kurz, P. *Angew. Chem. Int. Ed.* **2010**, *49*, 2233-2237.

(3) Robinson, D. M.; Go, Y. B.; Greenblatt, M.; Dismukes, G. C. *J. Am. Chem. Soc.* **2010**, *132*, 11467-11469.

(4) Jiao, F.; Frei, H. *Energy Environ. Sci.* **2010**, *3*, 1018-1027.

(5) Iyer, A.; Del-Pilar, J.; King'ondu, C. K.; Kissel, E.; Garces, H. F.; Huang, H.; El-Sawy, A. M.; Dutta, P. K.; Suib, S. L. *J. Phys. Chem. C* **2012**, *116*, 6474-6483.

(6) Boppana, V. B. R.; Jiao, F. *Chem. Commun.* **2011**, *47*, 8973-8975.

(7) Najafpour, M. M. *Dalton Trans.* **2011**, *40*, 3805-3807.

(8) Meng, Y.; Song, W.; Huang, H.; Ren, Z.; Chen, S.-Y.; Suib, S. L. *J. Am. Chem. Soc.* **2014**, *136*, 11452-11464.

(9) Jin, K.; Park, J.; Lee, J.; Yang, K. D.; Pradhan, G. K.; Sim, U.; Jeong, D.; Jang, H. L.; Park, S.; Kim, D.; Sung, N.-E.; Kim, S. H.; Han, S.; Nam, K. T. *J. Am. Chem. Soc.* **2014**, *136*, 7435-7443.

(10) Indra, A.; Menezes, P. W.; Zaharieva, I.; Baktash, E.; Pfrommer, J.; Schwarze, M.; Dau, H.; Driess, M. *Angew. Chem. Int. Ed.* **2013**, *52*, 13206-13210.

(11) Kuo, C. H.; Li, W.; Pahalagedara, L.; El-Sawy, A. M.; Kriz, D.; Genz, N.; Guild, C.; Ressler, T.; Suib, S. L.; He, J. *Angew. Chem. Int. Ed.* **2014**, doi: 10.1002/anie.201407783.

(12) Robinson, D. M.; Go, Y. B.; Mui, M.; Gardner, G.; Zhang, Z.; Mastrogiovanni, D.; Garfunkel, E.; Li, J.; Greenblatt, M.; Dismukes, G. C. *J. Am. Chem. Soc.* **2013**, *135*, 3494-3501.

(13) Zaharieva, I.; Chernev, P.; Risch, M.; Klingan, K.; Kohlhoff, M.; Fischer, A.; Dau, H. *Energy Environ. Sci.* **2012**, *5*, 7081-7089.

(14) Yamaguchi, A.; Inuzuka, R.; Takashima, T.; Hayashi, T.; Hashimoto, K.; Nakamura, R. *Nat. Commun.* **2014**, *5*, 4256.

(15) Takashima, T.; Hashimoto, K.; Nakamura, R. *J. Am. Chem. Soc.* **2012**, *134*, 1519-1527.

(16) Park, J.; Kim, H.; Jin, K.; Lee, B. J.; Park, Y.-S.; Kim, H.; Park, I.; Yang, K. D.; Jeong, H.-Y.; Kim, J.; Hong, K. T.; Jang, H. W.; Kang, K.; Nam, K. T. *J. Am. Chem. Soc.* **2014**, *136*, 4201-4211.

(17) Najafpour, M. M.; Moghaddam, A. N.; Dau, H.; Zaharieva, I. *J. Am. Chem. Soc.* **2014**, *136*, 7245-7248.

(18) Jiao, F.; Frei, H. *Angew. Chem. Int. Ed.* **2009**, *48*, 1841-1844.

(19) Jiao, F.; Frei, H. *Chem. Commun.* **2010**, *46*, 2920-2922.

(20) Rosen, J.; Hutchings, G. S.; Jiao, F. *J. Am. Chem. Soc.* **2013**, *135*, 4516-4521.

(21) Poyraz, A. S.; Kuo, C.-H.; Biswas, S.; King'ondu, C. K.; Suib, S. L. *Nat. Commun.* **2013**, *4*, 2952.

(22) Gao, M.; Sheng, W.; Zhuang, Z.; Fang, Q.; Gu, S.; Jiang, J.; Yan, Y. *J. Am. Chem. Soc.* **2014**, *136*, 7077-7084.

(23) Poyraz, A. S.; Song, W.; Kriz, D.; Kuo, C.-H.; Seraji, M. S.; Suib, S. L. *ACS Appl. Mater. Interfaces* **2014**, *6*, 10986-10991.

(24) Han, Y.-F.; Chen, F.; Zhong, Z.; Ramesh, K.; Chen, L.; Widjaja, E. *J. Phys. Chem. B* **2006**, *110*, 24450-24456.

(25) Baddour-Hadjean, R.; Pereira-Ramos, J.-P. *Chem. Rev.* **2009**, *110*, 1278-1319.

(26) Wang, W.; Guo, S.; Lee, I.; Ahmed, K.; Zhong, J.; Favors, Z.; Zaera, F.; Ozkan, M.; Ozkan, C. S. *Sci. Rep.* **2014**, *4*.

(27) Doyle, R. L.; Lyons, M. E. *Phys. Chem. Chem. Phys.* **2013**, *15*, 5224-5237.

(28) Ye, Z.-G.; Meng, H.-M.; Sun, D.-B. *J. Electroanal. Chem.* **2008**, *621*, 49-54.

(29) He, Z.; Mansfeld, F. *Energy Environ. Sci.* **2009**, *2*, 215-219.

(30) Tang, W.; Wu, X.; Li, D.; Wang, Z.; Liu, G.; Liu, H.; Chen, Y. *J. Mater. Chem. A* **2014**, *2*, 2544-2554.

(31) Liu, F.; Shan, W.; Lian, Z.; Xie, L.; Yang, W.; He, H. *Catal. Sci. Technol.* **2013**, *3*, 2699-2707.

(32) Gorlin, Y.; Lassalle-Kaiser, B.; Benck, J. D.; Gul, S.; Webb, S. M.; Yachandra, V. K.; Yano, J.; Jaramillo, T. F. *J. Am. Chem. Soc.* **2013**, *135*, 8525-8534.

(33) Karger, J.; Valiullin, R. *Chem. Soc. Rev.* **2013**, *42*, 4172-4197.

(34) Maeda, K. *ACS Catal.* **2014**, *4*, 1632-1636.

(35) Joo, J. B.; Zhang, Q.; Dahl, M.; Lee, I.; Goebl, J.; Zaera, F.; Yin, Y. *Energy Environ. Sci.* **2012**, *5*, 6321-6327.

Chapter 6. Facet-dependent catalytic activity of MnO electrocatalysts for oxygen reduction and oxygen evolution reactions.

6.1 Overview and Abstract

The rational design of novel electrocatalysts is crucial for more efficient water oxidation reactions (WORs) and oxygen reduction reactions (ORRs), both known as important energy conversion processes between O_2 and H_2O for renewable energy technologies. The earth-abundant, inexpensive manganese oxides (MnO_x) have emerged as an intriguing type of catalysts for OERs/ORRs, inspired by the photosystem II water-oxidizing complex of $CaMn_4O_x$ clusters. Despite tremendous efforts to improve the electrocatalytic performance of synthetic MnO_x catalysts for OERs/ORRs, the overall turnover frequencies of MnO_x are rather low.

We herein demonstrate a facet-dependent electrocatalytic activity of MnO nanocrystals for OERs/ORRs using halite MnO nanocrystals. Three-dimensional complex anisotropic MnO nanoflowers, polypods, polyhedra and octahedral with selectively oriented MnO crystals were prepared using a limited ligand protection method. MnO polypods exposed (100), (001), and (010) planes on their branched MnO nanorods; while, MnO octahedral nanocrystals exposed (111) planes on all surfaces. We found that MnO (100) planes with higher adsorption energy of O species could largely promote the electrocatalytic activity for OERs/ORRs. MnO polypods were identified as a superior bifunctional electrocatalyst for the overall oxygen electrode activity. Our results may illustrate a guideline to the design and synthesis of inexpensive and highly active MnO_x electrocatalysts.

6.2 Introduction

To meet the growing demands of renewable energy, various electrochemical energy conversion processes between O_2 and H_2O, *e.g.* oxygen evolution reaction (OER) and oxygen reduction reaction (ORR) that are of great importance for solar water splitting and fuel cells, have received much attention in the past decade.[1] A key technical barrier to achieve highly efficient OERs and ORRs is the kinetically slow electron-transfer in which four electrons are involved.[2] The rational design of active electrocatalysts is central to these energy conversion techniques. Traditionally, expensive Pt and its bimetallic alloys have traditionally been the most active catalysts for the ORR;[3] and precious metal oxide IrO_2 and RuO_2 catalysts have proved to be very efficient for the OER.[4] However, the large-scale commercialization of these catalysts is limited by, i) the cost effectiveness of the requisite raw materials, and ii) considerable overpotential (η) required for both the OER and ORR (0.3~0.8 V). The earth-abundant and inexpensive transition metal oxides, *e.g.* manganese oxides (MnO_x), have been explored as alternative electrocatalysts for OERs and ORRs under alkaline conditions.[5] MnO_x families have over 30 different crystal structures and variable valence of Mn centers in different polymorphs.[6] Despite numerous reports on the electrocatalytic performance of MnO_x for OERs and ORRs, insight into the effect of structural parameters, *e.g.* topological structures, surface compositions and energy, and valance of Mn centers on their catalytic activity, is still lacking.[5]

In heterogeneous catalysts, control of complex anisotropic structures with preferentially exposed crystal planes or surface atoms is a key to achieving a high catalytic selectivity and activity. Moreover, the surface interactions between O species and catalytic centers towards the formation of O-O bonds in -OOH species on catalytic centers, dominate the reaction activity of both the OER and the ORR. To this end, for MnO_x families, a fundamental understanding of

correlations between the catalytic performance for OER and ORR and surface properties is urgently needed. As a prototype system, we herein choose to concentrate on a simple halite MnO with a face-centered cubic (*fcc*) structure to evaluate the effect of surface energy on catalytic activity for both OER and ORR. 3-D complex MnO nanoflowers and polypods with selectively oriented MnO crystals were prepared using a limited ligand protection method. Electrocatalytic measurements demonstrated that the catalytic activity of MnO nanocatalysts for both OER and ORR was highly dependent on exposed crystal planes. Our study highlights the correlation between OER/ORR activities and exposed crystal planes of manganosite catalysts and it may provide fundamental guidance for developing active and cost-effective electrocatalysts.

6.3 Experimental Section

6.3.1 Materials

The ultra-pure water was obtained and purified using High-Q, Inc. system with model 103S. Manganese(II) chloride tetrahydrate (>98%), cobalt(II) chloride hexahydrate (>99%), sodium hydroxide (95%), oleic acid (90%), 1-octadecene (90%) were purchased from Sigma-Aldrich and sodium oleate (>97%) were purchased from Fisher Scientific Inc. All chemicals were used without further purification unless otherwise noted.

6.3.2 Synthesis of $Mn(oleate)_2$ Precursors and Nanocrystals

6.3.2.1 Synthesis of $Mn(oleate)_2$

$Mn(oleate)_2$ was synthesized using a reported method with slight modification.[1] Briefly, in a 250 mL round-bottom flask, manganese(II) chloride tetrahydrate (50 mmol, 9.9 g), sodium oleate

(105 mmol, 32.0 g) was added to 180 mL of a mixed water/EtOH/hexane (5:4:9, vol) solvent. The mixture was refluxed overnight under strong stirring. After cooling down to room temperature, the reaction mixture was then washed with water and extracted with hexane. The orange waxy solid of $Mn(oleate)_2$ was obtained after dried under vacuum.

6.3.2.2 Synthesis of $Co(oleate)_2$

In a typical synthesis of $Co(oleate)_2$, cobalt(II) chloride hexahydrate (10 mmol, 2.4 g), oleic acid (20 mmol, 5.6 g) and NaOH (20 mmol, 0.8 g) were added to 63 mL of a mix water/EtOH/hexane (20:8:35) solvent in a 250 mL flask. The mixed solution was heated for 4 h at 80℃ and then cooled to room temperature. The reaction mixture was then washed with water and extracted with hexane. The deep purple waxy solid of $Co(oleate)_2$ was obtained after removal of solvent under vacuum.

6.3.2.3 Synthesis of MnO Nanoflowers and Different Morphologies

In a typical synthesis, $Mn(oleate)_2$ (2 mmol, 1.24 g) and 10 g of 1-ocdacene were placed in a 25 mL of three-necked flask equipped with a condenser. The reaction was heated by heating mantle with a temperature regulator. The reaction mixture was first heated at 80^{o}C and vacuum treated for 30 min to remove residual moisture. After refilled with argon, the reaction was further heated to 320^{o}C at a rate of 10^{o}C/min. The clear orange solution gradually turned to greenish suspension when reached 320^{o}C and the mixture was stirred at 320^{o}C for another 30 min. After cooling down to room temperature, the crude product was precipitated with an excess of acetone and collected by centrifugation. After washed for three time with hexane and acetone, the collected product was redispersed in hexane and stored. To synthesize MnO nanocrystals of polypods and octahedrons,

oleic acid (OA) was introduced as a free ligand. With various $Mn(oleate)_2$/OA molar ratios, the MnO polypods ($Mn(oleate)_2$/OA = 1:0.09), MnO polyhedra with short arms ($Mn(oleate)_2$/OA = 1:0.27), and MnO octahedra ($Mn(oleate)_2$/OA = 1:0.9) can be obtained.

6.3.2.4 Synthesis of MnO Nanocrystals with Co Dopants

To synthesize cation doped MnO nanocrystals, a similar procedure was used. A mixture of $Mn(oleate)_2$ (2 mmol, 1.24 g), $Co(oleate)_2$ with molar percentage of 5% and 10%, and 10 g of 1-ocdacene were placed in the flask. The reactions were heated at 80°C under vacuum for 30 minutes and heated to 320°C at a rate of 10°C/min with 30 minutes duration time at 320°C under Argon. After cooling down to room temperature, the crude product was precipitated with addition of acetone and collected by centrifugation.

6.3.3 Electrochemical Studies

Linear sweep voltammetry (LSV), electrochemical impedance spectroscopy (EIS), and chronoamperometry experiments were obtained with a CHI 660A electrochemical workstation. For electrochemical oxygen evolution reaction (OER) and oxygen reduction reaction (ORR) studies, pyrolytic graphite carbon working electrodes were used (surface area ~0.13 cm^2) equipped with a rotating disc working electrode (RDE) configuration. A carbon rod was used as a counter electrode and saturated calomel electrode (SCE) as the reference electrode. The potentials reported in this work are referenced to the reversible hydrogen electrode (RHE) and denoted as RHE potential. To prepare the working electrode, 4 mg of catalysts and 1 mg of carbon (VulcanXC-72) were dispersed in 1 mL of water/EtOH by sonication. 85 μL of Nafion solution was added to the above mixture and sonicated for another 20 min. 10 μL of solution was then dropped on the

working electrode surface and dried overnight before use. CV curves were *i*R-compensated and performed from 0.41 to 1.81 V (vs. RHE) with a sweep rate of 5 mV s^{-1} in oxygen saturated 0.1 M of KOH solution. The working electrode was rotated at 1600 rpm. The electrochemical impedance spectra were collected by applying an AC voltage with 5 mV amplitude in a frequency ranged from 0.1 to 10^5 Hz. To check fitting results, selected experimental data were also fitted using the ZSimDemo software package (version 3.2). In this procedure, RC initial estimates were obtained using a circle fitting function. Similar fitting parameters were obtained using both software packages.

The calculation methods of mass activity and TOF of electrochemical studies in this work is presented as following. Mass activity (A g^{-1}) values were obtained from deposited the catalytic materials on the working electrode (~0.03 mg) with measured current density (*j*, A cm^{-2}) at η = 0.35 V. Turnover frequency (TOF) values were obtained using the following equation and assuming all materials on the working electrode are involved in the reaction, using TOF= *j*S/4Fn, where *j* (A cm^{-2}) is the measured current density at η = 0.35 V, S (cm^2) represent the surface area of the working electrode, F (C mol^{-1}) is Faraday's constant, and n (mol) is the moles of the metal atom on the working electrode. The standard rate constant (K^0) can be obtained using the measured charge transfer resistance (R_{ct}) and calculated using the following formulas:

$$i_0 = \frac{R\,T}{n\,F\,R_{ct}} \qquad k^o = \frac{i_0}{n\,F\,C}$$

Where i_0 is the exchange current in A, R is the gas constant, T is the absolute temperature, n is the number of electrons transferred (assumed to be 4 in OER for all catalyst for comparison), F is Faraday's constant, C is the saturated concentration of oxygen in 0.1 M KOH.

Koutecky-Levich (K-L) plots were used to interpret the ORR results measured at different rotating speed. The number of electron transferred per one oxygen molecule (n) can be obtained from K-L plots by applying the following equations:

$$\frac{1}{J} = \frac{1}{J_L} + \frac{1}{J_K} = \frac{1}{B\omega^{1/2}} + \frac{1}{J_K}$$

$$B = 0.2nFC_0(D_0)^{2/3}\nu^{-1/6}$$

Where, J is the measured current density, J_K is the kinetic current, J_L is the diffusion limiting current, ω is the rotation speed of the electrode in rpm, B is the reciprocal of the slope of the K-L plots, F is Faraday constant (96485 C mol^{-1}), C_0 is the saturated concentration of oxygen in 0.1 M KOH (1.2×10^{-6} mol cm^{-3}), D_0 is the diffusion coefficient of O_2 (1.9×10^{-5} cm^2 s^{-1}), and υ is kinematic viscosity of the electrolyte ($0.01 cm^2$ s^{-1}).

6.3.4 Characterization

The crystallinity of as-synthesized materials was characterized using a Rigaku UltimaIV powder X-ray diffractometer (PXRD) with Cu K_α radiation and a tube voltage of 40 kV and current of 44 mA. The PXRD patterns were collected over a 2θ range of 5~75° with a continuous scan rate of 2.0° min^{-1}. Morphologies of catalysts were studied using high resolution transmission electron microscopy (HR-TEM). HRTEM studies were carried out using the JEOL 2010 transmission electron microscope with an accelerating voltage of 200 kV and the 2006 Tecnai T12 TEM/STEM equipped with EDAX EDS system. TEM samples were prepared by casting the suspension of material on a carbon coated copper grid (300 mesh). In addition, the elemental maps of the specimen were collected using a Gatan imaging filter detector. The image filtering was carried out using the O K-, Mn K- and Co L-edges at 532, 540 and 456 eV, respectively. The

structural model of interfacial features observed in the HRTEM images was established and analyzed using Crystalmaker software.

For the surface analysis, the X-ray photoelectron spectroscopy (XPS) was performed on a PHI model 590 spectrometer with multi-probes (Physical Electronics Industries Inc.), using Al K_α (λ = 1486.6 eV) as the radiation source. The powder samples were pressed on carbon tape mounted on adhesive copper tape stuck to a sample stage placed in the analysis chamber. The XPS spectra were analyzed and fitted using CasaXPS software (version 2.3.12). The C 1s photoelectron line at 284.6 eV was used as a reference for correction of the surface charging. A mixture of Gaussian (70%) and Lorentzian (30%) functions was used for the least-squares curve fitting procedure. The XAFS data were collected at the National Synchrotron Light Source (NSLS) at Brookhaven National Laboratory utilizing beam line X18A. A Silicon (111) double crystal monochromator was used to monochromatize the synchrotron radiation. The incident and transmitted beam intensities were monitored using ionization chambers filled with N_2. The samples were diluted by h-BN with a ratio of (1:8) then pressed into pellets and mounted in front of transmission detector. Before the measurements were taken, a thin Mn foil reference was used for energy calibration. The XANES data were analyzed using Athena software where background and post and pre-edge corrections were made.

6.3.5 Computational Detail

The first-principles computation is performed within the framework of density functional theory (DFT), using the projector augmented wave method as implemented in the Vienna *ab initio* simulation package. In present spin polarized calculations, the exchange correlation interaction is treated within the generalized gradient approximation (GGA) using the Perdew-Burke-Ernzerhoff

(PBE) functional. The electronic wave functions were expanded in a plane wave basis with a cut off energy of 400 eV. It is worth mentioning here that due to the errors associated with the on-site Coulomb and exchange interactions, DFT based methods are known to fail to reproduce an accurate description of the electronic structure for strongly correlated systems such as transition metal oxides and rare-earth compounds. In such cases, the accuracy of DFT can be improved by incorporating a Hubbard-model-type correction (U), which accounts for localized *d* and *f* orbitals. Hence, in the present work to describe the localized nature of the manganese *d* states, all the calculations are performed using U = 4 eV, which is well-optimized value particularly for MnO.

In case of bulk MnO, the relaxation of atomic positions and optimization of lattice parameters are performed by the conjugate gradient method. The atomic positions are relaxed until the maximum component of the force on each atom is smaller than 0.02 eV/Å. The Brillouin zone sampling was done using a Monkhorst-Pack mesh of 4 x 4 x 4, to achieve the convergence within 0.1 meV per formula unit. The optimized lattice parameter of the bulk MnO (4.51 Å) is slightly overestimated with respect to available experimental results (4.445Å). The overestimation of lattice parameters is also observed in earlier DFT based studies. The relative stability of MnO(100), MnO(110), and MnO(111) surfaces is calculated using 9, 9, and11-layer slabs respectively separated by a vacuum spacing of 12 Å . During geometry relaxation a Γ-centered 5 x 5 x 1 k-point mesh was considered.

The surface energy (γ) for a symmetric slab is given by:

$$\text{Surface energy } (\gamma) = (E_{slab} - n \times E_{MnO\ Bulk}) / 2A$$

where, γ is the surface energy, E_{slab} and $E_{MnO\ Bulk}$ are the total energy of the surface and bulk MnO respectively, n is the number of MnO formula units and A is the area of the two-dimensional unit cell. The factor 2 takes into account symmetric nature of the slab used in the present work.

To fully exploit the nature of above mention surfaces, we also study the interaction between the surfaces and the spices from the surrounding environment such as gas-phase oxygen (both neutral atomic and molecular oxygen) and OH on different facet of MnO surfaces. Here, for each surface facet we determine exact orientation and preferential adsorption site for O, O_2 and OH using our DFT energetics. The adsorption energy E_{ad} is the energy of the fully relaxed surface with the adsorbate minus the sum of energies of the isolated relaxed surface and isolated adsorbate.

6.4 Results and Discussion

MnO nanoflowers and polypods were synthesized by using thermal decomposition of $Mn(oleate)_2$ in a non-coordinating, apolar hydrocarbon solvent.[7] Briefly, 1.24 g of $Mn(oleate)_2$ was dissolved in 10 g of octadecene in a 25 mL three-neck round-bottom flask. The mixture was first degassed at 80^{o}C under vacuum for 30 min and then heated to 320 ^{o}C at a rate of 10 ^{o}C/min under argon. After stirring for another 30 min, the reaction mixture was cooled and then precipitated with an excess of acetone. The obtained nanoparticles (NPs) were first characterized by transmission electron microscopy (TEM). As shown in the low-magnification TEM image (**Figure 6.1a**), the nanoflowers are composed of a spherical core decorated by densely packed well-defined MnO nanorods. The as-synthesized MnO nanoflowers are quasi-spherical and have an average diameter of 126.5±17.6 nm. These nanorods are nearly single crystalline MnO (see below) and have a length of 40~50 nm and a diameter of ~15 nm. High-resolution TEM analysis showed the manganosite crystalline structure of MnO with *d*-spacings of 0.22 nm and 0.32 nm that

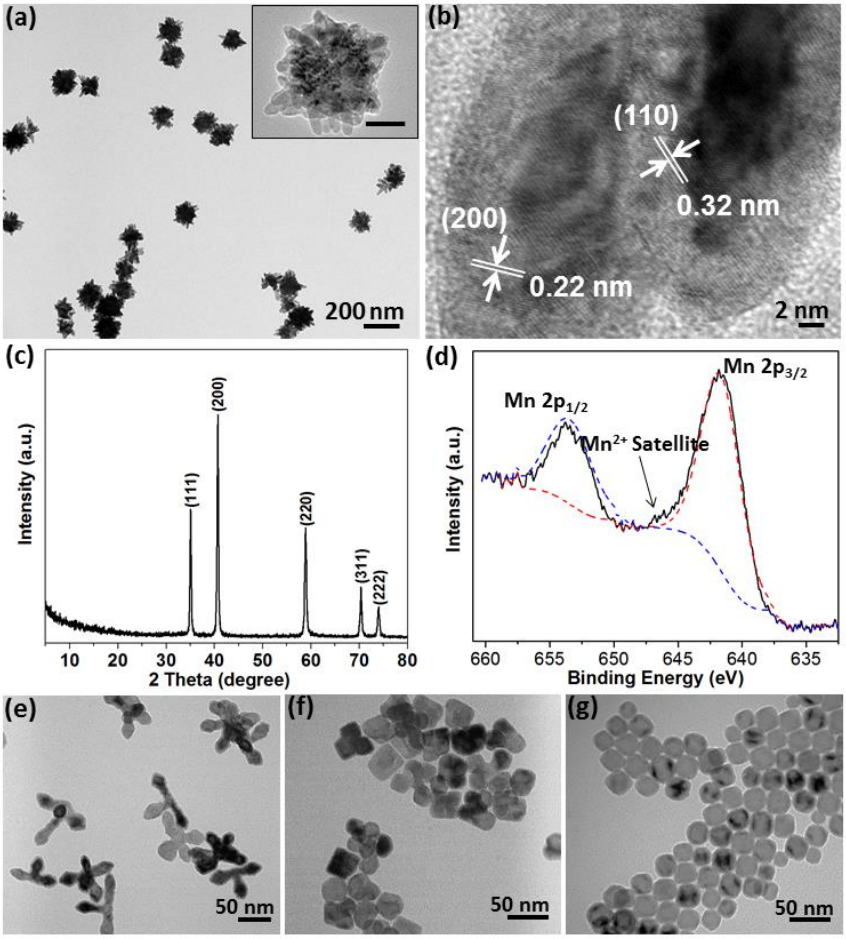

Figure 6.1 (a,b) TEM images of MnO nanoflowers. The inset in (a) is a zoom-in view of a single nanoflower. (c) The powder XRD pattern of MnO nanoflowers. (d) Mn 2p XPS spectrum of MnO nanoflowers. (e-g) TEM images of MnO nanocrystals obtained at different $Mn(oleate)_2$/OA molar ratios: (e) 1:0.09; (f) 1:0.27; (g) 1:0.9.

correspond to (200) and (110) planes (**Figure 6.1b**), in good agreement with the powder X-ray diffraction (XRD) pattern in **Figure 6.1c**. The deconvolution of X-ray photoelectron spectroscopy (XPS) data (**Figure 6.1d**) shows the binding energy of Mn $2p_{1/2}$ (653.4 eV) and Mn $2p_{3/2}$ (641.6 eV) falls in the Mn 2p region.[5a] The co-existence of a satellite peak at 646 eV suggests the presence of Mn^{2+} species on the surface of the nanoflowers. X-ray absorption near-edge spectra also confirmed the average Mn oxidation state of 2.02. No significant amount of Mn species with higher oxidation state was detected for months.

The oriented attachment of 1D nanorods to nanoflowers, *e.g.* the number and length of 1D nanorods, appeared to be highly controllable using oleic acid (OA) as a free ligand. These results are summarized in **Figures 6.1e-g**. At a low concentration of OA ($Mn(oleate)_2$/OA=1:0.09, mol/mol, M/O ratio hereafter), the formation of MnO polypods was observed (**Figure 6.1e**). These polypods essentially retained the 3-D complex architectures of nanoflowers but had far fewer branches. Of them, MnO tetrapods composed of four nanorod branches were the dominant product. Compared to MnO nanoflowers, the length and diameter of nanorods in MnO polypods did not change significantly. With increase of M/O ratio to 1:0.27 (mol/mol), irregular polyhedra with surface protuberances were obtained where MnO nanorods were significantly shortened (**Figure 6.1f**). The average size of MnO polyhedra decreased to ~32 nm. By further increasing the M/O ratio to 1:0.9 (mol/mol), the complex surface structures disappeared and nearly mono-disperse MnO octahedral nanocrystals were obtained with a diameter of ~19 nm (**Figure 6.1g**).

The growth of MnO 3-D complex nanocrystals was likely due to the limited ligand supply.[7a] Without the presence of OA free ligands, the initially formed MnO seeds were not covered by OA ligands; thus, the growth of MnO nanocrystals was nucleated on the exposed surface of MnO seeds. Limited ligand protection would lead to the formation of nanoflowers with oriented nanorods. In the presence of a low concentration of OA ligands (<20 mol%), the OA would partially cover the surface of MnO seeds. The less exposed surface resulted in the formation of MnO polypods with much less branched nanostructures. With the addition of 1: 0.9 equivalence of OA ligands, the (111) planes of MnO seeds were preferentially bonded with OA ligands thus leading to the formation of octahedral MnO nanocrystals.

To gain more insight into the crystallographic structure and growth mechanism of MnO nanocrystals, high resolution TEM characterization with selected area electron diffraction (SAED)

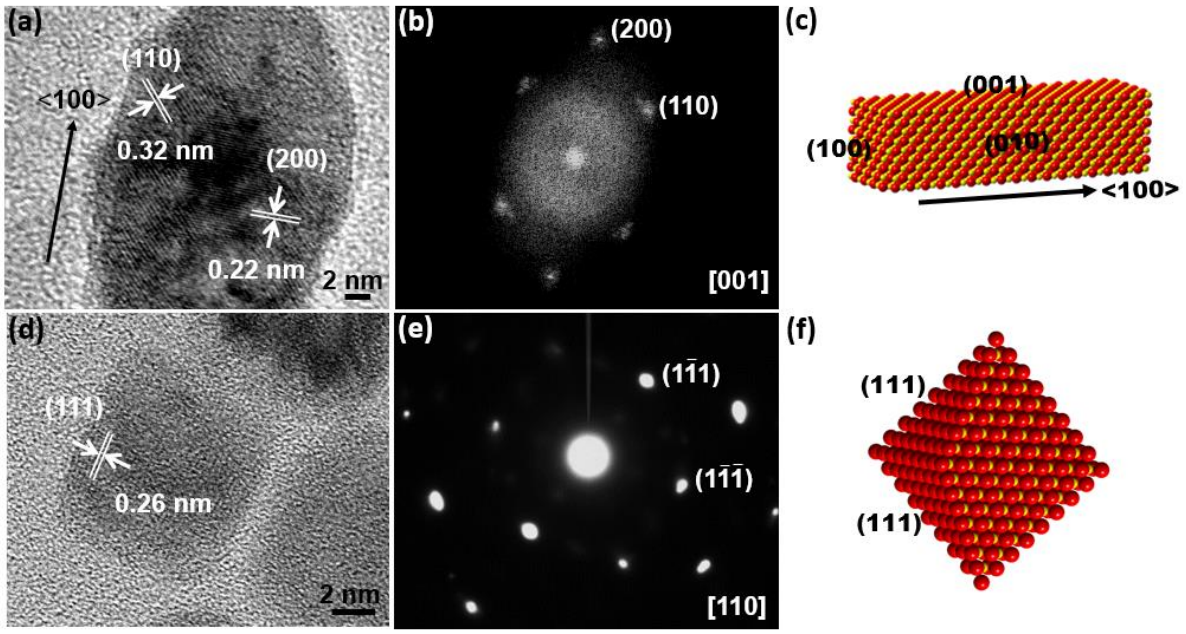

Figure 6.2 (a,b) The high-resolution TEM image of a single rod of MnO polypods (a) and the corresponded SAED pattern (b). (c) The schematic illustration indicating the growth direction and exposed planes of MnO nanorods on MnO polypods. (d,e) The high-resolution TEM image of a single MnO octahedral NP (d) and the corresponding SAED pattern (e). (f) The schematic illustration indicating the growth direction of MnO octahedral NPs. O is red and Mn is yellow.

studies were further performed. The results of surface planes of MnO nanocrystals are intriguing. The TEM image of a single nanorod on MnO polypods (**Figure 6.2a**) shows the (200) and (110) planes with an interfacial angle of 45°. The SAED pattern of nanorods can be indexed to the manganosite *fcc* structure with the <100> zone axis parallel to (001) and (010) planes (**Figure 6.2b**). MnO polypods exposed (100), (001), and (010) planes on their branches (**Figure 6.2c**). These results further support the growth mechanism as aforementioned. The free OA ligands have a favorable interaction with (111) planes with a slightly larger surface energy, resulting in the anisotropic growth of MnO nanocrystals. For MnO octahedral NPs, the corresponding SAED

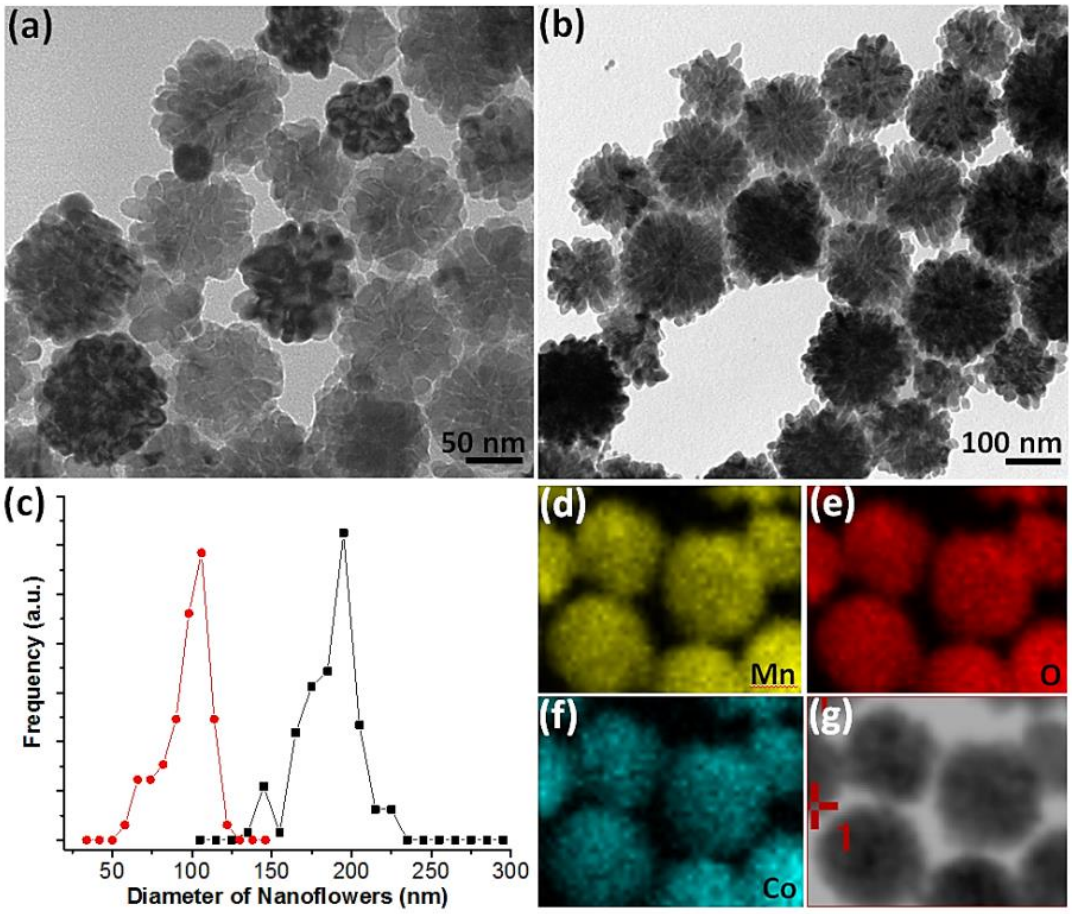

Figure 6.3 (a,b) TEM images of 5 mol% (a) and 10 mol% (b) Co doped MnO nanoflowers. (c) Size distribution of Co doped MnO nanoflowers, 5 mol% Co (red) and 10 mol% Co (black). (d-g) TEM energy-dispersive X-ray (EDX) elemental mapping of 10 mol% Co doped MnO nanoflowers and the corresponded TEM image (g). The molar ratio of Co/Mn from EDX mapping is 1:12. Yellow, red and cyan colors indicate the Mn-rich, O-rich and Co-rich domains, respectively.

pattern (**Figure 6.2e**) can be indexed as the <110> zone axis of the MnO *fcc* structure. Only (111) planes are exposed for octahedral NPs. This is similar to previously reported FeO and CuO octahedral NPs.[8]

In addition to pure MnO nanocrystals, other transition metal cations, *e.g.* Co^{2+}, can be doped into the complex nanostructure of MnO by mixing metal oleate precursors. TEM images of Co-doped MnO nanoflowers with Co/Mn molar ratios of 5% and 10% were given in **Figure 6.3**. The

3-D topological architectures of nanoflowers did not significantly change with the doping amount of Co cations. With 5% of Co, the diameter of Mn-Co nanoflowers was 95.8±14.2 nm (**Figure 6.3c**) and nanorods appeared to pack more densely on the surface; while further increase of the Co/Mn molar ratio to 10% would lead to the increase of their average size to 186.2±18.1 nm. Energy-dispersive X-ray elemental mapping confirmed the uniform distribution of Mn and Co elements in nanoflowers (**Figures 6.3d~g**). No change in the MnO crystalline structures was observed from XRD after doping.

MnO nanocrystals were further evaluated as bifunctional catalysts for the OER and ORR using rotating-disk electrode techniques. **Figure 6.4a** presents the typical linear sweep voltammograms (LSVs) of MnO nanocrystals for OERs in KOH solution (0.1 M) with a sweep rate of 5 mV s^{-1}. MnO polypods with exposed (100) planes showed a superior activity with an overpotential (η) of 0.58 V at a current density (j) of 10 mA cm^{-2}, much lower than that of other MnO nanocrystals. At η=0.35 V, the mass activity for MnO polypods catalyst was found to be 17.75 A g^{-1}. The turnover frequency (TOF) of MnO polypods reached 4.19×10^{-4} s^{-1} (see **Table 6.1**), comparable with the reported best values of MnO_x polymorphs.[5a,f,8a,9] MnO octahedra with (111) dominated surface exhibited a much lower activity and current densities, nearly overlapped with that of commercial MnO catalysts. MnO nanoflowers with multi-exposed planes displayed a moderate catalytic activity with a TOF of 1.32×10^{-4} s^{-1}. Tafel plots derived from LSV curves are given in **Figure 6.4b**. Tafel slopes of MnO polypods and nanoflowers are 149 and 169 mV/dec, respectively. The lower Tafel slopes indicate that the OER of polypods and nanoflowers is kinetically more

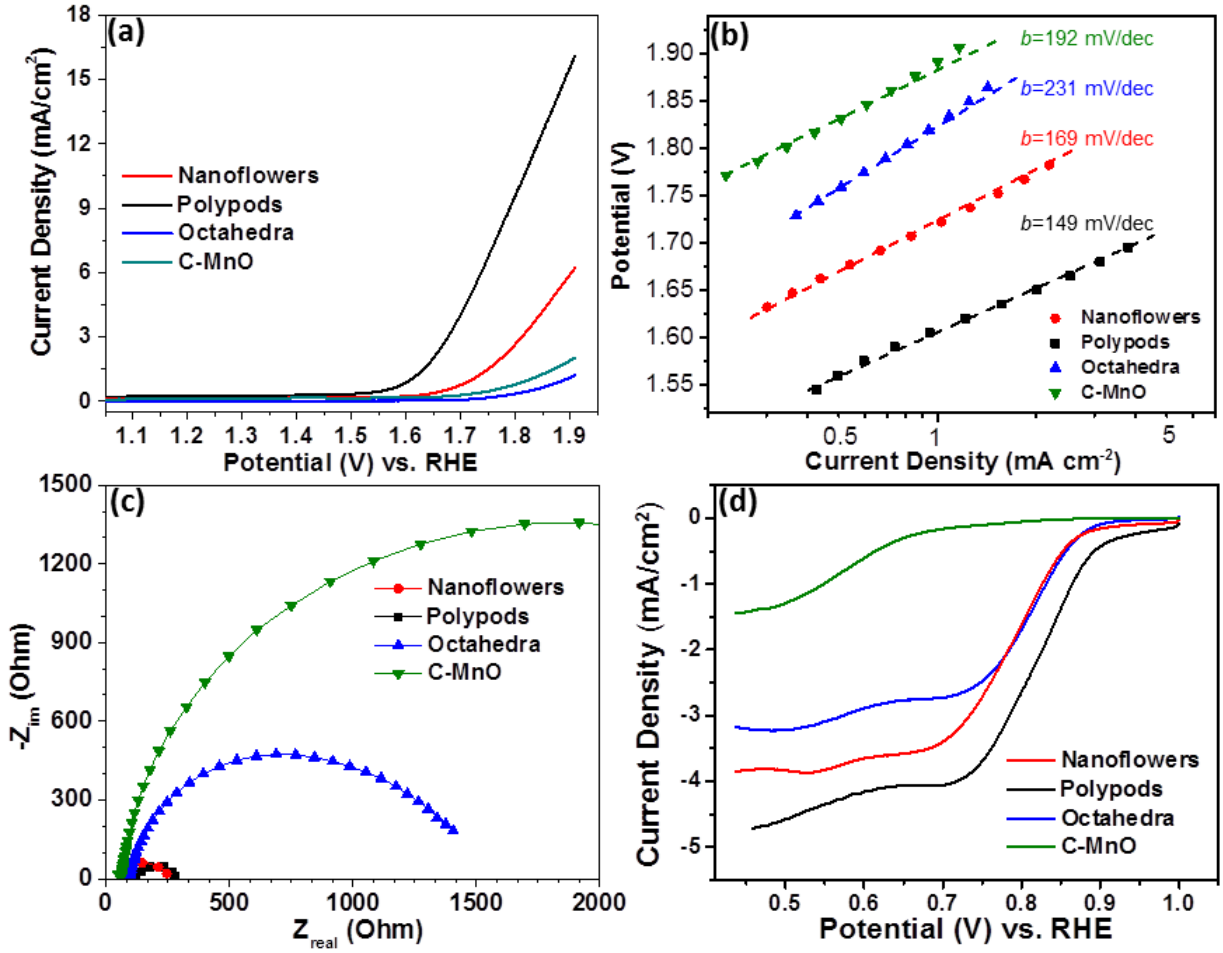

Figure 6.4 (a) Linear sweep voltammetry (LSV) curves of MnO nanocatalysts for electrochemical OERs at a scan rate of 5 mV s^{-1} in 0.1 M of KOH. C-MnO is commercialized MnO. (b) The corresponded Tafel plots of MnO nanocatalysts in (a). (c) The Nyquist plots obtained from the electrochemical impedance spectroscopy measurements at 1.76 V *vs*. RHE and a frequency range of 0.1 to 10^5 Hz. (d) Linear sweep voltammetry (LSV) curves for ORRs in 0.1 M of KOH solution.

favorable compared to that of octahedra. **Figure 6.4c** shows the Nyquist plot of the electrochemical impedance spectra (EIS) of MnO nanocrystals. The charge-transfer resistance value is inversely proportional to the electron transfer rate. MnO polypods and nanoflowers have R_{ct} of 256 and 275 Ω, respectively, lower than that of MnO octahedra and commercial MnO. This result is in good agreement with their OER activities.

Table 6.1 Summarized OER and ORR activities of MnO catalysts.

Catalysts	Oxygen Evolution Reaction					Oxygen Reduction Reaction	
	η at J = 10 mA cm^{-2} (V)[a]	Mass activity at η =0.35 V (A g^{-1})[b]	Resistance R_{ct} (Ω)[c]	TOF at η =0.35 V (s^{-1})[d]	k^o (cm s^{-1}) [e]	E_j at J = -3 mA cm^{-2} (V)[f]	$E_{1/2}$ / E_{onset} (V)[g]
Nanoflowers	-	5.60	275	1.32×10^{-4}	0.0016	0.73	0.77/0.91
Polypods	0.58	17.75	256	4.19×10^{-4}	0.0017	0.78	0.81/0.87
Octahedra	-	4.34	1406	1.02×10^{-4}	0.0003	0.57	0.61/0.88
C-MnO	-	0.52	3595	1.22×10^{-5}	0.0001	-	0.59/0.65
10% Co-MnO	0.64	22.16	196	5.23×10^{-4}	0.0022	0.73	0.79/0.88
5% Co-MnO	0.64	17.65	266	4.16×10^{-4}	0.0016	0.71	0.78/0.88

All data in the tables are extracted from the LSV and EIS experiments in 0.1 M KOH at a rotation speed of 1600 rpm vs RHE. [a] Overpotential measured from LSV at a current density of 10 mA/cm^2. [b] Mass activity calculated from LSV at overpotential at 0.35 V. [C] The charge transfer resistance (R_{ct}) obtained from EIS analysis at 1.76 V vs RHE. [d] The turnover number calculated from LSV at overpotential at 0.35 V. [e] The standard rate constant calculated from R_{ct} values. [f] The potential obtained at a current density of -3 mA/cm^2. [g] The half-way potential and onset potential obtained from LSV.

ORR activity of MnO nanocrystals was also examined by cyclic voltammetry (CV) in 0.1 M of KOH solution. In argon-saturated solution, the voltammogram without an obvious peak was observed; while, a well-defined cathodic oxygen reduction peak with a high current density appeared when the electrolyte was saturated with O_2, indicating MnO nanocrystals are electrocatalytically active for the ORR. The ORR catalytic results of MnO nanocrystals are given in **Figure 6.4d**. MnO polypods, again, displayed a superior activity with a half-wave potential of 0.77 V, only 80 mV lower than that of Pt/C catalysts.[5f] The diffusion-limiting current of MnO polypods reaches ~5.0 mA cm^{-2}, higher than MnO nanoflowers with 3.8 mA cm^{-2} and octahedra with 3.1 mA cm^{-2}, indicating that the preferentially exposed (100) planes indeed improved the

Table 6.2 DFT (GGA+U) based calculated surface energy (**γ**) and adsorption (Ead) and binding distances (BD) for (100), (110) and (111) surface of MnO.

	MnO (100)		**MnO (110)**		**MnO (111)**	
Surface energy (meV/ Å ^{2})	60		110		170	
Adsorbate	E_{ad} (eV)	BD (Å)	E_{ad} (eV)	BD (Å)	E_{ad} (eV)	BD (Å)
O*	-2.950	1.60	-0.446	1.79	-0.018	1.97
O_2	-2.619	1.65	-0.725	1.84	-0.298	2.12
OH*	-2.998	1.71	-3.428	1.96	-1.868	2.16

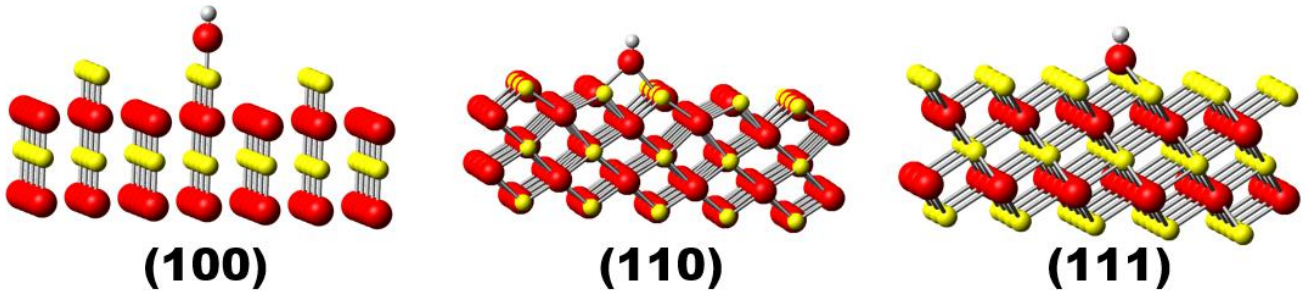

The representative of OH* adsorbate species on different MnO lattice surfaces. H is in white, O is in red, and Mn is in yellow.

ORR activity as well. As compared to other reported MnO_x catalysts for ORRs, *e.g.* MnO_x film reported by Gorlin *et al.* with a potential of 0.73 V[5f] and α-MnO_2 reported by Meng *et al*. with a potential of 0.76 V at J=-3 mA cm^{-2},[5a] MnO polypods have some of the lowest overpotentials for the ORR. The stability of MnO ploypods for the ORR was also studied by current-time (*i-t*) chronoamperometric response at a potential of 0.66 V (*vs.* RHE). MnO ploypods maintained 80% of its original activity after an hour. Furthermore, the overall oxygen electrode activity (ΔE=E_{OER}-E_{ORR}) is as low as 1.02 V, smaller than that of Ir/C and Pt/C,[3,4,5f] suggesting MnO polypods as a superior bifunctional electrocatalyst for OER/ORR.

For MnO (100) and (111) crystal planes, the (100) planes with mixed Mn^{2+} and O^{2-} ions have a lower surface energy; while, the (111) planes are polar surfaces consisting of alternating layers of Mn^{2+} and O^{2-} ions generating an electrostatic dipole field perpendicular to the surface. To gain further insight into the correlation between OER/ORR activities and the exposed crystal planes of the MnO nanocrystals, adsorption energies of O species, *e.g.* OH^- and O_2 have been estimated for different MnO crystal planes (**Table 6.2**) using density functional theory. The adsorption of O species is known as a rate-determining step for ORRs/OERs.[10] In comparison with (111) planes, the MnO (100) planes are highly exothermic for OH^- and O_2 adsorption. The large exothermic interaction may also be understood in terms of the unsaturated coordination on MnO (100) planes.

6.5 Conclusions

In summary, 3-D complex anisotropic MnO nanocrystals were demonstrated as superior bifunctional electrocatalysts. Their electrocatalytic activity for OERs/ORRs was strongly correlated with exposed lattice facets of MnO nanocrystals. The MnO (100) planes with higher adsorption energy of O species could largely promote the electrocatalytic activity for the OER and the ORR. Our results may illustrate a new paradigm for developing highly active and cost-effective electrocatalysts.

6.6 References

(1) (a) Voiry, D.; Yamaguchi, H.; Li, J.; Silva, R.; Alves, D. C. B.; Fujita, T.; Chen, M.; Asefa, T.; Shenoy, V. B.; Eda, G.; Chhowalla, M. *Nat. Mater.* **2013**, *12*, 850. (b) Ji, X.; Lee, K. T.; Holden, R.; Zhang, L.; Zhang, J.; Botton, G. A.; Couillard, M.; Nazar, L. F. *Nat. Chem.* **2010**, *2*, 286. (c) Liang, Y.; Li, Y.; Wang, H.; Zhou, J.; Wang, J.; Regier, T.; Dai, H. *Nat. Mater.* **2011**, *10*, 780.

(2) (a) Bing, Y.; Liu, H.; Zhang, L.; Ghosh, D.; Zhang, J. *Chem. Soc. Rev.* **2010**, *39*, 2184. (b) Zhang, H.; Jin, M.; Xia, Y. *Chem. Soc. Rev.* **2012**, *41*, 8035. (c) Guo, S.; Zhang, S.; Sun, S. *Angew. Chem. Int. Ed.* **2013**, *52*, 8526. (d) Guo, S.; Zhang, X.; Zhu, W.; He, K.; Su, D.; Mendoza-Garcia, A.; Ho, S. F.; Lu, G.; Sun, S. *J. Am. Chem. Soc.* **2014**, *136*, 15026.

(3) (a) Koenigsmann, C.; Santulli, A. C.; Gong, K.; Vukmirovic, M. B.; Zhou, W.-p.; Sutter, E.; Wong, S. S.; Adzic, R. R. *J. Am. Chem. Soc.* **2011**, *133*, 9783. (b) Zhang, S.; Zhang, X.; Jiang, G.; Zhu, H.; Guo, S.; Su, D.; Lu, G.; Sun, S. *J. Am. Chem. Soc.* **2014**, *136*, 7734. (c) Strasser, P.; Koh, S.; Anniyev, T.; Greeley, J.; More, K.; Yu, C.; Liu, Z.; Kaya, S.; Nordlund, D.; Ogasawara, H.; Toney, M. F.; Nilsson, A. *Nat. Chem.* **2010**, *2*, 454.

(4) Reier, T.; Oezaslan, M.; Strasser, P. *ACS Catal.* **2012**, *2*, 1765.

(5) (a) Meng, Y.; Song, W.; Huang, H.; Ren, Z.; Chen, S.-Y.; Suib, S. L. *J. Am. Chem. Soc.* **2014**, *136*, 11452. (b) Indra, A.; Menezes, P. W.; Zaharieva, I.; Baktash, E.; Pfrommer, J.; Schwarze, M.; Dau, H.; Driess, M. *Angew. Chem. Int. Ed.* **2013**, *52*, 13206. (c) Najafpour, M. M.; Ehrenberg, T.; Wiechen, M.; Kurz, P. *Angew. Chem. Int. Ed.* **2010**, *49*, 2233. (d) Boppana, V. B. R.; Jiao, F. *Chem. Commun.* **2011**, *47*, 8973. (e) Iyer, A.; Del-Pilar, J.; King'ondu, C. K.; Kissel, E.; Garces, H. F.; Huang, H.; El-Sawy, A. M.; Dutta, P. K.; Suib, S. L. *J. Phys. Chem. C* **2012**, *116*, 6474. (f) Gorlin, Y.; Jaramillo, T. F. *J. Am. Chem. Soc.* **2010**, *132*, 13612. (g) Kuo, C. H.; Li, W.; Pahalagedara, L.; El-Sawy, A. M.; Kriz, D.; Genz, N.; Guild, C.; Ressler, T.; Suib, S. L.; He, J. *Angew. Chem. Int. Ed.* **2015,** *54*, 2345. (h) Huynh, M.; Bediako, D. K.; Nocera, D. G. *J. Am. Chem. Soc.* **2014**, *136*, 6002. (i) Jiao, F.; Frei, H. *Chem. Commun.* **2010**, *46*, 2920.

(6) Suib, S. L. *Acc. Chem. Res.* **2008**, *41*, 479.

(7) (a) Narayanaswamy, A.; Xu, H.; Pradhan, N.; Peng, X. *Angew. Chem. Int. Ed.* **2006**, *45*, 5361. (b) Ould-Ely, T.; Prieto-Centurion, D.; Kumar, A.; Guo, W.; Knowles, W. V.; Asokan, S.; Wong, M. S.; Rusakova, I.; Lüttge, A.; Whitmire, K. H. *Chem. Mater.* **2006**, *18*, 1821. (c) Zitoun, D.; Pinna, N.; Frolet, N.; Belin, C. *J. Am. Chem. Soc.* **2005**, *127*, 15034.

(8) (a) Kim, D.; Lee, N.; Park, M.; Kim, B. H.; An, K.; Hyeon, T. *J. Am. Chem. Soc.* **2008**, *131*, 454. (b) Cheon, J.; Kang, N.-J.; Lee, S.-M.; Lee, J.-H.; Yoon, J.-H.; Oh, S. J. *J. Am. Chem. Soc.* **2004**, *126*, 1950. (c) Liang, X.; Gao, L.; Yang, S.; Sun, J. *Adv. Mater.* **2009**, *21*, 2068.

(9) Zaharieva, I.; Chernev, P.; Risch, M.; Klingan, K.; Kohlhoff, M.; Fischer, A.; Dau, H. *Energy Environ. Sci.* **2012**, *5*, 7081.

(10) (a) Lima, F. H. B.; Calegaro, M. L.; Ticianelli, E. A. *Electrochim. Acta* **2007**, *52*, 3732. (b) Mao, L.; Zhang, D.; Sotomura, T.; Nakatsu, K.; Koshiba, N.; Ohsaka, T. *Electrochim. Acta* **2003**, *48*, 1015.

Chapter 7. Future Perspectives and Directions.

The field of catalysis has a long history, however there is still much more to contribute. In fact, with incorporation of the new nanotechnologies briefly discussed in this thesis, heterogeneous catalysis has the potential to impact many modern industrial processes that were not previously accessible. However, such factors as cost, large-scale production, and reproducibility are still among the main problems that we need to overcome in nanomaterial synthetic techniques. One can imagine that expansion of the range of catalytic applications to industrial processes will move forward, and thus relies on our ability to develop new effective and selective catalysts.

In the work on CO oxidation with Co_3O_4@CNT, hydrophobic inorganic metal oxide (such as cerium oxide) might be used to replace the polymer-based coating layer in order to achieve higher thermal stability of the catalyst. The synthetic method of creating metal oxide nanoparticles on carbon nanotubes can also potentially be applied to other types of metal oxide materials. This may open up new possibilities in developing inexpensive and active metal oxide based composites for different applications. In the work on biomass reaction with acidic TiO_2 nanoparticles, the combination of several catalytic reactions using a single catalyst will be the next possible step in the research. Synthesis of a multi-functional catalytic system combining solid acids for dehydration/rehydration with noble metal/metal alloy for hydrogenation can eliminate the current catalytic process for obtaining versitle platform products from raw biomass resources. Additionally, incroporation of mix-metal oxides such as Zn, Ni, Sn with TiO_2 can possibly adjust the nature of the acid site in order to obtain different products.

In the work on water splitting with manganese oxide based catalysts, several specific goals can be pursued considering the current limitations and understanding of these transition

metal oxide based catalysts. These goals are the following: **(1)** Identify the active site of the manganese oxide catalyst, potentially providing fundamental guidance for developing active and cost-effective electrocatalysts. **(2)** Build up a protocol for material characterization to examine the synthesized catalyst for activity prediction. **(3)** Minimize the time and the number of experiments necessary to explore a new catalytic system. **(4)** Design an overall water splitting catalyst using nonprecious catalysts with various valence state metals. The first three approaches are aimed at finding correlation between the structure and the activity using known manganese based materials. The purpose is to investigate the structural transformations of the manganese oxide catalysts during the water splitting reaction. The structure of manganese oxides can be studied with several different techniques using X-ray powder diffraction (XRD), X-ray absorption fine structure (XANES) and extended X-Ray absorption fine structure (EXAFS) spectroscopy. Conclusions on structure-activity relationships can be made using a combination of structural information at the atomic scale as well as comprehensive catalytic behavior of manganese oxide catalysts with different structures. For exploring overall water splitting catalysts, synthesis of mesoporous cobalt and nickel mix-metal oxide catalysts can be used in the future. With the low hydrogen binding energy of nickel oxide and better OER activity of cobalt oxide, the proposed catalytic system will exhibit bifunctional catalytic efficiency for HER and OER. Finally, tuning of the catalytic behavior can also be performed by adjusting the cobalt/nickel ratio during material synthesis.

Appendix

List of Publications, Book Chapters, Patent Applications, Presentations, and Posters.

1. **Journal Articles:**

- **Kuo, C-H**, Mosa, I., Thanneeru, S., Sharma, V., Zhang, L., Biswas, S., Anidow, M., Alpay, S. P., Rusling, J. F., Suib, S. L., He, J. "Facet- Dependent Catalytic Activity of MnO Electrocatalysts for Oxygen Reduction and Oxygen Evolution Reactions" *Chem. Commun.* **2015**, *51*, 5951-5954.
- **Kuo, C-H**, Mosa, I., Poyraz, A. S., Biswas, S., El-Sawy, A. M., Song, W., Luo, Z., Chen, S.-Y., Rusling, J. F., He, J., Suib, S. L. "Robust Mesoporous Manganese Oxide Catalysts for Water Oxidation" *ACS Catalysis* **2015**, *5*, 1693-1699.
- Wasalathanthri, N. D., Poyraz, A. S., Biswas, S., Meng, Y., **Kuo, C-H**, Kriz, D. A., Suib, S. L. "High-Performance Catalytic CH_4 Oxidation at Low Temperatures: Inverse Micelle Synthesis of Amorphous Mesoporous Manganese Oxides and Mild Transformation to K_2-xMn_8O_{16} and ε-MnO_2" *J. Phys. Chem. C* **2015**, *119*, 1473-1482.
- Luo, Z., Poyraz, A. S., **Kuo, C-H**, Miao, R., Meng, Y., Chen, S.-Y., Jiang, T., Wenos, C., Suib, S. L. "Crystalline Mixed Phase (Anatase/Rutile) Mesoporous Titanium Dioxides for Visible Light Photocatalytic Activity" *Chem. Mater.* **2015**, *27*, 6-17.
- Njagi, E. C., Genuino, H. C., **Kuo, C-H**, Dharmarathna, S., Gudz, A., Suib, S. L. "High-yield selective conversion of carbohydrates to methyl levulinate using mesoporous sulfated titania-based catalysts" *Microporous Mesoporous Mater.* **2015**, *202*, 68-72.
- Li, W., Kanyo, I., **Kuo, C-H**, Thanneeru, S., He, J. "pH-programmable self-assembly of plasmonic nanoparticles: hydrophobic interaction verse electrostatic repulsion" *Nanoscale* **2014**, *7*, 956-964.
- Pahalagedara, L. R., Poyraz, A. S., Song, W., **Kuo, C-H**, Pahalagedara, M. N., Meng, Y., Suib, S. L. "Low temperature Desulfurization of H_2S: High sorption capacities by mesoporous cobalt oxide via increased H_2S diffusion" *Chem. Mater.* **2014**, *26*, 6613-6621.
- Biswas, S., Poyraz, A. S., Meng, Y., **Kuo, C-H**, Guild, C., Tripp, H., Suib, S. L. "Ion Induced Promotion of Activity Enhancement of Mesoporous Manganese Oxides for Aerobic Oxidation Reactions" *Applied Catalysis B: Environmental* **2015**, *126*, 731-741.

- El-Sawy, A. M., King'ondu, C. K., **Kuo, C-H**, Kriz, D. A., Guild, C., Meng, Y., Frueh, S. J., Dharmarathna, S., Ehrlich, S. N., Suib, S. L. "An X-ray Absorption Spectroscopic Study of a Highly Thermally Stable Manganese Oxide Octahedral Molecular Sieve (OMS-2) with High Oxygen Reduction Reaction Activity" *Chem. Mater.* **2014**, *26*, 5752-5760.
- **Kuo, C-H**, Li, W., Pahalagedara, L., El-Sawy, A. M., Kriz, D., Genz, N., Ressler, T., Suib, S. L., He, J. "Understanding the role of gold nanoparticles to enhance catalytic activity of manganese oxide for water oxidation reactions" *Angew. Chem. Int. Ed.* **2015**, *54*, 2345-2350.
- Li, W., **Kuo, C-H**, Kanyo, I., Thanneeru, S., He, J. "Synthesis and Self-Assembly of Amphiphilic Hybrid Nano Building Blocks via Self-Collapse of Polymer Single Chains" *Macromolecules* **2014**, *47*, 5932-5941.
- L. R. Pahalagedara, S. Dharmarathna, C. K. King'ondu, M. N. Pahalagedara, Y-T. Meng, **Kuo, C-H**, S. L. Suib "Microwave-Assisted Hydrothermal Synthesis of α-MnO_2: Lattice Expansion via Rapid Temperature Ramping and Framework Substitution" *J. Phys. Chem. C* **2014**, *118*, 20363-20373.
- Pahalagedara, M. N., Pahalagedara, L. R., **Kuo, C-H**, Dharmarathna, S., Suib, S. L. "Ordered Mesoporous Mixed Metal Oxides: Remarkable Effect of Pore Size on Catalytic Activity" *Langmuir* **2014**, *30*, 8228-8237.
- Pahalagedara, M. N., Samaraweera, M., Dharmarathna, S., **Kuo, C-H**, Pahalagedara, L. R., Gascón, J. A., Suib, S. L. "Removal of Azo Dyes: Intercalation into Sonochemically Synthesized NiAl Layered Double Hydroxide" *J. Phys. Chem. C* **2014**, *118*, 17801-17809
- **Kuo, C-H**, Li, W., He, J., Suib, S. L. "Facile synthesis of Co_3O_4@CNT with high catalytic activity for CO oxidation" *ACS Appl. Mater. Interfaces.* **2014**, *6*, 11311-11317.
- Poyraz, A. S., **Kuo, C-H**, Kim, E., Meng, Y., Islam, S., Suib, S. L. "Tungsten Promoted Mesoporous Group IV Transition Metal Oxides for Room Temperature, Solvent Free Acetalization and Ketalization Reactions" *Chem. Mater.* **2014**, *26*, 2803-2813.
- Poyraz, A. S., Hines, W. A., **Kuo, C-H**, Li, N., Perry, D. M., Suib, S. L. "Mesoporous Co_3O_4 Nanostructured Material Synthesized by One-Step Soft-Templating: A Magnetic Study" *J. Appl. Phys.* **2014**, *115*, 114309.

- **Kuo, C-H**, Poyraz, A. S., Jin, L, Meng, Y., Pahalagedara, L., Chen, S-Y, Kriz, D. A., Guild, C., Suib, S. L. "Heterogeneous Acidic TiO_2 Nanoparticles for Efficient Conversion of Biomass Derived Carbohydrates" *Green Chem.* **2014**, *16*, 785-791.
- Poyraz, A. S., **Kuo, C-H**, Biswas, S., Cecil K. King'ondu, C. K., Suib, S. L. "A general approach to crystalline and monomodal pore size mesoporous materials" *Nature Communications* **2013**, *4*, 2952.
- Meng, Y., Genuino, H. C. , **Kuo, C.-H.**, Huang, H., Chen, S.-Y., Zhang, L., Rossi, A. R., Suib, S. L. "One-Step Hydrothermal Synthesis of Manganese-Containing MFI-Type Zeolite, Mn-ZSM-5, Characterization, and Catalytic Oxidation of Hydrocarbons." *J. Am. Chem. Soc.* **2013**, *135*, 8594-8605.
- Genuino, H. C., Meng, Y., Horvath, D. T., **Kuo, C.-H.**, Seraji, M. S., Morey, A. M., Joesten, R. L. and Suib, S. L., "Enhancement of Catalytic Activities of Octahedral Molecular Sieve Manganese Oxide for Total and Preferential CO Oxidation through Vanadium Ion Framework Substitution," *ChemCatChem* **2013**, *5*, 2306-2317.
- Ö zacar, M., Poyraz, A. S., Genuino, H.C. Kuo, C.-H., Meng, Y., Suib, S. L., "Influence of silver on the catalytic properties of the cryptomelane and Ag-hollandite types manganese oxides OMS-2 in the low-temperature CO oxidation," *Applied Catalysis A: General* **2013**, *462*, 64-74.
- Pahalagedara, L., Sharma, H., **Kuo, C-H.**, Dharmarathna, S., Joshi, A., Suib, S. L., Mhadeshwar, A. B., "Structure and Oxidation Activity Correlations for Carbon Blacks and Diesel Soot," *Energy & Fuels* **2012**, *26*, 6757-6764.

2. Book Chapters:

- **Kuo, C-H**, Suib, S. L., "Biosynthesis of size-controlled metal and metal oxide nanoparticles by microorganisms and applications," John Wiley & Sons, Inc., in press.
- Jin, L., **Kuo, C-H**, Suib, S. L., "The Role of Green Chemistry in Biomass Processing and Conversion- Heterogeneous Catalysts for Biomass Conversion" (eds H. Xie and N. Gathergood), John Wiley & Sons, Inc., Hoboken, NJ, USA. doi: 10.1002/9781118449400.ch11.

3. Patent Applications:

- **Kuo, C.-H.**, Pahalagedara, L., Suib, S. L. "Iron and cobalt doped manganese oxide with addition of clay binders as efficient adsorbents for gas phase hydrogen sulfide removal" issued in May, 2014.
- Poyraz, A. S., **Kuo, C.-H.**, Lei, J., Suib, S. L. "Mesoporous materials and processes for preparation thereof" issued in Feb, 2013 and filed in Jun, 2014.

4. Presentations & Meetings:

- **Kuo, C.-H.** and Steven L. Suib "Crystalline, Monomodal Pore Size Mesoporous Manganese Oxide for Water Oxidation Reaction" (**Oral Talk**) 247th ACS National Meeting & Exposition - March 16~20, **2014**, Dallas, TX "Chemistry & Materials for Energy".
- **Kuo, C.-H.** and Steven L. Suib "Heterogeneous Acidic TiO_2 Nanoparticles for Efficient Conversion of Biomass Derived Carbohydrates" (**Poster Presentation**) 247th ACS National Meeting & Exposition - March 16~20, **2014**, Dallas, TX "Chemistry & Materials for Energy".